

**T.R.
SAKARYA UNIVERSITY
GRADUATE SCHOOL OF NATURAL AND APPLIED SCIENCES**

**STRUCTURAL EVOLUTION OF THE CENTRAL GALAXIES IN
GALAXY CLUSTERS**

PhD THESIS

Eman Aly Shaaban ABDELMOTALEB

Physics Department

SEPTEMBER 2023

**T.R.
SAKARYA UNIVERSITY
GRADUATE SCHOOL OF NATURAL AND APPLIED SCIENCES**

**STRUCTURAL EVOLUTION OF THE CENTRAL GALAXIES IN
GALAXY CLUSTERS**

PhD THESIS

Eman Aly Shaaban ABDELMOTALEB

Physics Department

Thesis Advisor: Prof. Dr. Mehmet BEKTAŐOĐLU

Thesis Co-Advisor: Assist. Prof. Dr. Sinan ALIŐ

SEPTEMBER 2023

The thesis work titled “STRUCTURAL EVOLUTION OF THE CENTRAL GALAXIES IN GALAXY CLUSTERS” prepared by Eman Aly Shaaban ABDELMOTALEB was accepted by the following jury on 04/09/2023 by unanimously/majority of votes as a PhD THESIS in Sakarya University Graduate School of Natural and Applied Sciences, Physics department, Physics programme.

Thesis Jury

Head of Jury : **Prof. Dr. Mehmet BEKTAŐOĐLU** (Advisor)
Sakarya University

Jury Member : **Assoc. Prof. Dr. Ali Serdar ARIKAN**
Sakarya University

Jury Member : **Assoc. Prof. Dr. Murat HÜDAVERDİ**
Yıldız Technical University

Jury Member : **Assoc. Prof. Dr. Halil Arslan**
Sakarya ugulamalı Bilimleri Univeristy

Jury Member : **Assoc. Prof. Hüseyin Yasin UZUNOK**
Sakarya Univeristy

STATEMENT OF COMPLIANCE WITH THE ETHICAL PRINCIPLES AND RULES

I declare that the thesis work titled " STRUCTURAL EVOLUTION OF THE CENTRAL GALAXIES IN GALAXY CLUSTERS", which I have prepared in accordance with Sakarya University Graduate School of Natural and Applied Sciences regulations and Higher Education Institutions Scientific Research and Publication Ethics Directive, belongs to me, is an original work, I have acted in accordance with the regulations and directives mentioned above at all stages of my study, I did not get the innovations and results contained in the thesis from anywhere else, I duly cited the references for the works I used in my thesis, I did not submit this thesis to another scientific committee for academic purposes and to obtain a title, in accordance with the articles 9/2 and 22/2 of the Sakarya University Graduate Education and Training Regulation published in the Official Gazette dated 20.04.2016, a report was received in accordance with the criteria determined by the graduate school using the plagiarism software program to which Sakarya University is a subscriber, I have received an ethics committee approval document, I accept all kinds of legal responsibility that may arise in case of a situation contrary to this statement.

(04/09/2023)

(signature)

Eman ABDELMOTALEB

To my Family and the soul of my father

ACKNOWLEDGMENTS

All greatest gratefulness and deepest appreciation to Allah, the Almighty, for all gifts given for me and for his help and reconciliation.

I would like to express my special thanks of gratitude to my supervisor Prof. Dr. Mehmet BEKTAŞOĞLU who gave me the excellent opportunity to do this wonderful study, which also helped me in doing a lot of research and I came to know about so many new things.

I would like to convey my heartfelt gratitude to my co-supervisor Assist. Prof. Dr. Sinan ALİŞ for providing me with this wonderful opportunity to work on this project. The completion of the thesis would not have been possible without his help and insights.

I would also like to thank the referees and the jury members to have taken the time to read my thesis despite their busy schedule. I would also like to thank my mother Faiza, my brothers Ahmed and Hesham, the soul of my father, and all my family for their encouragement and support.

I would like to express my special thanks to Dr. Rasha Samir for her immense knowledge and great effort in guidance for this work. I dedicate this work to the soul of Prof. Gamal Bakr, Prof. Adel Sharaf and Prof. Inal Adham who gave me motivation and enthusiasm throughout my scientific life.

I would like to express my deep appreciation to my friends for their valuable help Especially Asmaa Rafa, Doaa Asef, Asmaa El Manaser, Amira Tawfeek, Mona Molhem, Dina Wahba, Khadija and all members of the Astronomy Department, Faculty of Sciences, Istanbul University and members of Physics Department Sakarya University. I am thankful to them who offered me any help and advice.

This work was supported by the TUBITAK (The Scientific and Technical Research Council of Turkey) project 117F311 through the ARDEB-1001 Program. I acknowledge the grant provided by the Türkiye Scholarships which is a government-funded higher education scholarship program run by the Republic of Türkiye for international students.

Eman ABDELMOTALEB

TABLE OF CONTENTS

	<u>Page</u>
ACKNOWLEDGMENTS	ix
TABLE OF CONTENTS	xi
ABBREVIATIONS	xiii
LIST OF TABLES	xv
LIST OF FIGURES	xvii
SUMMARY	xxi
ÖZET	xxv
1. INTRODUCTION	1
1.1. Galaxies: Definition and Properties	2
1.2. Classification of Galaxies.....	4
1.2.1. Hubble classification.....	4
1.2.2. Elliptical galaxies	5
1.2.3. Spiral galaxies: normal and “barred”	8
1.2.4. Lenticulars (S0).....	9
1.2.5. Irregular galaxies.....	10
1.2.6. De Vaucouleurs System	11
1.3. Galaxies Formation and Evolution.....	13
1.3.1. Theories of galaxy formation	13
1.3.2. Galaxy evolution	14
1.3.3. Morphology and redshift.....	15
1.3.3.1. Morphological types.....	17
1.3.3.2. Comparison of morphology and colour	18
1.3.3.3. Gas deficiency	19
1.3.3.4. Tidal truncation	21
1.3.4. Effect of environment on the galaxy morphology	22
1.4. Structural Analysis of Galaxies	23
1.4.1. Surface photometry of galaxies.....	23
1.4.2. Visual morphology	25
1.4.3. Parametric methods.....	26
1.4.4. Non-parametric methods.....	30
1.5. Redshift effect on structure	34
2. BRIGHTEST CLUSTER GALAXIES	37
2.1. Identification	37
2.2. Properties.....	38
2.3. The Formation and Evolution of BCGs	40
2.3.1. Formation models of BCGs	40
2.3.2. Growth history of galaxies	45
3. DATA AND METHOD	49
3.1. CFHTLS	49
3.2. Imaging at CFHT in Wide Field	51
3.3. Overview of TERAPIX Pipeline.....	52

3.4. Seeing and Image Quality	55
3.5. Photometric Redshift	56
3.5.1. Accuracy of photometric redshifts	56
3.6. Sample Selection	57
3.7. BCG Sample	59
3.8. Brief Introduction to GALFIT: 2D Image Decomposition	60
3.8.1. Analytical light profile functions	61
3.8.1.1. Images in FITS format with pixel values in counts	62
3.8.1.2. Proper sky value for image.....	62
3.8.1.3. Correct sigma image.....	62
3.8.1.4. Ideal PSF image for convolution.....	63
3.8.1.5. Removed neighboring contamination	63
3.8.1.6. Appropriate convolution box	63
3.8.1.7. Simple model for the fitting start	63
3.8.2. GALFIT inputs and outputs	63
3.8.2.1. Fits image	64
3.8.2.2. Sigma image	64
3.8.2.3. PSF image	64
3.8.2.4. Configuration input file.....	65
3.8.2.5. Fitting profile.....	65
3.8.3. Goodness of fit	68
3.8.4. Determining the point spread function.....	69
4. RESULTS.....	73
4.1. BCG Sample.....	73
4.2. Structural Analysis of BCGs	74
4.2.1. Preparing images	75
4.2.2. Mask images.....	76
4.2.3. Obtaining the point-spread function model.....	77
4.2.4. Running GALFIT	78
4.3. The Surface Brightness Profile Fitting of a Sample of BCGs.....	81
4.3.1. Distribution of structural parameters.....	83
4.4. The Kormendy Relation	86
4.5. Size-Luminosity Relation.....	88
4.6. Evolution of Structural Parameters	91
5. CONCLUSIONS.....	95
REFERENCES	97
CURRICULUM VITAE	113

ABBREVIATIONS

a	: Semi major axis
ADU	: Analog-to-Digital Unit
AGN	: Active galactic nucleus
b	: Semi minor axis
BCG	: The Brightest Cluster Galaxies
CADC	: Canadian Astronomy Data Centre
CCD	: Charge- Coupled Device, an electronic light sensor
CFHTLS	: The Canada–France–Hawaii Telescope Legacy Survey
Dec	: Declination
FWHM	: Full width half maximum
GALFIT	: Galaxy fitting
HST	: Hubble space telescope
ICM	: Intracluster medium
LMC	: Large Magellanic Cloud
ΛCDM	: Lambda cold dark matter
m	: The apparent magnitude
M	: The absolute magnitude
MGC	: Millenium Galaxy Catalog
n	: Sersic index
PA	: Position angle
PSF	: Point Spread Function
χ^2	: Qui square
Re	: Effective radius

LIST OF TABLES

	<u>Page</u>
Table 1.1. The percentages of various galaxy types in rich and poor clusters in the "field" (Keel, 2012).....	17
Table 1.2. The average concentration (C), asymmetry (A) and clumpiness (S) parameters for nearby galaxies as measured in the optical r-band (Conselice, 2003).	33
Table 3.1. Sky coordinates of the CFHTLS deep (D1, D2, D3, and D4) and wide (W1, W2, W3, W4) areas.	51
Table 3.2. Overview of the CFHTLS Wide fields. Sky coverage is expressed along R.A. and Dec axes.	53
Table 3.3. Summary of the W1 mean survey parameters.	55
Table 3.4. The observed area in the surface covered by the MEGAPrime focal Plane on the sky.	55
Table 3.5. For different magnitude cuts in the r-band, photometric redshift accuracy and outlier fraction (Coupon et al., 2009).	57
Table 4.1. Statistical features of effective radius (Re) (in kpc) and Sérsic index of the BCGs for different richness and redshift bins (number of objects, mean, standard deviation (σ) and median).....	82
Table 4.2. parameters that best fit the relation between $\log(\text{Re}) - \log(n)$ for different redshift and richness bins where a is the slope, and b is the intercept.	85
Table 4.3. The best-fitting parameters for the relation between $\log(\text{Re}) - \langle \mu_e \rangle$ (i.e., the Kormendy relation) for various redshift and richness bins, where a is the slope and b is the intercept.	87
Table 4.4. The size-luminosity relation's best-fit parameters for various redshift and richness bins, where a is the slope and b is the intercept.	90
Table 4.5. The Kormendy relation coefficients gathered in our work are compared with those from earlier studies on various redshift scales. The relation's slope is represented by a, and its intercept by b.	93

LIST OF FIGURES

	<u>Page</u>
Figure 1.1. The main components of a galaxy. On the left is an elliptical galaxy with the core, envelope, and halo structures. The image on the right represents a spiral galaxy showing the spiral arms, bulge, and halo structures.	2
Figure 1.2. Tuning-fork style diagram of the Hubble sequence.....	5
Figure 1.3. Examples of elliptical types.....	6
Figure 1.4. Examples of two elliptical galaxies: NGC 4621 on the left and M87 on the right. Images are from WikiSky/SDSS and NASA/ESA/HST Hubble Space Telescope, respectively.	7
Figure 1.5. Example of a barred spiral galaxy (NGC 1300) on the top and a spiral galaxy (M100) on the bottom. Images are from ESA/VLT and NASA/ESA/HST, respectively.	9
Figure 1.6. Image of an S0 galaxy (IC 5267). The image was taken by the Spitzer Space Telescope.	10
Figure 1.7. The amorphous galaxy M 82 in Ursa Major.....	11
Figure 1.8. The de Vaucouleurs system.	12
Figure 1.9. Morphology-density obtained for ellipticals, blue ellipticals and red spirals relationship (Bamford et al., 2009). Early-type versus local galaxy density for some galaxies (top), the number of red spirals (red, thick, solid line) and blue early-types ((blue, dotted line) in luminosity-limited sample versus local galaxy density (bottom left) as fractions of whole sample taken by Bamford et al., (2009) and (bottom right) as fractions of all spirals and early-types, respectively.	19
Figure 1.10. Gas peeling effect in the C153 galaxy in the Abell 2125 cluster.	20
Figure 1.11. A surface brightness profile of an elliptical galaxy in a cluster (Lopes de Oliveira et al. 2006).....	27
Figure 1.12. Sérsic profiles for a fixed effective radius for different values of n (Peng et al., 2002).....	28
Figure 1.13. The Fundamental Plane (Jorgensen et al. 1995).	29
Figure 1.14. The concentration (C), asymmetry (A) and clumpiness (S) measured on a nearby galaxy. For A and S, the value 'I' represents the original galaxy image, while 'R' is this image rotated by 180 deg. For the clumpiness S, 'B' is the image after it has been smoothed (Conselice, 2014).....	32
Figure 1.15. The concentration and asymmetry indices with coloured points representing the clumpiness (S) for each galaxy (top left); system with $S < 0.1$ are red, $0.1 < S < 0.35$ are green, and $S > 0.35$ are blue. Similarly, for A-S diagram, $C > 4$, $C < 3$ and $3 < C < 4$ are given with red, green and blue points, respectively. For S – C diagram, red points are for $A < 0.1$, green ones are for $0.1 < A < 0.35$, and blue ones are for $A > 0.35$	35
Figure 3.1. CFHTLS Deep and Wide fields. Wide areas (W1, W2, W3, and W4) and deep areas (D1, D2, D3, and D4) are illustrated.	50

Figure 3.2. Positions and geometry of the CFHTLS Wide fields. The black thick contours show the total field of view composing the ugriz filter collection of the T0007 release. The blue squares show a typical MegaCam field of view and indicate the positions of thereference center field. The MegaCam images included in the release are in green. They reveal the tiling and mosaicing of each CFHTLS Wide area. The small rectangles indicate individual MegaCam CCDs. W1, W2, W3 and W4 do not cover the same field of view, so the four Wide regions are not shown with the same scale in this figure. These plots have been produced during the calibration step of W1, W2, W3 and W4.	52
Figure 3.3. Positions, identification and naming conventions of the stacks in the CFHTLS Wide survey.	54
Figure 3.4. CFHTLS W1 pointings' geometry. For this field, there are 9×8 MegaCam pointings. Region of the released image with T0007 release is represented by a solid black line. Astrometric calibrations have been applied in areas beyond the black line. Because sseveral MegaCam pointings overlap, the overall effective area that was covered with W1 is 63.75deg^2 . The reference field with central coordinates of $\text{RA} = 02^{\text{h}} 18^{\text{m}}$, $\text{Dec} = -07^{\circ}00'$ is displayed in the centre as a blue rectangle (Hudelot et al., 2012).	59
Figure 3.5. A diagram illustrating the use of GALFIT.	64
Figure 3.6. GALFIT input file example.	65
Figure 3.7. Simultaneous example of model that fit of galaxies (original data, GALFIT model and residual, respectively).	69
Figure 3.8. The image on the CCD of PSF effects on the body	70
Figure 4.1. An example of cluster center and the BCG (ID 7942, $z_{\text{phot}}=0.282$). Cluster center is marked with cyan cross, BCG is marked with cyan circle, and the dashed circle represents the 500 kpc projected radius around the cluster center.	75
Figure 4.2. This study applied a masking method. The TERAPIX polygon mask file (left of the image) containing stars is combined with the masks for objects (centre), the final mask file (right) formed for BCG ID 7942.	77
Figure 4.3. PSFex was used to create a point-spread function model for a single MegaCam pointing. Inset is the enlarged image of the PSF of a sub-field. Similar PSFs are generated for each of W1's 72 areas.	79
Figure 4.4. Example GALFIT output file for BCG 4634-r band; empty image (top left), original image (top right), the GALFIT model (bottom left) and the residual image (bottom right).	80
Figure 4.5. BCGs' r-band apparent magnitude normalised distributions (top) and photometric redshift (bottom). The whole sample for each histogram is divided into two subsamples for the lower richness ($\lambda \leq 30$) and higher richness ($\lambda > 30$) clusters.	82
Figure 4.6. Normalised distributions effective radius (top) and Sérsic index (bottom) over the all-redshift range but for various richness cuts.	84
Figure 4.7. Relation between $\log R_e - \log n$ for poor (top) and rich (bottom) clusters. Blue, red, and gray points together with their corresponding linear fits (2σ) display various redshift bins. Confidence intervals are also shown for each fit.	85
Figure 4.8. The Kormendy relation for poor (top) and rich (bottom) clusters, the meaning of points, lines, and shaded regions is the same as Figure 4.7. ..	88

Figure 4.9. The size-luminosity relation for poor (top) and rich (bottom) clusters. The meaning of points, lines, and shaded regions is the same as in Figure 4.7. 90

Figure 4.10. Evolution of the Sérsic index (top) and effective radius (bottom) for poor and rich clusters. BCGs in poor and rich clusters are shown, respectively, by blue and red dots. For both poor and rich clusters, the median values for each redshift bin are displayed individually..... 92

STRUCTURAL EVOLUTION OF THE CENTRAL GALAXIES IN GALAXY CLUSTERS

SUMMARY

In this study, we aim to characterize evolution of the structural parameters of the brightest cluster galaxies (BCGs) by means of surface brightness analysis. In a redshift range of $0.1 < z < 1.0$ we will be able to show how the size of BCGs evolve. Deviation of the surface brightness – profile from ordinary elliptical galaxies can shed light onto possible merging histories. Thus, our aim is to present the evolution of structural parameters of BCGs and their correlation with cluster environments as a function of cluster redshift.

The central galaxies of galaxy clusters are known as (BCGs). They are the brightest, with quite homogeneous luminosities, and the most massive galaxies in the universe. These galaxies are elliptical galaxies, with no prominent star formation, and are usually found very close to the center of the clusters of galaxies. Due to being in the center of the host cluster, which could be playing a significant role in the formation of the BCG, interactions with the other galaxies in the cluster, and even cannibalization occur frequently. BCGs have distinct surface brightness profiles than regular elliptical galaxies. The unusual properties of the BCGs make the study of formation and evolution of the BCGs interesting. Modern theories explained many methods of galaxy formation: Galaxies can grow by mergers, or the accretion of intergalactic gas, or in situ star formation in collapsing galaxies.

The challenge of our studying the development of galaxies is to compare between different galaxies at different redshifts. Surveys provide us a lot of information in this regard. For instance, with its Deep Field observations, the Hubble Space Telescope (HST) offers images of galaxies at redshift $z > 1$. Furthermore, numerous neighbouring galaxies are covered by the Sloan Digital Sky Survey (SDSS) and Millenium Galaxy Catalogue surveys. They offer data on spectroscopy and imaging. Moreover, the Canada–France–Hawaii Telescope Legacy Survey (CFHTLS) survey, used in this study, is a major imaging project aimed to explore high redshift universe and huge scale structure.

TERAPIX has calculated the photometric redshifts (z_p) of the CFHTLS using LePhare. The Le Phare programme applied to calculate photometric redshifts. LePhare is a SED fitting tool that uses χ^2 minimization to get the most successful comparison of template spectra. Five various template spectra (E, Sbc, Scd, Irr, and SB) are used in the CFHTLS fields' photometric redshift computation. Covering a redshift range up to $z \sim 1.2$, these five templates are expanded into 66 templates. Using spectroscopic redshifts (z_s) from a VIMOS VLT Deep Survey (VVDS), the templates have been calibrated.

Understanding the structural parameters of (BCGs) offers crucial hints for understanding how they formed and evolved. The surface brightness profile fitting

findings of 1685 brightest cluster galaxies (BCGs) obtained from the (CFHTLS) in the redshift range of $0.1 < z < 1.0$ are presented.

We used a single Sérsic profile to fit r-band images of BCGs. To examine the effect of the environment, based on the richness of the host cluster, our sample is separated into two categories. According to our findings, based on statistics, BCGs in rich clusters are larger than those in poor clusters. For the Kormendy, the $\log R_e - \log n$, and the size-luminosity relations, we present the best-fit linear regressions.

We plan to analyze the surface brightness distribution and examine how the structural parameters evolved of various BCGs in the optical images obtained from the CFHTLS survey. The main tool for analysis will be GALFIT which is a data analysis algorithm that fits a 2-D analytic functions to galaxies and point sources directly on digital images. GALFIT is essentially used to gain more information and hints about the origin of galaxies from the analysis of its hidden fine structures.

Studies of galaxies using a 2-D modeling has been applied as it can recover the true parameter values without any degeneration. GALFIT, the fitting algorithm, is capable of modeling celestial object profiles in two-dimensional (2D) formats from their raw images. The main functions used in GALFIT to fit a galaxy are; Sérsic, Exponential disk, Nuker, Modified Ferrer, and Edge-on disk. Basically, one model for a specific galaxy is used, otherwise, additional models to minimize the residuals for a complex galaxy with multi-components can be added. Fitting a model to a galaxy image at the simplest conceptual stage is about defining a merit function. χ^2 , which is the precision of GALFIT fits, whose value varies from 1 to 2.

In the current study, we explored the structural evolution of BCGs found in clusters observed in the CFHTLS's W1 field. The coordinates and geometry of the W1 field has 9×8 certain pointings. The overall effective survey area in W1 is 63.75 deg^2 due to overlaps between the pointings. The 80% completeness limit in r-band for extended sources is 24 mag, while the median seeing of r band images for the W1 field is $0.71''$. The W1 galaxy catalogue, which masks the regions surrounding brilliant stars, ghosts, spikes, and other places of lower cosmietic quality, allowed the detection of galaxy clusters and associated BCGs. As a result, there are 2 871 455 ($r \leq 24$) galaxies in our object catalogue.

Among the data outputs of CFHTLS are images, mask files, object and photometric redshift catalogues, and more. TERAPIX processes, produces, and distributes these products. Since the most recent data release in 2012, all data has been made accessible to the public and may be viewed through the Canadian Astronomy Data Centre (CADDC).

According to the host cluster richness, we separated the cluster sample into two sub-samples, such as poor ($\lambda \leq 30$) and rich ($\lambda > 30$), to investigate any possible environmental effects. The variety of effective radii suggests that the environmental influences on the development of the BCG can vary. Galactic merger and cannibalism could be more frequent in richer clusters since BCGs existing in the middle of the potential well of galaxy clusters. Additionally, in the literature, it has been demonstrated that the host cluster characteristics and the BCG structural parameters for a BCG sample at $z \sim 0$ are correlated. However, the Sérsic index distributions for the poor and rich clusters are almost equal, as predicted by the K-S test.

In order to investigate for any evolutionary effects, we divided our BCGs into three redshift bins (i.e., $0.1 < z \leq 0.4$, $0.4 < z \leq 0.7$ and, $0.7 < z \leq 1.0$). The offsets in the Kormendy relation at various redshift bins are mostly caused by cosmic dimming. The slopes of the various relations seem to be consistent with one another.

GALAKTİK KÜMEDEKİ MERKEZİ GALAKSİLERİN YAPISAL EVRİMİ

ÖZET

Bu çalışmada BCG'lerin yapısal parametrelerinin evriminin yüzey parlaklık analizi ile karakterize edilmesi amaçlanmaktadır. $0.1 < z < 1.0$ kırmızıya kayma aralığında BCGlerin boyutunun nasıl geliştiği gösterilecektir. Yüzey parlaklığı özelliklerinin normal eliptik gökadalardan farklılık göstermesi, daha önce meydana gelen birleşmelere ışık tutabilir. Bu nedenle bu çalışmadaki amaç, BCGlerin yapısal parametrelerinin evrimi ve bunların küme ortamlarıyla olan ilişkisini kırmızıya kaymanın bir fonksiyonu olarak sunmaktır.

Galaktik kümelerinin merkezi gökadalara, en parlak küme gökadalara (BCG) olarak bilinir. Bu galaksiler oldukça homojen parlaklıklara sahip evrendeki en parlak ve en kütleli galaksilerdir. Genellikle belirgin bir yıldız oluşumu olmayan bu eliptik gökadalara çoğunlukla bir gökada kümesinin merkezine yakın bulunurlar. Kendisinin oluşumunda önemli bir rol oynamış olabilecek ev sahibi kümenin merkezinde yer alması sebebiyle BCG, genellikle kümedeki diğer gökadalara birleşene veya onları yutana kadar etkileşime girer. BCGlerin yüzey parlaklık profilleri, sıradan eliptik galaksilerinkinden farklıdır. BCGlerin alışılmadık özellikleri, BCGlerin oluşumu ve evrimi çalışmalarını ilgi çekici kılmaktadır. Modern teoriler, farklı galaksi oluşum yolları ortaya koyar: galaksiler ya birleşmelerle, galaksiler arası gazın birikmesiyle ya da çöken galaksilerde yerinde yıldız oluşumuyla oluşabilir. Oluşum gerçekleşikten sonra, galaksiler zamanla gelişir.

Galaksinin evrimi çalışmasındaki zorluk, farklı kırmızıya kaymalardaki farklı galaksiler arasında karşılaştırma yapmaktır. Anketler bu konuda birçok bilgi verir. Örneğin Derin Alan gözlemleri ile Hubble Uzay Teleskobu (HST), $z > 1$ kırmızıya kaymadaki birçok galaksinin görüntülerini sağlar. Ayrıca, Sloan Dijital Gökyüzü Araştırması (SDSS) ve Milenyum Galaksi Kataloğu araştırmaları, birçok komşu galaksiyi içerir. Bu araştırmalar hem spektroskopik hem de görüntüleme verileri sunar. Bunlardan başka, bu çalışmada kullanılan Kanada-Fransa-Hawaii Telescope Legacy Survey (CFHTLS) araştırması, büyük ölçekli yapıyı ve yüksek kırmızıya kayma evreni keşfetmeyi amaçlayan büyük bir görüntüleme projesidir.

CFHTLS'nin fotometrik kırmızıya kaymaları (z_p), LePhare programı kullanılarak TERAPIX tarafından hesaplanmıştır. Fotometrik kırmızıya kaymaları hesaplamak için Le Phare, χ^2 minimizasyonu yoluyla karşılaştırılan şablon spektrumları ile en iyi eşleşmeyi bulan bir SED uydurma aracıdır. CFHTLS alanlarının fotometrik kırmızıya kayma hesaplamaları için beş farklı şablon spektrumu (E, Sbc, Scd, Irr ve SB) kullanıldı. Bu beş şablon, $z \sim 1.2$ 'ye kadar olan kırmızıya kayma aralıklarını kapsamaları için 66 şablona genişletilmiştir. Şablonların kalibrasyonu, bir VIMOS VLT Deep Survey (VVDS)'den elde edilen spektroskopik kırmızıya kaymalar (z_s) kullanılarak yapılmıştır.

En parlak küme gökadalalarının (BCG'ler) yapısal parametrelerinin incelemek, oluşumlarını ve evrimlerini anlamak için önemli ipuçları sağlar. Bu çalışmada $0.1 < z < 1.0$ kırmızıya kayma aralığında CFHTLS'den türetilen 1685 en parlak küme gökadası için yüzey parlaklık profili fit sonuçları sunulmaktadır. BCG'lerin r-bant görüntülerinin uydurulması için tek bir Sérsic formu kullanılmıştır. Örnek, ortamın etkisini araştırmak için ev sahibi kümesi zenginliğine göre iki gruba ayrılmıştır. Sonuçlarımız, zengin kümelerdeki BCG'lerin, fakir kümelerdeki muadillerinden daha büyük olduğunu göstermektedir. $\log R_e - \log n$ ve büyüklük-parlaklık ilişkileri için en iyi uyum doğrusal regresyonlar sunulmaktadır. Ek olarak, yapısal parametrelerin değişimi incelenmiş, ancak örneğimizdeki BCGlerin $z \sim 1$ 'den itibaren önemli bir boyut değişikliği göstermedikleri sonucuna varılmıştır.

CFHTLS araştırmasından elde edilen optik görüntülerde yüzey parlaklık dağılımını analiz etmeyi ve çeşitli BCG'lerin yapısal parametrelerinin gelişimini araştırmayı planlıyoruz. Ana analiz aracı, 2 boyutlu analitik fonksiyonları galaksilere ve nokta kaynaklarına doğrudan dijital görüntüye uyduran bir veri analizi algoritması olan GALFIT olacaktır. GALFIT, esas olarak, gizli ince yapıların analizinden galaksilerin kökeni hakkında daha fazla bilgi ve ipucu elde etmek için kullanılır. GALFIT, bir galaksinin yüzey parlaklık profilini bileşenlerine ayırma tekniğidir.

Herhangi bir bozulma olmadan gerçek parametre değerlerini kurtarabildiği için 2 boyutlu modelleme kullanan galaksi çalışmaları uygulanmıştır. Uydurma algoritması GALFIT, ham görüntülerden gök cisimlerinin profillerini iki boyutlu (2D) formatlarda modelleyebilmektedir. GALFIT'te bir galaksiyi uydurmak için kullanılan başlıca fonksiyonlar Sérsic, Exponential disk, Nuker, Modified Ferrer ve Edge-on disk'tir. Temel olarak, belirli bir galaksi için bir model kullanılır, aksi takdirde, çok bileşenli karmaşık bir galaksi için artıkları en aza indirmek için ek modeller eklenebilir. En basit kavramsal aşamada bir modeli bir galaksi görüntüsüne uydurmak, bir değer fonksiyonu tanımlamakla ilgilidir. GALFIT fitinin hassaslığını ifade eden χ^2 değeri 1 ile 2 arasında değişir. Daha az değerli bir fonksiyonun daha iyi bir uyum parametresine yol açtığı ve böylece uygun bir galaksi görüntüsünü modelleyebileceği sonucuna varılmıştır.

Bu tez çalışmasında, CFHTLS'nin W1 alanında tespit edilen kümelerdeki BCG'lerin yapısal evrimi araştırılmıştır. W1 alanının geometrisi ve koordinatları, 9×8 noktaya sahiptir. Noktalar arasında örtüşmeler olduğu için W1'in toplam etkin tarama alanı $63.75^{\circ}2'$ 'dir. Genişletilmiş kaynaklar için r-bandında %80 tamlık sınırının 24 mag olduğu W1 alanı için r-bandı görüntülerinin medyan görüşü $0.71''$ dir. Parlak yıldızları, izleri, gürültüyü ve düşük kalitedeki diğer bölgeleri maskeleyen W1 galaksi kataloğu galaksi kümeleri ve ilişkili BCGlerin tespit edilmesine olanak sağlar ve bu katalog $r \leq 24$ olan toplam 2,871,455 galaksi ihtiva eder.

CFHTLS'nin veri çıktıları arasında görüntüler, istenmeyen arka plan ışığının silindiği dosyalar, nesne ve fotometrik kırmızıya kayma kataloğu ve daha fazlası yer alır. 2012'de gerçekleşen en son veri yayınından bu yana, tüm veriler halka açıktır ve Kanada Astronomi Veri Merkezi (CADM) aracılığıyla erişilebilir.

Herhangi bir olası çevresel etkiyi araştırmak için küme örneğini, ev sahibi küme zenginliğine dayalı olarak fakir ($\lambda \leq 30$) ve zengin ($\lambda > 30$) şeklinde iki alt örneğe ayırdık. Etkin yarıçapların çeşitliliği, ortamın BCG evrimi üzerindeki etkisinin farklı olabileceğini gösterir. BCGler galaksi kümelerinin potansiyel kuyusunun merkezinde yer aldığından, galaktik birleşme ve yutma zengin kümelerde daha sıklıkla meydana gelebilir. Ayrıca, literatürdeki bazı çalışmalar $z \sim 0$ olan BCG grubu için ev sahibi

küme karakteristikleri ile BCGlerin yapısal parametreleri arasında korelasyon olduğunu göstermişlerdir. Bununla birlikte, fakir ve zengin kümeler için Sérsic fonksiyonu dağılımları K-S testinin önerdiği gibi neredeyse aynıdır.

BCGler ayrıca $0.1 < z \leq 0.4$, $0.4 < z \leq 0.7$ ve $0.7 < z \leq 1.0$ olarak üç kırmızıya kayma bölgesinde gruplandırılmıştır. Farklı kırmızıya kayma bölmeleri için Kormendy ilişkisindeki ofsetler, temel olarak kozmolojik karartma nedeniyledir. Farklı bağıntılardaki eğimler arasında uyum olduğu görülmektedir.

1. INTRODUCTION

A galaxy cluster is a structure that consists of hundreds to thousands of galaxies. These galaxies with typical masses ranging from 10^{14} – 10^{15} solar masses, bound together by gravity, so galaxy clusters can be considered as the largest and most massive gravitationally bound structures in the Universe. These structures are excellent probes to test cosmological models. Furthermore, they are useful to understand the history of the Universe. This is due to the fact that they constrain the limits of observed physical parameters, such as mass or brightness, through time, in numerical simulations (Kravtsov and Borgani, 2012).

Clusters are thought to be located at the intersection of cosmic filaments, they are believed to form by merging with other smaller clusters or groups of galaxies. They continue to accrete gas and galaxies that gravitationally declined towards the gravitational potential well's centre along cosmic filaments (De Propriis et al., 2020).

Galaxies consider to be the basic building blocks of the visible matter in the Universe. Studying galaxies helps us unravel the physics of the Universe. Galaxy structure can be considered as one of the most important quantities to study evolution of galaxies. Galaxies are classified physically in many classes depending on their visual morphology. Spiral galaxies, for example, contain significantly more stars than the elliptical ones (Conselice, 2014). Galaxies have a variety of shapes and forms greater than those of any other class of deep sky objects. An important characteristic of galaxies is their tendency to form pairs, groups, and clusters. Lately, Galaxy groups and clusters are formed by 54% of the local universe's galaxies (with $z < 0.1$). Around these groupings and clusters, 20% of the population occur in areas that are collapsing. The remaining 26 % can be classified as field galaxies (Blanton et al., 2003). In this chapter a brief introduction about galaxies, their fundamental properties, classification, formation, and evolution is given.

1.1. Galaxies: Definition and Properties

Galaxies are significant elements of the cosmic puzzle, the universe, together with their evolution over cosmic time. Therefore, studying them is crucial to comprehending the Universe. Galaxies differ in terms of their characteristics, yet they all share a number of characteristics that make them gravitationally bound structures. These include interstellar matter (gas in various forms, cosmic rays, and dust), stars (main sequence, giant and subgiant stars, and stellar remnants including white dwarfs, black holes and neutron stars), and dark matter (Luoma, 2018).

Galaxies are groups of approximately 10^5 - 10^{13} stars which are held together by gravity. They participate in the Universe's expansion. Galaxies are frequently separated from one another by distances between 100 and 1000 times their diameters. Galaxies are 10^8 excessive concentrations compared to the average stellar density of the nearby universe (Mackie, 2011; Tawfeek, 2019). Masses of galaxies may have a range between less than a million to several trillion solar masses (Lucentini, 2002). The galactic body is divided into four main components as presented in Figure. 1.1.

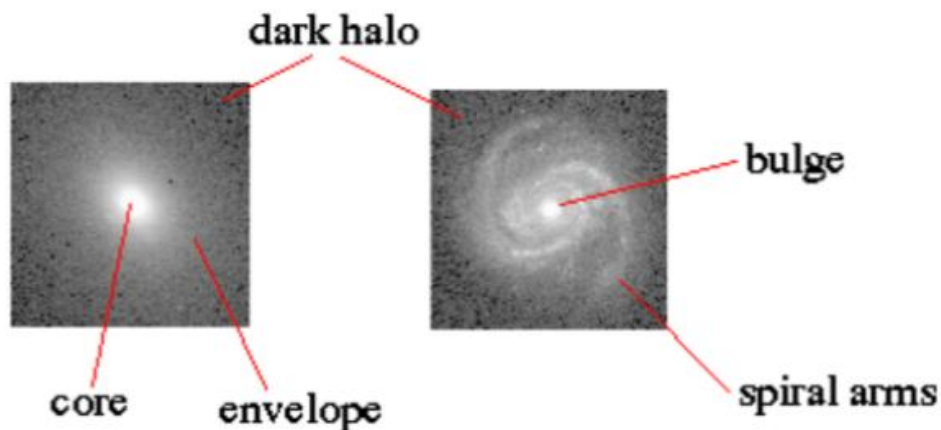


Figure 1.1. The main components of a galaxy. On the left is an elliptical galaxy with the core, envelope, and halo structures. The image on the right represents a spiral galaxy showing the spiral arms, bulge, and halo structures.

In 1929, Edwin Hubble claimed that almost all the galaxies are shifting away at speeds proportionate to its distance from the Earth, that more distant galaxies are travelling faster away from Earth. The galaxies' speed has been figured out by their redshift and expressed by Hubble Law.

According to different publications, gravitational interactions in the early universe's modest size influenced how galaxies developed. The number of stars in a single galaxy can range from a little thousand to billions, all of which are gravitationally tied to one another. Galaxies have been shown to be distant evidence of Big Bang theory, that took place 13.7 billion years ago. The earliest structures form soon after this first "burst" of the Universe's origin, brought on by significant volumes of cold dark matter. Initial hydrogen and helium clouds gradually split into small pieces called "protogalaxies" by both angular momentum and gravity (Hogan, 1998; Livio, 2000). These protogalaxies are finally converted into the first true galaxies by early star formation, together with gravitational coalescence (Steinicke and Jakiel, 2007).

To explain the primary characteristics of galaxies, a number of inner and external properties are required. The interior parameters indicate the astrophysical properties, and the exterior ones indicate geometrical properties of the galaxies. Among the astrophysical characteristics are linear dimension, luminosity (absolute magnitude), mass, rotation, content (stars, interstellar matter), metallicity (i.e., fraction of mass in elements heavier than helium), colour (a blue to red sequence of galaxies), dynamical characteristics (velocity dispersions for elliptical galaxies and circular velocity for spiral galaxies), surface brightness, and central massive black holes. The physical parameters provide significant information regarding how the galaxies are formed and evolved. Those parameters essentially describe the overall features. Therefore, they may be called "integral quantities". Numerous relationships exist between the physical variables. For instance, brighter galaxies, on average, typically rotate more quickly. This is an indication of their relatively big mass. Increase of the rotation speed of a spiral galaxy with its luminosity has been given by Tully and J. R. Fisher with the Tully–Fisher relation as $L \propto V^\alpha$, with $\alpha \sim 4$. Similarly, the Faber-Jackson relation, introduced by Sandra M. Faber and Robert Earl Jackson, stated that centre stellar velocity dispersion of elliptical galaxy (σ) and luminosity connected in the form $L \propto \sigma^\gamma$, where $\gamma \sim 4$. Due to the fact that they are not directly observable, such quantities are difficult to be measured. Determination of linear dimension or absolute magnitude, for example, requires knowledge of the distance. A galaxy's morphology is capable of yielding indications about its astrophysical characteristics. Therefore, different classification schemes have been advanced (Steinicke and Jakiel, 2007).

Among geometrical properties are space orientation (position angle, inclination, and elongation). Distance and coordinates are also included. Brightness of the apparent galaxy and angular diameter, based on a variety of criteria, including parameters within luminosity, linear diameter, radial velocity and redshift (z), could also be added to the list. All these parameters, except for the distance, are directly measurable (Steinicke and Jakiel, 2007).

1.2. Classification of Galaxies

Galaxies' classification is largely based on empirical studies that classify galaxies into categories depending on how they look (Van den Bergh, 1998). The shapes and structures of galaxies play a key role to understand the galaxy evolution which is based upon internal astrophysical properties (Steinicke and Jakiel, 2007). A satisfactory classification scheme needs to give standard terms used to characterise galaxies, along with hints as to how galaxies are created. As technology has developed, spectroscopy and photometric photometry have shown to be effective methods for quantitative analysis of the structural properties (Conselice, 2014). Galaxy classification can be done according to their morphologies using various schemes. The most famous one of such schemes is the Hubble sequence devised by Edwin Powell Hubble (1889 – 1953). Hubble provided the first meaningful scheme for classification of the galaxies in a 1936 book, "The Realm of the Nebulae". Some modifications and additions were made by Gerard de Vaucouleurs (1984) and Sidney van den Bergh (1998). That system still being used today (Conselice, 2014). The Hubble classification scheme refined by Sandage (1961) will be discussed in more details below.

1.2.1. Hubble classification

The classification system introduced by Hubble in 1926 revolutionized the basic understanding of galaxies. In this classification, galaxies may be split into various categories: elliptical (E), lenticular (S0), spiral or barred spiral (S, SB), and irregular (I). Hubble's first categorization in two dimensions was well recognised as the "tuning-fork" scheme, illustrated in Figure 1.2. The types on the left, called "early" by Hubble, start with an almost circular E0 and end with a very elliptical E7. Spiral galaxies, starting with Sa and SBa, and ending with Sc and SBc, were called "late" and given on the right of the diagram. This category has two subcategories; normal spirals (S)

and barred spirals (SB). Located where the two arms of the "handle" gather, lenticular galaxies are situated in between elliptical and spiral galaxies. Eventually, irregular galaxies are not of specific shape and do not fit into the three major categories. It is now understood that this system does not match an evolutionary progression (Conselice, 2014; Lake, 1992; Steinicke and Jakiel, 2007).

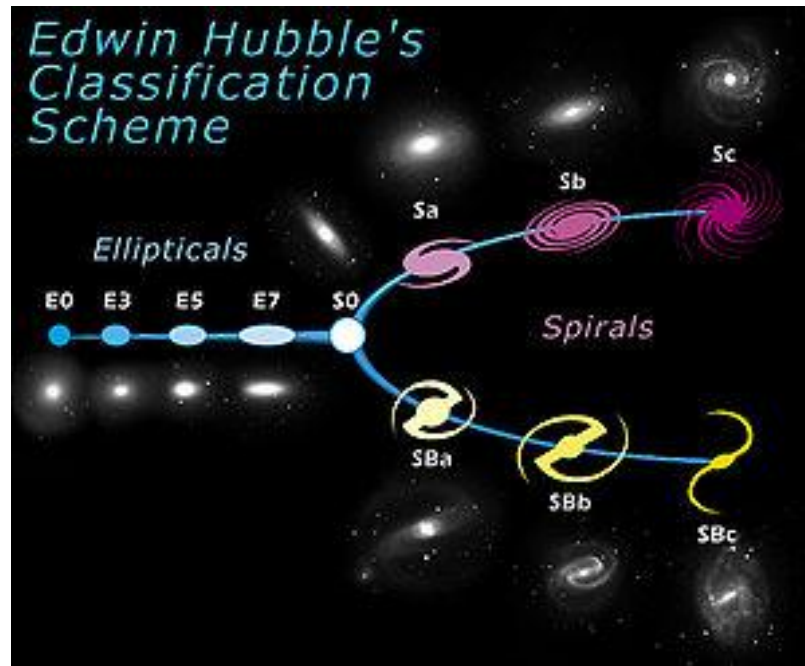


Figure 1.2. Tuning-fork style diagram of the Hubble sequence.

A few adjustments and expansions to the Hubble classification were made, and Sandage detailed them in two books. One of these works, the "Hubble Atlas of Galaxies", demonstrates the traditional Hubble scheme, with minor modifications. The second one is the two-volume Carnegie Atlas of Galaxies, which presents a more extended system and is demonstrated by a larger set of samples. De Vaucouleurs constructed a new version based on a system created for the "Second Reference Catalogue of Bright Galaxies" (RC2) (Steinicke and Jakiel, 2007). Many galaxy catalogues introduce a mix of different classification schemes.

1.2.2. Elliptical galaxies

The brightest galaxies, as well as some of the dimmest ones, in the Universe are ellipticals (Sparke and Gallagher, 2007). These galaxies generally have a symmetric shape. In images, they are represented as ellipses and have smooth and light distributions without features. From the middle to the edges, the surface brightness gradually declines. The actual figure might have oblate shapes like a thick biconvex

lens, or prolate shapes like a cigar or spindle or even triaxial without any symmetry. They constitute approximately 10% of the observed galaxies. Galaxies which is elliptical have elliptical isophotes shapes. Elliptical galaxies seem to contain very little dust or gas. Thus, no new star formation takes place. Therefore, These galaxies contain very old stars, including many red giants (Bertola, 1981; Sparke and Gallagher, 2007; Steinicke and Jakiel, 2007).

Elliptical galaxies are classified according to their ellipticities as E_n . Here $n = 10(1 - b/a)$, with a and b being the lengths of the major and minor axes. In the Hubble sequence, they are classified as $E_0, E_1, E_2, \dots, E_7$, where represents the flatness of the ellipse. E_0 , for instance, corresponds to round shape and no flattening and E_7 to a very elongated ellipse. Figure 1.3. illustrates some good examples of elliptical galaxies of different projected shapes. The Hubble classification scheme uses the apparent ellipticity. Thus, it refers to the projection of the galaxy's shape on the celestial sphere, instead of its actual shape (Sparke and Gallagher, 2007). Examples of two elliptical galaxies are shown in Figure. 1.4.

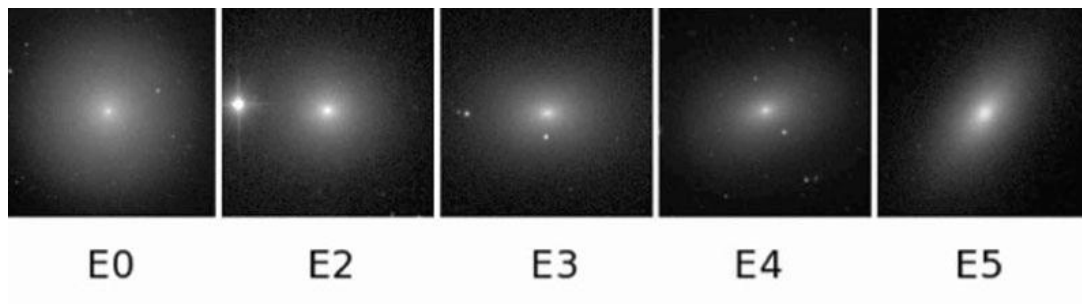


Figure 1.3. Examples of elliptical types.

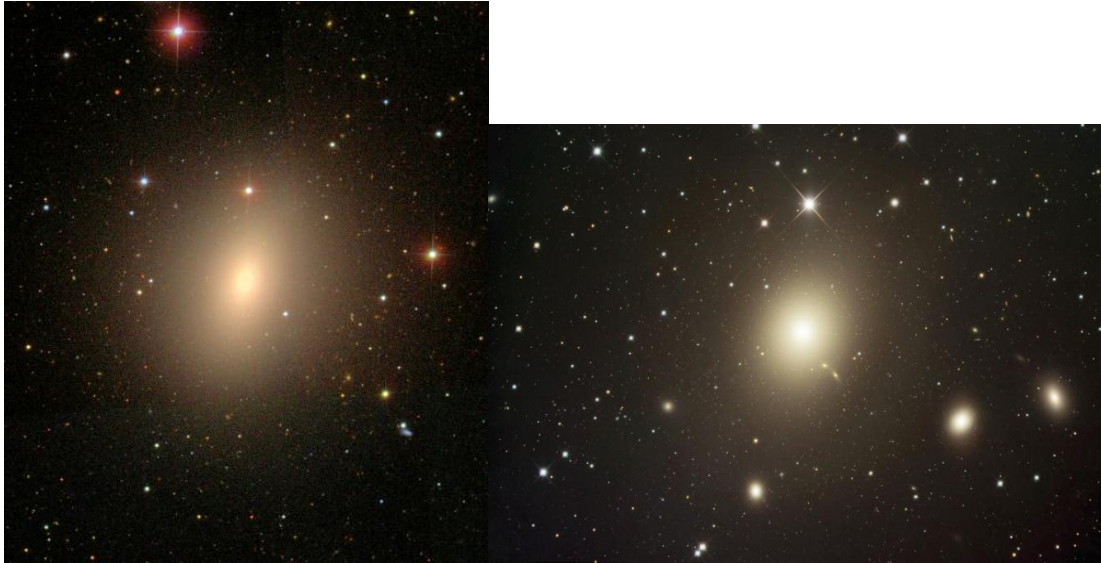


Figure 1.4. Examples of two elliptical galaxies: NGC 4621 on the left and M87 on the right. Images are from WikiSky/SDSS and NASA/ESA/HST Hubble Space Telescope, respectively.

Elliptical galaxies have a large range of masses from 10^7 to 10^{13} solar masses. The corresponding range of diameters of such galaxies is between 1/10 kpc and 100 kpc. Furthermore, their absolute blue magnitude varies over a correspondingly large range from -8 to -23. Thus, while the smallest elliptical galaxies, called dwarf ellipticals, may be only a little larger than globular clusters, the giant elliptical galaxies (eg., M87) are among the largest galaxies in the Universe (Zeilik, 2002). Giant ellipticals, together with their close cousins the cD galaxies, are the most massive and luminous class of galaxies (Sparke and Gallagher, 2007). These huge objects are generally located near the centres of galaxy groups and clusters. They can range from nearly nonrotating to fast rotating systems. The isophotes of their inner structures can range from spheroidal to “disky” or even boxy or rectangular.

Relatively rare and even highly massive are the cD (“core dominant”) galaxies (van den Bergh, 1998). These giant ellipticals have extensive diffuse halos that can encircle much of the central region of a large cluster. They are found almost solely in the centre of large galaxy clusters and are usually surrounded by some smaller systems. Giant ellipticals, also cD galaxies, merge with smaller objects by “galactic cannibalism”. Many cD galaxies can have more than one nuclear concentration in their cores. There are paired giant ellipticals called “dumbbell galaxies” in some of large galaxy clusters. These extremely massive systems are very close to each other and rotate around a

common centre of gravity. Such pairings can be observed in many dense galaxy clusters (Steinicke and Jakiel, 2007).

1.2.3. Spiral galaxies: normal and “barred”

Spiral galaxies represent about 70% of observed galaxies. They are rich in gas and dust. In disc galaxies, which is characterized by a disc- a flattened circular volume of stars- like spiral galaxies, most of the luminosity comes from a thin layer (Sparke and Gallagher, 2007).

The most special feature that characterizes spiral galaxies from the other types is the presence of the spiral arms structure. In general, a spiral galaxy has two spiral arms, but some others, such as our galaxy, the Milky Way, may have more than two arms (Zeilik, 2002). Spiral galaxies consist of a flat, rotating disk, and a central bulge, which contains old stars and is similar in appearance to an elliptical galaxy. The disk is the place where spiral arms originated. It contains an enormous number of stars and a large amount of gas and dust. Spiral arms are the sites of star formation and are usually brighter than the surrounding disk (Tawfeek, 2019). Glowing clouds of ionised hydrogen (HII regions) and hot young stars make the spiral arms look pink and blue in photographs (Steinicke and Jakiel, 2007). Some spiral galaxies, like the Milky Way, have a bar-like structure through their center (barred spiral galaxies, SB). About 30% of galaxies are barred spirals. They also often contain dust lanes in the bar and their spiral arms often start from where the bar ends (Dressler, 1980). Example of a spiral (a barred spiral) galaxy is shown on the left (on the right) panel of Figure 1.5.

Spiral galaxies, both S and SB, are divided into three subgroups, indicated with the lowercase letters a, b and c, based on the looseness of their spiral arms and largeness of their nucleus. For instance, Sa spirals have narrow, tightly wound arms and, despite some exceptions, a large bulge in the center. They are usually visible thanks to the presence of interstellar dust and bright stars. On the other hand, the nucleus of an Sc galaxy is very small, and its multiple spiral arms are more open (Sparke and Gallagher, 2007).



Figure 1.5. Example of a barred spiral galaxy (NGC 1300) on the top and a spiral galaxy (M100) on the bottom. Images are from ESA/VLT and NASA/ESA/HST, respectively.

1.2.4. Lenticulars (S0)

The word lenticular originated from the Latin language which means a biconvex lens. Lenticular galaxies are considered to be a transition class between ellipticals and early-type spirals (Sa, Sba). The S0 types (“lenticular”, or sometimes denoted “L”), are lens-shaped systems. They consist of a bright central bulge surrounded by an extended, disk-like structure, on the other hand, unlike spiral galaxies, the disks have no visible spiral structure. They are less flattened than the disks of spiral galaxies, displaying a high surface brightness as shown in Figure 1.6. In some cases, dust bands or even a weak bar structure (type SB0) are present. The central region of S0-galaxies is spherical, similar, although less massive compared to the bulges of spiral galaxies. In summary, lenticular galaxies have connections to both elliptical and spiral galaxies,

thus they are well placed by Hubble (Steinicke and Jakiel, 2007; Tawfeek, 2019). Example image of an S0 galaxy (IC 5267) is illustrated in Figure 1.6.



Figure 1.6. Image of an S0 galaxy (IC 5267). The image was taken by the Spitzer Space Telescope.

1.2.5. Irregular galaxies

Although the Hubble classification is the most used in the field, it does not include all types of galaxies. Some galaxies stand out as peculiar in shape and do not fit any of the three Hubble morphological categories. Most of these peculiar galaxies have evidence of unusual activities and some of them have been tidally distorted by interaction with other galaxies. Some are active galaxies with some evidence of violent internal processes taking place. Others may still be more normal galaxies, but give an unusual appearance (Tawfeek, 2019).

Approximately 3% of observed galaxies cannot be classified as ellipsoidal or spirals (Sparke and Gallagher, 2007). These galaxies, with no particular shape, have little symmetry in their structure. These galaxies, termed irregular galaxies, have divided them into two categories:

- Irr-I: asymmetric objects with no spiral arms, but with many O and B stars.
- Irr-II: asymmetric objects where the galaxy is smoother with frequent dust lanes. M 82, shown in Figure 1.7., could be given as an example.



Figure 1.7. The amorphous galaxy M 82 in Ursa Major.

Irregular galaxies have masses in the range 10^8 to 10^{10} solar masses, diameters from 1 to 10 kpc, and blue absolute magnitudes from -13 to -20. Other than that, they have few systematic features. Irregulars are gas rich galaxies with ongoing star formation and many of them appear to be an extension of late-type spirals (Grebel, 2004).

The most massive disk-like Irrs with residual spiral structure are called Magellanic spirals; e.g., the Large Magellanic Cloud (LMC) is a barred Magellanic spiral. Looser and more amorphous Irrs like the Small Magellanic Cloud (SMC) are sometimes also referred to as Magellanic irregulars or barred Magellanic irregulars if a bar is present (Grebel, 2004; Steinicke and Jakiel, 2007).

1.2.6. De Vaucouleurs System

The de Vaucouleurs system for classifying galaxies is a widely used extension to the Hubble sequence. de Vaucouleurs claimed that Hubble's two-dimensional classification of spiral galaxies is not adequate to describe the full range of observed galaxy morphologies. He argued that rings and lenses were important structural components of spiral galaxies. On the other hand, the de Vaucouleurs system retains Hubble's basic division of galaxies into ellipticals, lenticulars, spirals and irregulars. de Vaucouleurs introduced a more elaborate classification system for spiral galaxies, based on three morphological characteristics: bars, rings and spiral arms (see Figure 1.8):

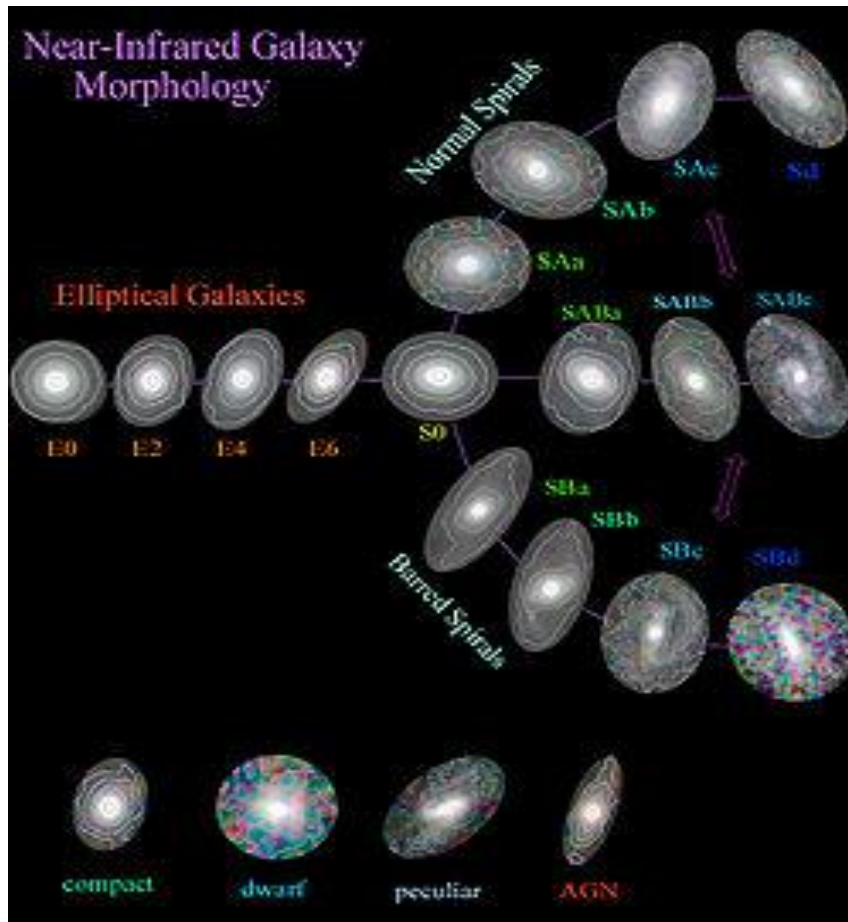


Figure 1.8. The de Vaucouleurs system.

The de Vaucouleurs classification offers symbols to denote abnormal structures but fails for really peculiar objects. It is now known that most peculiarities are due to interaction. “Warped disk”, found in spiral galaxies, can still be normal. The disk is not flat but twisted like the brim of a hat. The reason for that could most probably be due to a close encounter with a much smaller galaxy, resulting in a merger (Steinicke and Jakiel, 2007).

The de Vaucouleurs classification is multidimensional. It first appeared in the Second Reference Catalogue of Bright Galaxies (RC2). Then it was established in its successor, the Third Reference Catalogue of Bright Galaxies (RC3), (De Vaucouleurs et al., 1991). There exist various levels of specification (class, family, variety, stage). “Class” is comparable to the Hubble type. For spiral galaxies, the class is divided into three “families”: S, SAB, and SB. S (SB) denotes ordinary (barred) spirals as in the Hubble system, SAB is mixed (Steinicke and Jakiel, 2007).

“Variety” is another dimension. (s), (r), (rs) describe the way the spiral arms fit to the bulge. When they rise immediately from the bulge, which leads to as S-shaped spiral

pattern, one gets case (s). Case (r) is seen when they are tangential to the bulge. These form an inner ring structure. A mixed situation is described by (rs) (Steinicke and Jakiel, 2007).

1.3. Galaxies Formation and Evolution

Several theories have been proposed for formation and evolution of galaxies and they will be mentioned in the following section. In addition, a historic relation between the morphology and redshift will be introduced.

1.3.1. Theories of galaxy formation

Galaxy formation, one of the most active research areas in astrophysics, requires comprehensive knowledge on thermal history and universal gravitational force. Theoretical investigations have shown that galaxies are formed from a diluted but lumpy mixture primordial matter (hydrogen and helium) forged in the Big Bang. All galaxies began to form at about the same time approximately 13.7 billion years ago. There is a large volume of published studies (Hogan, 1998; Livio, 2000; Steinicke and Jakiel, 2007), describing two basic types of models, namely "top-down" and "bottom-up", for galaxy formation.

The "top-down" model states that the galaxies form from huge gas clouds larger than the resulting galaxy. When the internal gravity of the clouds collapse is strong enough to overcome the pressure inside the clouds. If the gas rotates slowly, then the collapsing gas can form most of its stars before the cloud can flatten into a disk and that may result in an elliptical galaxy. If the gas cloud rotates faster, then the collapsing gas can form a disk before most of the stars are made and a spiral galaxy forms. The rate of star formation may be the determining factor in what type of galaxy will form. However, the situation may be reversed, and the type of galaxy determines the rate of star formation. A recent modification of the "top-down" model states that there are extremely large gas clouds that fragment into smaller clouds, each of which then forms a galaxy. This explains why galaxies are grouped in clusters and even clusters of galaxy clusters ("superclusters"). The model predicts an exceptionally long time for the collapse of the super-large clouds and fragmentation into individual galaxy clouds (Conselice, 2014).

The “bottom-up” theory states that galaxies are formed from the merging of small, compacted masses with size of about a million solar masses. These clumps of masses will collapse together forming galaxies which are then drawn into clusters by their own gravity. According to this model, small galaxies should be more than large galaxies. In addition, clusters and superclusters of galaxies should still form. Both predictions have been observed to be true (Conselice, 2014).

1.3.2. Galaxy evolution

One of the most important ways of describing galaxy properties and studying their evolution is galaxy structure which has been studied since the first galaxies were observed. Investigating galaxies and their evolution through cosmic time plays a main role in understanding the Universe we live in. The first descriptions of galaxies were not resolved enough to study their structures, morphologies, and evolution, but the problem of galaxy evolution and formation is mysterious. Thanks to the new generations of technology and tools, galaxies are now studied up to redshifts of $z \sim 7-10$, although at the highest redshifts less information is available. The most common measures for the distant galaxies are colors, stellar masses, star-formation rates, sizes and basic structures. From these we know that the volume integrated star-formation rate increases with time from these ultrahigh redshifts until $z \sim 2$, when the star-formation rate begins to decline. Stellar mass measurements roughly agree with this picture, such that about half of all stellar mass is formed by $z \sim 1$. In the past, galaxies were much bluer than today. There is some debate and uncertainty concerning the star-formation history of individual galaxies and the relevant role of very old and very dusty galaxies at redshifts $z > 1$ (Conselice, 2014).

Modern theories explain galaxy formation in different ways: Galaxies can form either by merging or accretion of intergalactic gas or through in situ star formation in collapsed galaxy. After the formation has occurred galaxies evolve through time. This has been observed as the mass density of galaxies changes quickly at $1 < z < 3$ and $\sim 50\%$ of stellar mass is formed by $z = 1$. The galaxy structure is clearly different now than that at the highest observed redshift $z = 8$ (Luoma, 2018).

Hierarchical formation of clusters anticipate a strong connection between the cluster halo and its BCG. In this scenario, the stellar mass of the BCGs is closely related to the mass of the dark matter halo in which it is formed. De Lucia and Blaizot (2007)

showed that the stellar masses of BCGs are assembled around $z = 0.5$ with an evolutionary path consistent with the hierarchical growth of structures as suggested by the Λ CDM cosmology. Thus, investigating structural properties of BCGs play a significant role in the understanding of their formation, and especially their evolution.

It has been confirmed that there is a strong correlation between BCG parameters and the main properties of their host clusters (Alis, 2009; Ascaso et al., 2011; Lidman et al., 2012; Nelson et al., 2002). That connection with their host clusters (e.g., environment) have been extensively studied by means of stellar mass, size, surface brightness profiles, and the merging events (Bai et al., 2014; Bellstedt et al., 2016; Brough et al., 2005, 2008; Hansen et al., 2009; Stott et al., 2008).

Position angle, as a structural parameter of a galaxy, can be used to investigate the alignment of BCGs with their host clusters (Dubinski, 1998). Such studies in low (Fasano et al., 2010), intermediate (Chu et al., 2022; Niederste-Ostholt et al., 2010), and high redshifts (West et al., 2017) showed that BCGs are in general well aligned with their host clusters.

The challenge in the study of galaxy evolution is making comparisons among different galaxies at different redshifts. Different surveys have provided us a lot of information about galaxy evolution. For instance, the Hubble Space Telescope (HST) has provided images of thousands of galaxies at redshift $z > 1$ with its Deep Field observations. Furthermore, the Sloan Digital Sky Survey (SDSS) and the Millenium Galaxy Catalog (MGC) cover a vast number of nearby galaxies with both spectroscopic and imaging data (Luoma, 2018).

1.3.3. Morphology and redshift

Understanding the formation and evolution of galaxies, as a function of luminosity, environment, and star-formation and galaxy assembly over cosmic time, requires comprehensive knowledge on the morphology of galaxies. The advent of large digital sky surveys, with large depth and resolution, in addition to quantitative methods for morphology measurement, is providing a new era in this evolving field of astronomical research (Wadadekar, 2012).

Methods for galaxies' morphology classification, based on visual conception, were improved in the last century. For instance, de Vaucouleurs developed a version of the Hubble sequence, which included criteria such as bars, rings, and other internal

features. Then, scientists developed a system to classify galaxies based on the form of spiral arms and the apparent clumpiness of the light in these arms. Other astronomers such as Holmberg (1958) established that the morphology and physical properties of nearby galaxies correlate. He found that ellipticals are typically massive and red, and show little star formation, whereas spirals are less massive and bluer and have evidence for ongoing star formation. This quantitatively expands into other physical parameters as well (Conselice, 2014).

A new era in morphological and structural studies took place with the photometric photometry, especially charge-coupled devices (CCDs), thanks to what detailed measurements of light distributions in galaxies have been possible (Conselice, 2014). Modern studies are aiming to understand how galaxy morphology is influenced by environmental density, merger history, internal secular evolution, and star formation history. All these parameters have influence on galaxy morphology. In the last years, theories of galaxy evolution were gradually developed, thanks to advanced computer simulations that take into account all the physics of the gas, dust, stars, and dark matter (Wadadekar, 2012).

Redshift surveys are designed to find which galaxies are the oldest and which ones are the youngest. So, to understand the relation between redshift and the galaxy morphology, one must study redshift (z), displacement of the spectrum of an astronomical object toward longer (red) wavelengths. It is attributed to the Doppler effect, a change in wavelength that results when a given source of waves (e.g., light or radio waves) and an observer are in rapid motion with respect to each other. The emitted light is not actually red; instead, the term refers to the human perception of longer wavelengths at the red end of the visible spectrum. Examples of redshifting are a gamma ray perceived as an X-ray, or initially visible light perceived as radio waves. The opposite of a redshift is a blueshift, where wavelengths are shorter and energy increases. However, redshift is a more common term and sometimes blueshift is referred to as negative redshift. There are three main causes of red (and blue shifts) in astronomy and cosmology:

1. Objects move apart (or closer together) in space. This is an example of the Doppler effect.
2. Space itself expands, causing objects to become separated without changing their positions in space. This is known as cosmological redshift. All sufficiently

distant light sources (generally more than a few million light years away) show redshift corresponding to the rate of increase in their distance from Earth, known as Hubble's Law.

3. Gravitational redshift is a relativistic effect observed due to strong gravitational fields, which distort spacetime and exert a force on light and other particles. The Galaxy morphology is difficult at very high redshifts, specially Beyond $z \sim 1$, even with HST data, the parametric technique does not work well. In addition to the galaxies appearing faint and small, the dropout selection technique used to find these distant galaxies, is biased towards highly star forming ones, which are more likely to show disturbed morphologies. Non-parametric methods are common at high redshifts. However, with non-parametric methods, it is not easy to convert measured quantities to physically meaningful parameters such as bulge or disc luminosity (Wadadekar, 2012).

1.3.3.1. Morphological types

Morphological types show distinct variations in different environments. The percentages of various galaxy types in rich and poor clusters and in the "field" can be tabulated as follows in Table 1.1.

Table 1.1. The percentages of various galaxy types in rich and poor clusters in the "field" (Keel, 2012).

Type	cD	E+S0	S+I
Rich clusters	93	56	38
Poor clusters	6	20	14
Field"	< 6	< 24	48

Rich clusters are those clusters with hundreds to thousands of galaxies, mostly ellipticals and S0 spirals; ellipticals gather in the centre of the cluster, while spirals prefer to stay close to the periphery. However, poor clusters are those having only a handful of galaxies and tend to be a little bit more irregular in shape than rich ones.

E, S0 and cD galaxies prefer rich environments (see Table 1.1). Spirals and irregulars are known to prefer clusters of irregulars (rather than centrally concentrated) form, but this is likely to reflect a nearly universal relation between morphology and local galaxy

density (Dressler, 1980; Keel, 2012). Interestingly, this relation can be found within a single cluster, containing only E and/or S0 in the core. Considering the possibility that different clustering scales and densities grow at different rates complicates the heredity vs environment issue.

1.3.3.2. Comparison of morphology and colour

Morphology is defined by the dynamical state and star formation history of galaxies. Colour is an indicator of a recent (1 Gyr) star formation history of a galaxy, with no direct dependence on the spatial distribution of stars. Colour and morphology difference depending on the environment shed light on the work environmental mechanisms (Bamford et al., 2009). Automatic morphology proxies are used in many studies to address this issue. Researchers who considered the structural measures of morphology, have found that these quantities, such as concentration or Sersic index, are not as dependent upon environment as they are on galaxy mass (Hogg et al, 2004; Kauffmann et al, 2004). On the other hand, colour and star forming fractions have strong dependence on both environment and mass (Baldry et al., 2006). Thanks to the Galaxy Zoo data set, these issues may be determined using traditional visual morphologies, without recourse to automatic proxies (Bamford et al., 2009).

In order to investigate environment dependence of colour and morphology, one may adopt a measure of colour, in addition to a criterion for dividing objects into red and blue samples. The optimal, stellar-mass-dependent, divider was used to separate galaxies based on the bimodality of the u-r colour distribution (Baldry et al., 2006). Using the SDSS model magnitudes, the colour was effectively centrally weighted (Stoughton et al., 2002). Objects can be classified above and below the divider of Baldry and his coworkers as 'red' and 'blue', respectively (Bamford et al., 2009).

The morphology-density relations are described in Figure 1.9. A number of possibilities exist for the morphology-density relations, mostly concerned with getting rid of gas-rich spirals. The first one is that spiral galaxies cannot form in protoclusters. Secondly, spirals could turn into S0s this happens when they are stripped as a result of direct collisions or by ram pressure of the intracluster gas, including "galaxy harassment" in both cases (Moore et al., 1996). Thirdly, spirals may turn into elliptical galaxies via mergers. It could mean that S0s really are not closely related to spirals, or

it is more probably that the simple expectations are not realistic enough and that S0s, as van den Bergh has argued, are not a homogeneous class. (Keel, 2012).

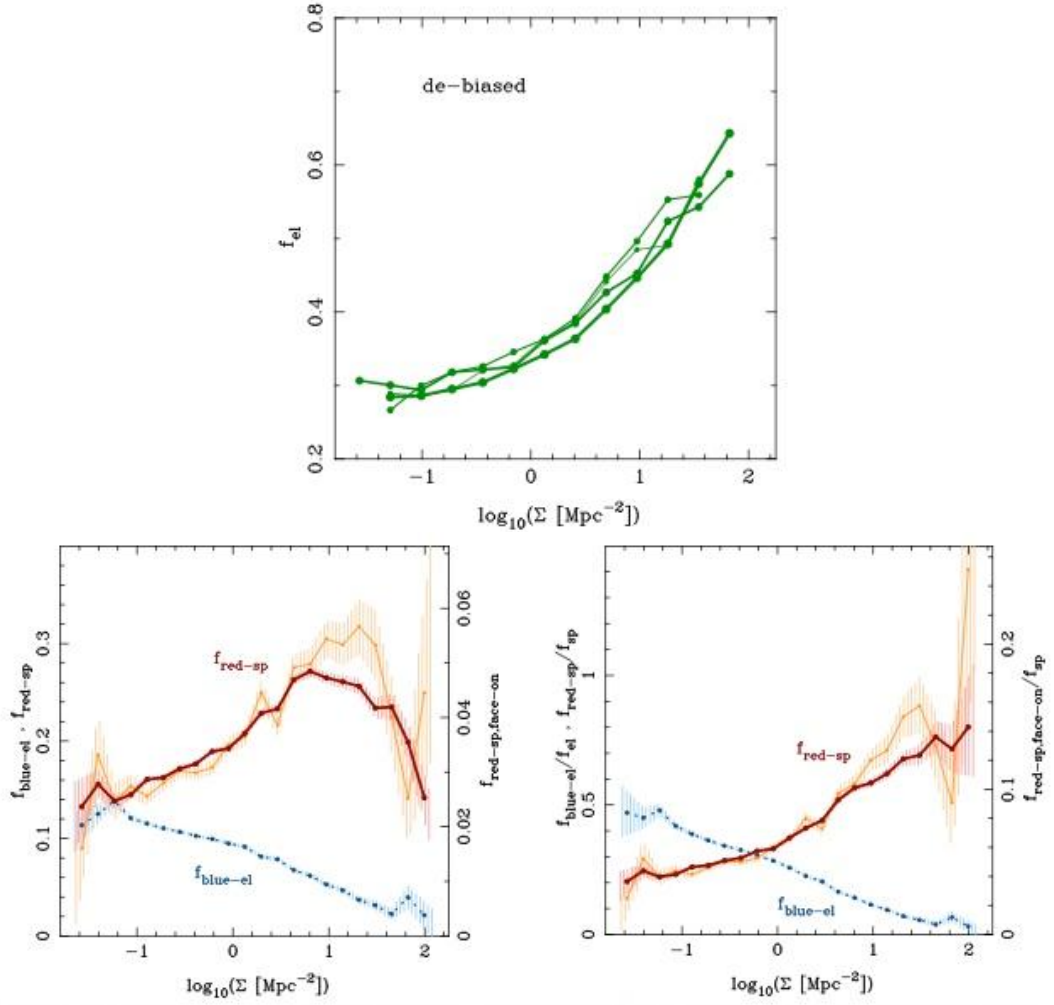


Figure 1.9. Morphology-density obtained for ellipticals, blue ellipticals and red spirals relationship (Bamford et al., 2009). Early-type versus local galaxy density for some galaxies (top), the number of red spirals (red, thick, solid line) and blue early-types ((blue, dotted line) in luminosity-limited sample versus local galaxy density (bottom left) as fractions of whole sample taken by Bamford et al., (2009) and (bottom right) as fractions of all spirals and early-types, respectively.

1.3.3.3. Gas deficiency

In cosmological contexts, the 21-cm line can be used as a probe of gas along the line of sight to a background radio source. The excitation state of the neutral H is characterized by an excitation temperature known as the 21-cm spin temperature (Keel, 2012).

Gas deficiency can be derived from HI measurements for spirals in clusters. Results given by Haynes et al., (1984) suggest removal of the gas for these galaxies coming close to the dense core. There is another suggestive correlation between the fraction of HI - deficient galaxies in a cluster and its hot gas content (Giovanelli and Haynes, 1985). Due to the strong correlation between overall cluster richness and the cluster X-ray luminosity, there is uncertainty as to whether this relationship gives enough information about the rate of stripping. These results do not reveal how the gas is removed (Keel, 2012). Evidence of ongoing ram-pressure effects come in the form of soft X-ray, in addition to optical emission-line trails, from galaxies travelling fast through dense clusters as shown in Figure 1.10.

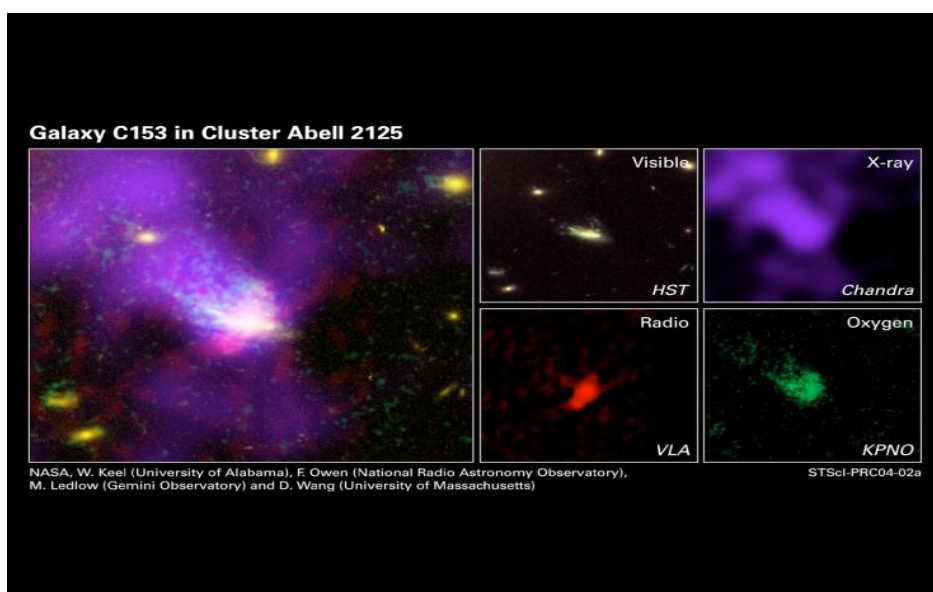


Figure 1.10. Gas peeling effect in the C153 galaxy in the Abell 2125 cluster.

The denser molecular clouds are obviously less fragile than HI clouds. It has been reported that CO deficiency level is less than that of HI (Stark et al., 1986). This is the result of tidal encounters as well as stripping. That is because the HI disks are often more extensive and consequently less strongly bound than CO disks. While Some galaxies appear to have impressive HI plumes, their optical images and CO distributions are not very disturbed (Keel, 2012).

Studies of the beginning of stripping gave results about star formation and the state of remaining gas. Cloud compression occurs, and a galaxy that is being stripped may see excessive star formation. That could be accounted for the Butcher-Oemler effect, which suggests clusters at redshift $z = 0.1 - 0.5$ contain more blue galaxies than nearby ones (Butcher and Oemler, 1978). Some investigators confirmed the prevalence of

blue galaxies in clusters at modest redshifts and that those galaxies are frequently in tight, interacting clumps. Hubble Space Telescope imaging shows that most of the anomalous blue galaxies are respectably normal spirals. Their clusters are quite rich in spirals and some mergers and tidal interactions are seen. Study of a cluster at $z = 0.83$ by van Dokkum et al. (2000) demonstrated that the fraction of spirals reached 39% and the merger remnants forming the ellipticals could be distinguished by colour.

While the Butcher-Oemler effect is almost universal at $z \sim 0.4$, it does not depend solely on the redshift. There exist a few very rich clusters of red galaxies at about $z = 0.4$, also rich clusters like Abell 2125 at $z = 0.25$ unusually rich in spiral members. Thus, the density history of a cluster is important. That is indicative of a clear selection effect (the Scott effect), which states that it is systematically to sample richer (and brighter in X-rays) clusters at high redshifts (Keel, 2012).

1.3.3.4. Tidal truncation

One of the most significant current discussions in the cluster environment is how it can lead to a gradual decline in the star-formation rate of its constituents. There is the disruption, which by the global cluster tidal field, of the gas that is accreted onto galaxy disks from a surrounding gaseous halo, and which fuels their star formation should be studied (Larson et al., 1980). That seems like a natural mechanism for suppressing star formation significantly over large regions of the cluster. Additionally, the deprivation of disk galaxies of their gas supply is highly germane to the formation of S0 galaxies (Bekki et al., 2001).

Tidal truncation cuts off the stellar distribution of galaxies in rich environments. This process is through two-galaxy encounters. It could also be through encounters with the cluster potential. This effect seems to be found in companions of bright galaxies. However, its role in clusters is unknown. If there is a stripping of dark halos, there is an indication of how dense halo material is, and the probability that cluster members could end up halo-deficient with much of the halo-matter associated with the entire cluster rather than with individual galaxies (Keel, 2012; Yelkenci, 2015).

It has been found that the rotation curves in the outer regions of cluster spirals are not flat as in field spirals. They are gently declined. this could be interpreted as smaller relative halo mass in cluster galaxies (Rubin et al., 1988). It could mean that halos never become as big as cluster members. It might also mean that interactions between

halos and halos or the overall cluster potential can strip some of the halo material. It has been found that this effect is strongly obvious for galaxies projected in the cluster cores. However, frequency of weak tidal encounters could be sufficient to prevent a cluster spiral from being in dynamical equilibrium (Keel, 2012).

However, all the previously mentioned evidence for spirals, contradictory to elliptical galaxies, does not show strong environmental effect. Their colours show a considerably consistent colour-absolute magnitude relation well accounted for just by metallicity changes, allowing very little recent star formation. It is common to look for the signs of recent star formation in just formed ellipticals in clusters. Relatively younger systems, right after discontinuation of star formation assumed to accompany gas removal, are the "E+A" systems, which spectroscopically resemble a mix of E galaxy and A-star spectra (Keel, 2012; Yelkenci, 2015).

1.3.4. Effect of environment on the galaxy morphology

It is important to understand how the morphology and the evolution of a galaxy is influenced by the factors such as environmental density, merger/interaction history, internal perturbations driven by instabilities, gas accretion from other galaxies, nuclear activity, internal secular evolution, and star formation history (Kormendy and Kennicutt, 2004). Better understanding of galaxy evolution is achieved by testing the predictions of galaxy evolution theories and observing crucial features such as galaxy morphology, multiple wavelength observations of large galaxy samples at various redshifts and different environmental conditions (clusters, groups, field) (Yelkenci, 2015).

Secular evolution provides a new collection of physical processes which are needed to be considered in order to understand galaxies. Hubble classification was in active and successful usage thirty years ago. However, an extensive list of commonly observed, regular features in disk galaxies, including lenses, boxy bulges, nuclear bars, and star clusters, is known. They were not understood and were not included in the classification schemes. Moreover, we knew about uniquely peculiar galaxies, which were also completely outside the classification process (Kormendy and Kennicutt, 2004).

Since the late twentieth century, galaxy morphology and evolution are thought to have been heavily influenced by the environment of the galaxy. Galaxies can interact and

merge, show gas build up and collide to trigger star formation. While each galaxy contains billions of stars, lots of dark matter, and various amounts of gas and dust, it's not easy to understand the details of galaxy interactions. Usually, supercomputers are used with advanced simulations that consider all the physics of gas, dust, and dark matter to understand how all this substance behaves during galaxy interactions (Wadadekar, 2012).

Galaxy environments can be extended over a wide range of density. The density is an aggregate of density both of galaxies themselves and of intergalactic material. With the extremes isolated galaxies and those in the cores of rich clusters can be found (knowing that dealing with galaxies are different, due to the differences in the processes operating in pairs and dense cluster environments).

Therefore, it is preferable to make tests for systematic differences between galaxies in different environments. These differences illustrate that certain types of galaxies do not form in regions that will become, say, rich clusters, or that they do not survive unaltered in such environments (Keel, 2012).

1.4. Structural Analysis of Galaxies

Recent developments in the theories of formation of the galaxies have heightened the need for image analysis which gives information about the properties of galaxies. In this section, we review quantitative methods of studying galaxy morphology and the nature of astrophysical insights that have been possible to be investigated using such image analysis. The major methods of morphological and structural study of galaxies will be explained. Among the major methods includes the well-established morphology visual method, Sersic fitting to measure galaxy sizes and shapes of surface brightness profile and non-parametric structural methods including concentration (C), asymmetry (A) and clumpiness (S) (CAS) method.

1.4.1. Surface photometry of galaxies

Surface photometry is one of the oldest techniques in modern astronomy to measure the surface brightness (SB) distribution of extended objects, so it is an important and powerful tool to study and derive the photometric properties of galaxies (Budding and Demircan, 2007; Tawfeek, 2019). The measure of SB of galaxies helps us to define the distribution of their light (luminous matter), their global structure, geometrical

characteristics, spatial orientation, stellar populations, characteristics of dust, etc (Jorgensen, 1999). Additionally, surface photometry and spectroscopic observations are the two major observational methods of extragalactic astronomy. Measuring across the galaxy gives us information about the internal structure and dynamics of a galaxy. The first attempt to measure the brightness distribution dates back to Reynolds in 1913 and Hubble in 1930 who studied the light distribution in elliptical galaxies. Surface photometry is currently done using charge-coupled devices (CCDs). The surface of a CCD is divided into individual picture elements, or pixels.

The analysis of objects in the astronomical images becomes very difficult due to the differences in shapes, dimensions and brightness of objects (Peng et al., 2010). Thus, the changes in the types, shapes and dimensions of galaxies are challenging problems in creating their surface brightness profiles. In addition, the image of the galaxies has different sensitivity to different bands, which results in an inaccurate surface brightness profile (Yelkenci, 2015). The surface brightness profiles (SBP) of stars on an astronomical image can be expressed easily by Gaussian shape. Since the beginning of photographic observations, many methods have been developed to investigate the surface brightness profiles of galaxies. The most important of these is the use of analytical functions that can model it. This technique is also known as the "parametric method" which described before, and it was first adapted to galaxies by de Vaucouleurs (1948). One of the common models to fit the radial SBPs is the empirical "de Vaucouleurs $R^{1/4}$ model". It shows that the surface brightness of an elliptic galaxy changes as a function of the distance R from the center of the galaxy. The de Vaucouleur formula expressed in (Equation 1.1).

$$I(R) = I_e \exp \left[-7.669 \left(\left(\frac{R}{R_e} \right)^{\frac{1}{4}} - 1 \right) \right] \quad (1.1)$$

where $I(R)$ is the SB in units of count rate/arcsec², R_e , the effective radius, which is the radius containing half of the total light and I_e represents the intensity at the effective radius R_e . If an isophote of brightness level I , has an area A then the equivalent radius, R , is defined as the radius of a circle which has the same area as A , i.e., as appeared in (Equation 1.2);

$$R = \left(\frac{A}{\pi} \right)^{\frac{1}{2}} = (ab)^{\frac{1}{2}} \quad (1.2)$$

where a and b are the semi-major and semi-minor axes of the isophote. The model parameters R_e and I_e of the de Vaucouleurs law are obtained by applying the nonlinear least square fitting technique (Conselice, 2014; Kormendy et al., 2009).

The Sersic index n , proposed by Sérsic (1963) and Sérsic (1968) and frequently used today, is the generalization of the de Vaucouleurs function. The Sersic index $n = 4$ indicates de Vaucouleurs profile; If $n = 1$, describes the exponential profile and $n = 0.5$ describes the Gaussian profile (Peng et al., 2002). Parametric modeling is based mostly on Sersic functions (Conselice, 2014), the use of the Sérsic profile to describe nearby galaxies is extensive.

Lately the fitting of galaxy two dimensional profiles with various forms such as the Sérsic, exponential and de Vaucouleurs profile is done using the GALFIT code by Peng et al. (2002), GIM2D by Simard et al. (2011), BUDDA by de Souza et al. (2004) and GASPHOT by Pignatelli et al. (2006). These codes allow a simple and fast method to measure the light profiles and radii of many galaxies, useful to obtain data to understand the evolution of galaxy structure. These codes, in addition to other similar ones, have limitations such as a constant ellipticity assumption within a given component. However, they are sufficient for gross measures of galaxy structure (Conselice, 2014; Yelkenci, 2015).

1.4.2. Visual morphology

The classic approach to understand galaxy structures is through their apparent visual morphology. The major classification system in use was developed by Hubble (1926), de Vaucouleurs (1959) and Sandage (1961, 1975). Galaxies are classified according to their visual morphology into spirals, ellipticals, and irregular/peculiar. The spirals can be further subdivided into spirals with or without a bar. Some studies are considered peculiar galaxies as mergers of two pre-existing galaxies, whereas irregular galaxies are lower mass galaxies containing a semi-random pattern of star formation as seen in Magellanic irregulars. These irregularities are typically too faint to be seen at high redshifts (Conselice, 2014).

On nearly all deep Hubble Space Telescope imaging has been conducted on visual morphological classifications starting from its earliest days (Dressler et al., 1994), continued with deeper HST observations, including those in the near-infrared optical rest-frame sample. However, there are some limitations on how to use these

classifications with higher redshifts, since it is not clear how a galaxy's apparent morphology will change the effects due to redshift rather than real evolution.

One of the problems with the galaxies that look 'elliptical' or 'disky' is that they don't have the same features as systems with the same nearby morphologies observed. Such features like sizes, light profiles, colors and star formation rates vary over time within the same morphological type of the galaxy (Conselice et al., 2011). Therefore, a morphological type is only a visual determination of the way a galaxy looks. It does not predispose to a particular local galaxy type or template or describe a certain history or scale of formation (Conselice, 2014).

1.4.3. Parametric methods

The parametric approach is very powerful to study the behavior of a sample of galaxies with respect to various correlations to explain different aspects of their formation mechanisms. Tracking the history of development image analysis revealed that image of the galaxy has been considered as a key factor in constructing a 1-d surface brightness profile, which can be defined as a plot of the surface light intensity or the brightness as a function of the distance from the center of the galaxy. There are various methods to perform the surface brightness profile, the simplest one taking a slice along the major axis (Vaghmare, 2015).

Regardless of the used method, it is important to use a simple mathematical function to get a profile whose behavior can be described. De Vaucouleur stated that in case of elliptical galaxies, the brightness varies as a function of $R^{1/4}$, with R being the distance from the center. Shown in Figure 1.11. is the surface brightness profile of a galaxy obeying that law. The x-axis describes $R^{1/4}$ and y-axis describes the magnitude so that the plot stands out the validity of $R^{1/4}$ profile (Vaghmare, 2015).

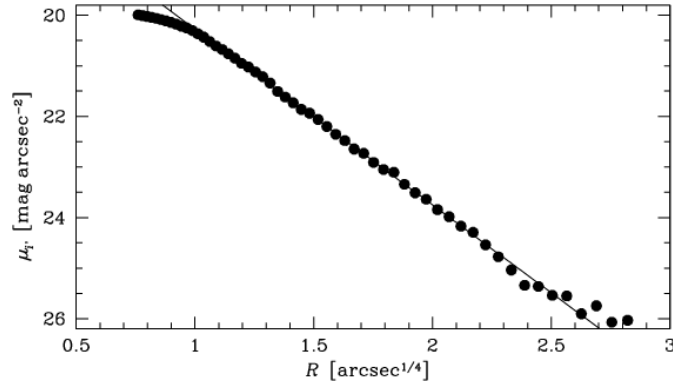


Figure 1.11. A surface brightness profile of an elliptical galaxy in a cluster (Lopes de Oliveira et al. 2006).

A major problem with De Vaucouleur’s law is that several elliptical galaxies did not obey and deviated from it systematically. It has been stated by Sérsic (1968) a general formula can be determined from De Vaucouleur’s law so that it could explain the brightness profiles for a wider sample of elliptical galaxies. The formula, named Sérsic law, is given as

$$I(R) = I_e \exp \left[-b_n \left(\left(\frac{R}{R_e} \right)^{\frac{1}{n}} - 1 \right) \right] \quad (1.3)$$

where n is referred to as the Sérsic index. As appeared in Equation (1.3) the quantity b_n is not an independent parameter defining the profile provided that R_e contains half the total light, b_n is a function of n and d can be estimated as $b_n = 1.9992 n - 0.3271$ (Capaccioli, 1989; Vaghmare, 2015; Yelkenci, 2015). Thus, the following parameters could be useful to determine the structure of an elliptical galaxy:

- R_e , a measure of the size.
- n , a measure of the concentration of light towards the center, as demonstrated in Figure 1.12. which represents the profile for a given effective radius for various values of n .
- I_e , a measure of the overall surface brightness of the galaxy. Generally, astronomers prefer to use the equivalent quantity μ_e , the surface brightness in mag per square arc seconds. I_e and the distance are independent quantities as long as they work in the nearby galaxies.

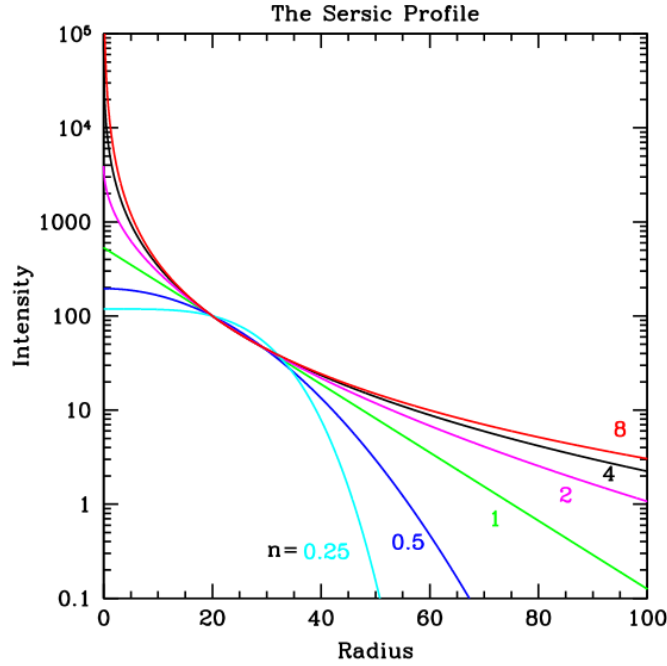


Figure 1.12. Sérsic profiles for a fixed effective radius for different values of n (Peng et al., 2002).

Noteworthy, parameters derived from the analysis of one galaxy do not reveal much about it. However, those collected from analysis of a statistically considerable sample of galaxies can powerfully shed some light on the physics inside these objects. Kormendy (1977), for instance, investigated a correlation between the surface brightness at effective radius and the effective radius of bright elliptical galaxies. It implies that large galaxies had lower surface densities and provided evidence about how galaxies formed. To avoid the higher level of errors and uncertainty of plotting the brightness at effective radius, it is preferable to use, in modern research, the average surface brightness within the effective radius (Vaghmare, 2015).

From the valid correlation given above (Equation 1.3), the physics behind the formation of elliptical galaxies can be explained. The Kormendy relation states that $R \sim I^{-0.8}$. It can be presented, assuming the virial theorem and a constant mass-to-light ratio, if elliptical galaxies form via dissipationless-dry-merging of two galaxies, then $R \sim I^{-1}$, on the other hand, if they form through rapid dissipative collapse of gas, $R \sim I^{-0.5}$.

Basically, The Kormendy relation is a two-dimension projection of a higher dimensional relation, known as the Fundamental Plane (Dressler et al., 1987). A three-

dimension relationship between the velocity dispersion of the stars at the galaxy center and the two parameters mentioned in the Kormendy relation exists and is written as:

$$\log R_e = A \log \sigma + B \mu_e + C \quad (1.4)$$

In Equation 1.4. where σ is the velocity dispersion, A and B are the slopes and C is the offset (intercept) of the fundamental plane. μ_e is the mean effective surface brightness. Jorgensen et al., (1995) investigated this relation and presented it in Figure 1.13.

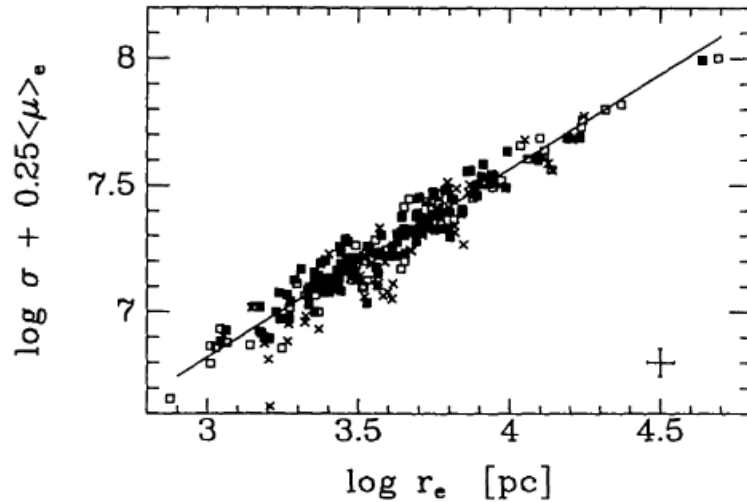


Figure 1.13. The Fundamental Plane (Jorgensen et al. 1995).

The Fundamental Plane makes a contribution to several purposes such as the following:

- Practically, the relation provides a method for estimation of the distance of objects. By measuring the average brightness and the velocity dispersion the effective radius can be determined. By knowing the effective radius in units of kilo parsec and angular units from observations, it is easy to estimate the angular distance to the object.
- Physically, the relation provides information on the physics underlying the formation of elliptical galaxies. By assuming the virial theorem, for instance, a smooth functional dependence of the mass-to-light ratio M/L on luminosity and that ellipticals form a homologous family, the fundamental plane can be derived as $M/L \sim L^{-0.25}$. Elliptical galaxies obey this correlation over a wide range of luminosities and other properties is a witness to common underlying formation processes (Vaghmare, 2015).

The photometric plane is another example of a correlation which includes photometric parameters namely n , R_e and $\mu(0)$ (the central surface brightness) (Khosroshahi et al., 2000). Study of Freeman (1970) demonstrated that the brightness profile of late-type galaxies on the Hubble tuning form exhibit little contribution from a bulge-like component. That can be described using an exponential profile (see Equation 1.5).

$$\log(n) = (0.231 \log R_e) + 0.291 \quad (1.5)$$

where R_d is the disk scale length and defining the distance from the center at which the intensity falls to $1/e$ times the intensity at the centre, $I(0)$. The most suitable profile that can describe the late-type galaxies is the total surface brightness profile, which is a combination of Sérsic and exponential profile. This combination allows one to decompose the brightness distribution into the bulge and disk contributions (Conselice, 2014; Kormendy et al. 2009; Vaghmare, 2015).

1.4.4. Non-parametric methods

The non-parametric method of measuring distributions of galaxy light is a more recent technique. These methods of measuring galaxy structure began in the photographic era by Morgan, in 1962, who attempted to quantify the light concentration in galaxies. Quantitative measures were not carried out until the mid-1990s (Conselice, 2014; Luoma, 2018). The development of methods and tools for measuring the light structures of galaxies began when the first deep images of distant galaxies were obtained by HST. Their use for low redshift measurements was also denoted at about the same time (Conselice 1997; Rix and Zaritsky, 1995). These works showed that quantitative galaxy structure correlates with other parameters, such as color and peculiar features suggesting mergers or interactions between galaxies (Conselice 1997, 2014; Rix and Zaritsky, 1995).

Currently, the most common non-parametric methods for calculating galaxy structure are CAS system and related parameters. CAS system include the concentration (C), asymmetry (A), and clumpiness (S) (Conselice, 2003). Those parameters are designed to capture the main features of the underlying galaxies' structures and, in contrast with the Sérsic fitting, they do not involve assumptions about the underlying form. Being measurable even out of high redshifts make the non-parametric parameters ideal for deriving galaxy evolution over several epochs (Conselice, 2014).

Vaghmare (2015) pointed out that free parameters of analytical functions were used to describe a component of the galaxy illustrating its structure. That assumes a given model can totally describe the target component. Such an assumption is not applicable in some cases. Like unrelaxed systems that lately experienced a merger. Those galaxies exhibit a disturbed morphology. Their light distribution could not completely be described using conventional analytical models. High redshift galaxies ($z \geq 1$) fall in other cases. These galaxies are still forming and do not achieve the structures as seen on the Hubble tuning fork. Additionally, this approach is not straightforward to automatically implement through pipelines like PyMorph (Vikram et al., 2010). To overcome these limitations, some studies have been done to develop alternative ways to describe the quantitative morphology of a galaxy with no or minimal assumptions made about the brightness distribution (Conselice, 2003; Lotz et al., 2004). In such alternative schemes, the quantities used to describe the galaxies are:

- Concentration: The concentration of light is used as a method to quantify the amount of light in the center of a galaxy compared to the amount in its outer part. It can be considered as a ratio of radii containing specific fractions of the total galaxy light. It is large for elliptical galaxies and classical bulges while it is low for late-type galaxies.

The definition most commonly used is the ratio of two circular radii which contain an inner and outer fraction given in Equation 1.6. 20% and 80% or 30% and 70% are the most common (r_{inner} , r_{outer}) of the total galaxy flux (see Figure 1.14).

$$C = 5 \left(\log \left(\frac{r_{outer}}{r_{inner}} \right) \right) \quad (1.6)$$

Values of C get higher when a larger amount of light is within the central region. A careful measurement of the concentration index is significant. It is due to the fact that different regions and radii used can produce very different values that systematically do not reproduce well when observed under degraded conditions (Conselice, 2014).

- Asymmetry: The asymmetry index (A), one of the most commonly used indices in non-parametric methods of measuring galaxy light distributions, is a measure of the asymmetry of a galaxy after its rotation along the galaxy's central line of sight by 180 deg (shown in Figure 1.14). This can be an indicator of what fraction of the light in a galaxy is in non-symmetric components.

Conselice et al. (2000) choose the center by an iterative process that finds the center resulting in a global minimum of A (see Equation 1.7). The asymmetry index is given as

$$A = \min \left(\frac{\Sigma(I_0 - I_{180})}{\Sigma I_0} \right) - \min \left(\frac{\Sigma(B_0 - B_{180})}{\Sigma I_0} \right) \quad (1.7)$$

where B_0 and B_{180} are the pixel values of a blank background area, I_0 is the original galaxy image and I_{180} is 180° rotated one (Conselice et al., 2000).

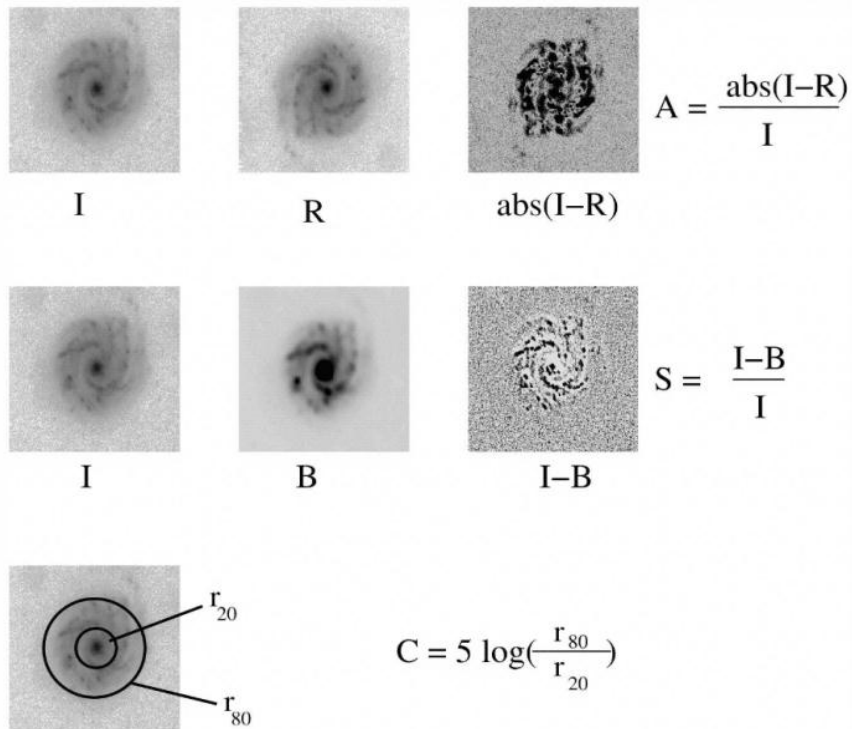


Figure 1.14. The concentration (C), asymmetry (A) and clumpiness (S) measured on a nearby galaxy. For A and S, the value 'I' represents the original galaxy image, while 'R' is this image rotated by 180 deg. For the clumpiness S, 'B' is the image after it has been smoothed (Conselice, 2014)

Typical asymmetry values for nearby galaxies and other CAS values are given in Conselice (2003) and presented here in Table 1.2. Quantitative structural values for the same galaxy can significantly be different between wavelengths. This is important for measuring these parameters at high redshifts.

Table 1.2. The average concentration (C), asymmetry (A) and clumpiness (S) parameters for nearby galaxies as measured in the optical r-band (Conselice, 2003).

Galaxy type	Concentration (R)	Asymmetry (R)	Clumpiness (R)
Ellipticals	4.4 ± 0.3	0.02 ± 0.02	0.00 ± 0.04
Early type disks (Sa-Sb)	3.9 ± 0.5	0.07 ± 0.04	0.08 ± 0.08
Early type disks (Sc-Sd)	3.1 ± 0.4	0.15 ± 0.06	0.29 ± 0.13
Irregulars	2.9 ± 0.3	0.17 ± 0.10	0.40 ± 0.20
Edge-on Disks	3.7 ± 0.6	0.17 ± 0.11	0.45 ± 0.20
ULIRGs	3.5 ± 0.7	0.32 ± 0.19	0.50 ± 0.40
Starbursts	2.7 ± 0.2	0.53 ± 0.22	0.71 ± 0.25
Dwarf Ellipticals	2.5 ± 0.3	0.02 ± 0.03	0.00 ± 0.06

- **Clumpiness.** The parameter clumpiness (or smoothness) (S) is used to define the fraction of light in a galaxy that is included in clumpy distributions. Clumpy galaxies have a fairly large amount of light at high spatial frequencies. Elliptical galaxies, as smooth structures, produce light at low spatial frequencies. Galaxies which undergo star formation appear to have very clumpy structures, and therefore have high (S) light/clumpiness values. Clumpiness can be calculated in various ways, the most widely used method (see Equation 1.8) was introduced by Conselice (2003), where the most common form is:

$$s = 10 \left[\sum_{x,y=1,1}^{N,N} \frac{I_{x,y} - I_{x,y}^{\sigma}}{I_{x,y}} - \sum_{x,y=1,1}^{N,N} \frac{B_{x,y} - B_{x,y}^{\sigma}}{B_{x,y}} \right] \quad (1.8)$$

Here, $I_{x,y}$ is the pixel value of the original image at (x, y), $B_{x,y}$ is the pixel value at (x, y) in a secondary image produced by blurring the original one, and N is the size of the galaxy in pixels, the smoothing kernel size σ is defined as a function of radius (Conselice, 2003).

The abovementioned three parameters can be combined to create a three-dimensional space in which different galaxy types can be classified. Figure 1.15 represents the concentration vs. asymmetry vs. clumpiness diagram. It demonstrates how these are

used to determine morphological types of galaxies in the nearby universe in CAS space. Furthermore, there are some other the quantities used to describe the galaxies such as:

- Gini Coefficient: It is a measure of how unequally the light is distributed in a galaxy. This is similar to the Gini coefficient used in economics to estimate the inequality of wealth distribution.
- The M20 coefficient describes whether the light is concentrated in the image or not. Compared to the parameter C, it does not imply the location of the concentration.

The multiplicity index (Ψ) is another parameter mentioned by Conselice. (Ψ) measures potential energy of the light distribution. The multimode of light profile (M), intensity (I) and deviation (D) are newer parameters used in the study of mergers by Freeman et al. (2013)

Using these coefficients, one can construct parametric spaces in which galaxies can be separated into various classes such as star bursts, ellipticals, etc. (Conselice, 2014; Vaghmare, 2015).

1.5. Redshift effect on structure

Some studies of structural measurement have dealt with nearby galaxies rather than all redshifts. Conselice (2014) pointed out different ways of measuring and quantifying the galaxy structure for comparisons across all redshifts. Many properties of nearby galaxies cannot be examined at high redshift.

One of the main problems with non-parametric structural indices is that they can change for more distant galaxies. This is due to both the evolution and distance effects, producing a smaller and fainter image of the same system, which should be taken into account when using the galaxy structure as an evolution indicator (Conselice, 2014).

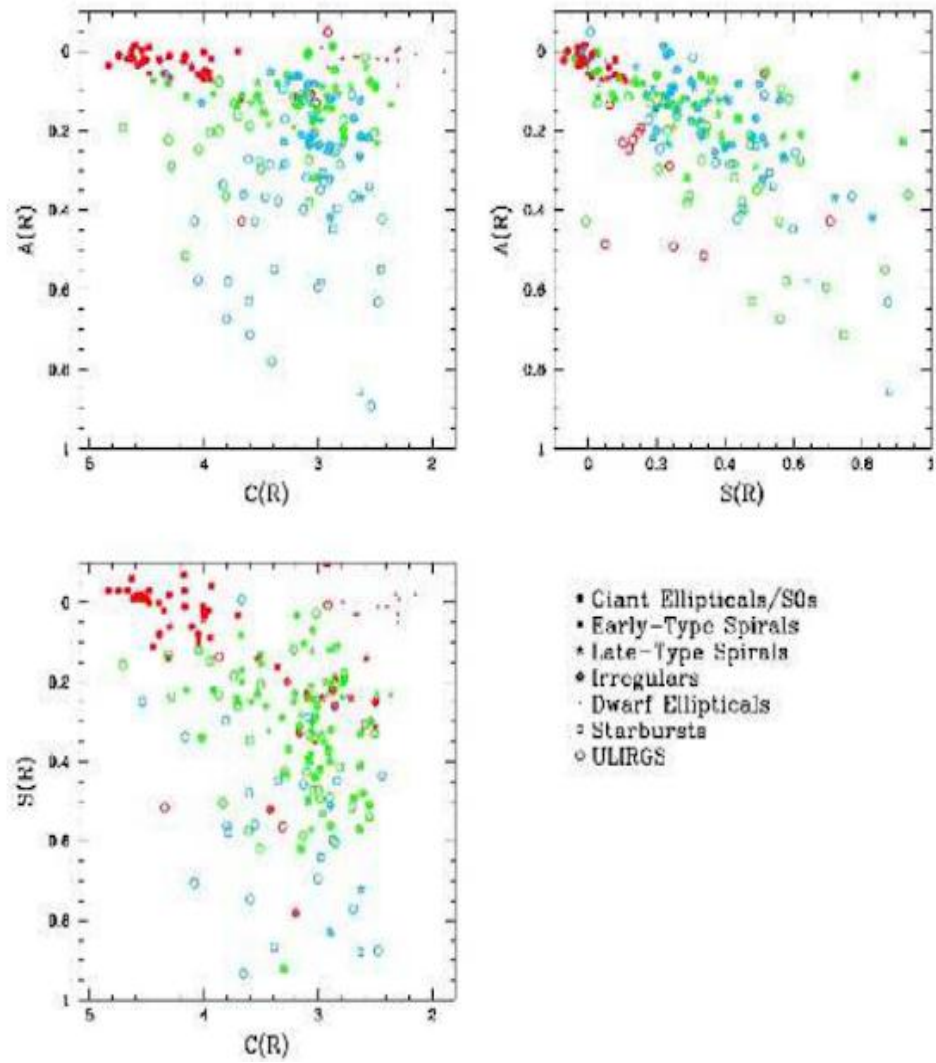


Figure 1.15. The concentration and asymmetry indices with coloured points representing the clumpiness (S) for each galaxy (top left); system with $S < 0.1$ are red, $0.1 < S < 0.35$ are green, and $S > 0.35$ are blue. Similarly, for A - S diagram, $C > 4$, $C < 3$ and $3 < C < 4$ are given with red, green and blue points, respectively. For S - C diagram, red points are for $A < 0.1$, green ones are for $0.1 < A < 0.35$, and blue ones are for $A > 0.35$.

2. BRIGHTEST CLUSTER GALAXIES

Galaxy clusters, the largest gravitational bound structure in the Universe, have recently gained great interest. Most of them host a ‘brightest cluster galaxy’ (BCG) at their core. The BCGs are among the largest, the most luminous and massive galaxies in the Universe. Due to being located at the centres of the rich galaxy clusters, they are easily recognized, both by observation and simulation. Also, they can be seen at a time when the Universe’s size is less than a third of its present size. They, therefore, can be evidence to test our ignorance of processes that drive galaxy evolution, even for the most massive galaxies in the Universe (Lidman et al., 2012). Comparing BCGs to regular elliptical galaxies reveals that they have peculiar characteristics in terms of their diameters, dark matter contents, and velocity dispersions (Von Der Linden et al., 2007). In this chapter the properties, formation, and evolution of BCGs will be outlined. The environmental effect and the quantitative methods for measuring galaxy structure are also explained.

2.1. Identification

BCGs can be classified as elliptical or early-type galaxies (Lauer & Postman, 1992), but a fraction of them possess an extended, low-surface-brightness envelope around the central region. These are referred to as cD galaxies (e.g. Dressler 1984; Oegerle and Hill 2001; Zhao *et al.*, 2015). We have to consider this galaxy class-elliptical and cD galaxies-when studying BCGs, because cDs are not found outside the BCG galaxy population. It can be considered morphology is one of the main observables focusing on the different properties of elliptical and cD BCGs (Zhao *et al.*, 2015). The term "cD galaxy" was introduced by Matthews *et al.* (1964). Their morphological features were clearly demonstrated for the first time by Morgan and Lesh (1965). Those galaxies are characterized by some distinctive features: (1) they exist exclusively in rich, regular clusters, and are the brightest or the second brightest object. (2) They fill the central position in the clusters. (3) They do not strongly flattened (Beers and Geller, 1983; Oemler, 1976; White, 1978). (4) They have a bright elliptical nucleus, this nucleus,

which can be double or multiple, is embedded in an amorphous shell (halo) (Hoessel and Schneider, 1985; Tonry, 1985). Bautz and Morgan (1970) accounted the distinct correlation between the existence of a central galaxy and its type with the type of cluster, in their classification of galaxy clusters, clusters containing a cD galaxy, designated as class I, are known to be the most regular, with a clear concentration toward the centre and have a clear numerical preponderance of earlier type galaxies.

2.2. Properties

BCGs are easily distinguishable and unique objects. They represent a distinct population, separated from the general elliptical non-BCG population. Visual distinctions are noticeable on local scales as several BCGs host special, extended star envelopes. Furthermore, they reveal remarkable homogeneity, and numerous studies demonstrate that BCGs are uniformly luminous in similarly massive clusters up to redshifts of $z \sim 1$. That contradicts the current simulations which struggle to reproduce the observed homogeneity seen in BCGs up to redshifts of $z \sim 1$. Numerous simulations were successful in reproducing the colours of observed BCGs, but they failed to model BCG growth accurately, anticipating the observed amount between factors of 2–4 (Furnell et al., 2018).

BCGs are characterized by their unique morphologies. Two BCG subtypes (elliptical and cDs) can be discriminated by morphology. cD is characterized by the presence of an extended, low-surface-brightness stellar envelope. However, elliptical is characterized by an approximately ellipsoidal shape and a smooth, nearly featureless image. In spatial extent and luminosity, cD galaxies are intermediate between normal galaxies and galaxy clusters. cD galaxies are considered the BCG of a cluster and form around 20% of the BCGs. Many fossil group galaxies are similar to cD BCG galaxies, from this observation one can conclude that the cD results from the creation of a fossil group which the new cluster accumulates around. Unlike fossil groups, cDs themselves are not found as field galaxies (Jordan et al., 2004).

Differences between the ellipticals and BCGs with different morphologies have recently been reported. It has been found that Fasano et al. (2010) both non-BCG cluster ellipticals and BCGs generally have triaxial shape, however, BCGs exhibit much higher tendency for prolateness thanks to the domination of cDs in the BCG population. Indeed, while the shape of elliptical BCGs does not differ from other

cluster ellipticals, cDs tend to have prolate shapes. Moreover, the authors of the above work suggest that the prolateness of the cDs could reflect the shape of the associated dark matter haloes. Zhao et al. (2015) demonstrated that the morphological distinction between ellipticals and cDs is accompanied by quantitative structural differences. cD BCGs are usually much larger in sizes and their light profiles cannot be modelled accurately using single Sérsic functions. On the other hand, elliptical BCGs are smaller and single Sérsic profiles provide better modelling to their surface brightness distributions. Such differences in morphology and structure suggest that cD and elliptical BCGs followed different evolutionary paths (Zhao et al., 2015).

Unlike nearby clusters, identifying the BCG in more distant clusters is often nontrivial. BCGs have been known to reside close to the peak of cluster X-ray emissions for most of the dynamically relaxed galaxy clusters. This X-ray peak indicates an inflow of the intracluster medium (ICM), the hot, diffuse gas between clusters, into the cluster core, which is a sign of a deep potential well. On the other hand, for clusters that have gone recent mergers with neighbouring groups and being out of dynamic equilibrium, this technique is not effective, with multiple, similarly luminous candidate BCGs and X-ray peaks often being present. In high redshift systems, merger activity is more common. Most studies stated that hierarchical merging is the dominant mechanism behind the growth of galaxy clusters. In spite of that, there are many issues to consider when quantifying cluster parameters such as mass, velocity dispersions, richnesses, X-ray mass–temperature scaling, and weak gravitational lensing (Furnell et al., 2018).

BCGs have been estimated to mainly grow through ongoing star formation as a result of condensing cluster gas regulated by some feedback mechanisms. For many hydrodynamical simulations, active galactic nucleus (AGN) activity remains the favored dominant candidate feedback mechanism. Some studies shifted toward closer examination of external baryonic processes, such as ram-pressure stripping and shock heating (Furnell et al., 2018).

BCGs have a number of singular properties. The origin and evolution have a direct relation to the mass which assembles in galaxy clusters. BCG luminosities can be considered as a homogeneous property, as first studied by Humason et al. (1956). Later works verified their high luminosities and small scatter in absolute magnitude, and, as a result, suggested them as standard candles for measuring cosmological distances (Sandage, 1972). Actually, both luminosities and small scatter in absolute magnitude

were originally used to increase the range of Hubble's redshift–distance law (Ascaso et al., 2011).

2.3. The Formation and Evolution of BCGs

2.3.1. Formation models of BCGs

Brightest cluster galaxy evolution has a great interest as BCG is located near the center of clusters and dominated. Recent evidence suggests that the classical hierarchical merging based the BCG formation scenarios have been a popular alternative to growth through star formation since $z \sim 1$. Generally, those models have been based on two theories, galactic merging, where numerous similarly sized galaxies merge together violently to form the BCG in a short amount of time, and galactic cannibalism, which is a slower process where mass is accumulated over time from small galaxies sinking to the bottom of the cluster potential well (Lidman et al., 2012).

Low rates of BCG star formation indicate mass-growth through dry mergers (Lavoie et al., 2016; Lidman et al., 2012; Liu et al., 2009; Ruszkowski and Springel, 2009) because of the dissipationless processes, they have little scatter in their luminosity (Aragon-Salamanca et al., 1998; Linden et al., 2007; Postman and Lauer, 1995; Von Der Linden et al., 2007). Size, luminosity, stellar mass, and the magnitude difference increase when the BCG expands through merging with nearby satellite galaxies (Bernardi et al., 2007). On the other hand, Lidman et al. (2013) and Scarlata et al. (2007) proposed that when BCGs are formed in the redshift ranges at $z < 1$, massive mergers, particularly gas-rich ones, could take place.

Presently, a two-step scenario behind BCG formation is favored, with bulge formation first at early times ($z > 2$) followed by the feature of envelope at later times ($z < 1$). Popularity of this approach is being increased to explain the morphology of cD-type of BCGs (i.e. bulge + halo) at low redshift and the apparent 'puffing up' of elliptical types. Additionally, there is persuasive indirect evidence that merger events take place at some point in the formation history of BCGs, with many examples of BCGs hosting multiple nuclei at their centres (Furnell et al., 2018). This view was supported by Liu et al. (2008) who stated that luminosity of BCGs were larger than expected from the bulk of early type galaxies, as a signal of dissipationless mergers playing an important role in their formation.

BCGs can be identified as the dominant galaxies within a cluster at $z \sim 1$. Stott et al. (2010) supported a scenario that BCGs were roughly totally assembled at $z \sim 1$. Others suggested that BCGs are still growing at the present epoch (Edwards and Patton, 2012; Liu et al., 2009; McIntosh et al., 2008). Some investigators proposed BCGs at $z < 1$ still undergo major merger events and grow by a factor of ~ 2 from $z \sim 1$ to the present epoch (Burke and Collins, 2013; Lidman et al., 2012). Simulations show that most of the mass comes from a small (≤ 10) number of merging events (De Lucia and Blaizot, 2007). Observation of mass separation in clusters and the existence of multiple bound companions around BCGs presented that clusters and the BCG environment are dynamically evolving in such a way that makes stellar material available to BCGs easily (Burke and Collins, 2013; Lavoie et al., 2016; Lidman et al., 2013).

Two mechanisms for the formation and evolution of cDs were proposed by (Gallagher and Ostriker, 1972; Gunn and Gott, 1972). Gunn and Gott (1972) suggest the possible existence of a physical link between the inter-cluster (IC) gas and cD galaxies. Such that the cooling of IC gas, by thermal bremsstrahlung, would produce a flow of material in the central cluster region that might accrete onto the cD galaxy. Gallagher and Ostriker (1972) suggested an alternative mechanism, such that the cDs might have formed of stars stripped from other galaxies. It was supposed that the outer parts of the cD are in equilibrium with the cluster's gravitational potential. Consistently, Dressler's observations of the cDs in Abell 2029 showed rapid growth of galaxy velocity dispersion with radius, implying that the mass-to-light ratio of the cDs went up as the distance from the galaxy centre increased. Gallagher et al. (1980) demonstrated the envelopes of cDs are bluer than the mean galaxy, and that was consistent with the tidal debris scenario.

Another popular scenario was proposed by Ostriker and Tremaine (1975) and developed by Ostriker and Hausman (1977) to state that the cD galaxy would grow by cannibalism of its neighbors. White (1976) supported this scenario by the n-body simulations. It has been shown that the dynamical friction mechanism could drive galaxies to the center as the cluster was evolving, and thus favor merging phenomena. Carnevali et al. (1981) modelled the evolution of small groups clarifying that the "merging instability" leads to the formation of a large central object. Roos and Aarseth (1982) re-examined the merging scenario for the formation of cD galaxies. They concluded merging of small groups of galaxies, before the cluster formation, required

for early creation of cDs. The merging scenario was supported by several pieces of evidence. A correlation between the luminosities of cD envelopes and the total luminosities of their parent clusters has been found (Oemler, 1976). The lack of significant luminosity segregation in cD-type clusters indicated that cD galaxies had cannibalized neighbouring galaxies. The cD's major axis was suggested to be aligned with the distribution of surrounding galaxies (Carter and Metcalfe, 1980).

In 1978, when the simulations by White indicated that merging can produce giant elliptical galaxies instead of cD extended halos. Numerous investigators estimated the cooling time of the IC gas in the dense X-ray emitting clusters to be lower than a Hubble time and they noted that "slow-moving galaxies in the core of X-ray emitting clusters could accrete large quantities of cooling gas (Cowie and Binney, 1977; Fabian and Nulsen, 1977; Lea et al., 1973; Silk, 1976). cD galaxies were characterized by small velocities relative to the cluster mean (Quintana and Lawrie, 1982) and that added a new strength to the hypothesis of cD growth via accretion of the cooling IC gas. First observational evidence for the existence of cool gas in the cluster centres came in 1979 with the detection of soft X-ray components in the spectrum of the Perseus galaxy NGC 1275 (Mushotzky and Smith, 1979).

The observational properties of BCGs can be described by various theories and provide a frame about their formation. BCGs were suggested to be formed through the accumulation of tidal debris stripped from cluster of galaxies. Galaxy cannibalism can also produce massive, similar BCG-like galaxies in the central regions of galaxy clusters (Ostriker and Hausman, 1977). In addition, Fabian et al. (1982) stated that gas cooling flows in galaxy cluster centers are responsible for creating these systems.

Over the past few decades, the cold dark matter (CDM) scenario is considered the most convenient for explaining the structure formation in the Universe. Interestingly, this galaxy formation scenario could also demonstrate the formation of BCGs. Consequently, Dubinski (1998) reported that the natural merging process of dark matter halos in a hierarchical model could produce central galaxies with similar surface brightness and velocity dispersion. Hierarchical simulations of structure formation have lately shown that the stellar component of BCGs was formed at early epochs (50% at $z \sim 5$ and 80% at $z \sim 3$) in separated galaxies which then accreted material to form the BCG through by dry mergers (De Lucia and Blaizot, 2007). That could mean that most of the stars located in BCGs actually were not formed in situ. In contrast,

they were accreted from galaxy satellites over the galaxy's formation history. Those accreted stars built the extended BCG halos (Abadi et al., 2006; Murante et al., 2007). The period of mass growth of BCGs has recently been found to be shorter than that expected from numerical simulations (Ascaso et al., 2011; Collins et al., 2009).

The evolution of BCGs and its origin provided us a lot of information about the evolution of their host clusters and on how large-scale structures in the Universe formed and evolved. There are many scenarios to explain the formation and evolution of BCGs. One of them proposed BCGs were to be formed by the accumulation of tidal stripped debris from clusters of galaxies and star formation in the cluster core, where gas cooling flow is responsible for the formation of the BCGs (Fabian et al., 1982; Ostriker and Tremaine, 1975). Lately, numerical simulations and semi-analytic models have suggested inside-out formation scenario which includes two phases for BCG formation, the stellar component of BCGs was initially formed through the collapse of cooling gas or gas-rich mergers at high redshifts; thereafter, BCGs continued to grow basically by dissipationless processes such as dry mergers. This inside-out formation scenario has the advantage of being broadly consistent with observations, avoiding the need for cold gas to flow that would be necessary if BCGs formed at later times. It also overcomes the problem caused by the merger rate in clusters being too low due to the high velocity dispersion in dynamically relaxed clusters. On the other hand, it has been claimed that feed-back, rather than merging processes, is the main mechanism affecting the evolution of the BCGs to the present epoch, ending the star formation within these systems (Ascaso et al., 2011).

Recent theories have posted that BCGs passed through different evolutionary paths. For instance, Guo et al. (2009) studied how the structural parameters of central cluster galaxies correlate with their stellar masses and their host dark matter (DM) halo mass. They found that the most important characteristic was the stellar mass which played a role in the shape and size of these galaxies, however, the DM halo mass did not exert an important role. Van der Wel et al. (2008) have also reached similar conclusions. In contrast, other studies claimed that there was a significant correlation between the cluster mass and the properties of BCGs (Ascaso et al., 2011). Furthermore, the cluster richness was added to the halo/cluster mass as an environmental indicator (Tovmassian and Andernach, 2012). Thus, as the effects of the halo mass and the cluster richness become different, it is necessary to take them into account as separate environmental

parameters when studying the BCG evolution. Many researchers have studied the properties of BCGs relative to other early-type galaxies, especially how they form and evolve (for instance: Bernardi, 2009; Shankar et al., 2015).

Acaso et al. (2011) studied two BCG samples at different redshift ranges. They found an increase in the size of the BCGs from intermediate to local redshift, however, they did not detect any variation in the Sérsic shape parameter in the two samples. The observed tendencies were model independent, and the results were strongly recommended (Acaso et al., 2011). The findings of Stott et al. (2011) also reported no evolutionary dependence on BCG profile slope between $0.25 < z < 1$ from their Sérsic fits. Furthermore, significant correlations between some of the BCG parameters and the main properties of the host clusters can be obtained. More luminous, larger, and centrally located BCGs have been found to be located in more massive and dominant galaxy clusters. Such facts may indicate that the host galaxy cluster has played an important role in the formation of their BCGs (Acaso et al., 2011; Bernardi 2009). Bernardi (2009) did find that BCGs are more massive and extended than field or non-BCG satellite galaxies; however, Weinmann et al. (2009), using SDSS data, found little difference. Discrepancies between results therefore appear to lie in the method of selection, the method of defining the environment and whether to take a single or multiple-component approach when fitting (Furnell et al., 2018).

Numerous pieces of evidence have shown that BCGs are not extracted from the same luminosity distribution function as normal galaxies and that could be attributed to their differences in the way of formation (Lin et al., 2010; Loh and Strauss, 2006; Tremaine and Richstone, 1977). Some indications show that the environment plays an important role in the formation of BCGs due to their special location in the cluster. Some works found correlations between the BCGs' luminosity and the mass or the X-ray luminosity of the clusters (Brough et al., 2002; Lin and Mohr 2004; Nelson et al., 2002; Whiley et al., 2008). An alignment between the major axis of the BCGs and the distribution of galaxies around the clusters located in 15 Mpc scales was discovered (Lambas et al., 1988). From another viewpoint, some studies suggest considerable observational evidence that the stars of giant elliptical galaxies were formed at high redshift and have evolved passively to the present day (Aragón-Salamanca et al., 1993; Bower et al., 1992). However, this evolution is different from that of normal elliptical galaxies due to the fact that BCGs are more metallic and have larger α -enhancement than do normal

elliptical galaxies depending on the stellar population studies (Loubser et al., 2009). This passive evolution of the stellar population contradicts some studies showing an evolution of the size and mass of BCGs. For instance, Aragón-Salamanca et al. (1998) found that BCG galaxies have grown their masses in the last 8 Gyr. A growth of ~ 2 at $z \sim 0.5$ has been reported by Nelson et al. (2002). Bernardi (2009) showed that BCGs at $z \sim 0.25$ are 70% smaller in size than nearby ones.

Like normal elliptical galaxies, the surface brightness profiles of BCGs are generally well fitted by de Vaucouleur or Sérsic profiles even at large radii (Graham et al., 1996). In spite of that, some of them show an excess of light, usually called envelopes, over the $R^{1/4}$ profile at large radii. Those envelopes show low surface brightness and large spatial extension. Although the origin of such extended envelopes is still not completely clear. Patel et al. (2006) claimed that the BCGs' extended stellar halos were likely to be from the BCGs themselves and were not part of the so-called intracluster light (ICL), which was formed by non-bounded stars and observed in some nearby clusters. They were formed by stars bounded gravitationally to the BCG. Nevertheless, the origin of the extended can be related to the origin of the ICL (Ascaso et al., 2011). Size evolution of BCGs is quite controversial. There have been studies showing little or no evolution (Chu et al., 2022; Stott et al., 2008), and significant change in the galaxy size (Ascaso et al., 2011; Bernardi, 2009). This controversy when coupled with the assembly time of the BCGs becomes more important. Samples from both observations and simulations point out to an older stellar population which assembled relatively recent epochs (e.g., $z \sim 0.5$). Homogeneity of the BCG properties (Bernardi et al., 2007) makes them attractive for using as standard candles, which then can be used on the cosmological scales as they are the most luminous galaxies in the Universe.

2.3.2. Growth history of galaxies

One of the important tools to understand the structure and evolution of the Universe is studying the growth of galaxies. In addition to the great contribution of redshift, both star formation and mergers play an important role in the growth of galaxies, (Vulcani et al., 2016). One of the accepted scenarios for the formation of structures in our universe was that BCGs grow their stellar mass over time by merging with other galaxies and by converting material accreted from their surroundings into stars (Lidman et al., 2013). It has been explained from observing BCGs in different ranges

of redshifts that the stellar mass of the average BCG is expected to increase significantly with time through merging with other galaxies. For example, in the semi-analytic model described by De Lucia and Blaizot (2007), the stellar mass increased by a factor of four between redshift $z = 1.0$ and today. In contrary, it appears that the growth is slightly slower than the predictions of the De Lucia and Blaizot (2007) model. It was found that the stellar mass of BCGs increased only by a factor 1.8 over the redshift interval $z \sim 0.9$ to $z \sim 0.2$ (Lidman et al., 2013). The results of others (Collins et al., 2009; Stott et al., 2010) were different stating that the stellar mass of BCGs exhibited little or even no change over the same redshift interval. That was partially due to the way the positive correlation between the mass of the cluster and the stellar mass of the BCG tended to dilute the observed evolution. The distant clusters used in those samples were more massive than the likely progenitors of clusters in the low-redshift comparison samples (Lidman et al., 2013). The distant clusters therefore tended to have more massive BCGs (Lidman et al., 2013). Vulcani et al. (2016) found that at all redshifts, progenitors, in a variety of environments, ranged from being isolated to having 5–10 companions with a mass ratio of at least 1:10 within a projected radius of 500 kpc. Generally, this analysis confirmed the model predictions, showing how the growth history of massive galaxies is dominated by in situ star formation at $z \sim 2$, both star formation and mergers at $1 < z < 2$, and by mergers alone at $z < 1$.

Recently some models predicted that BCGs between $z = 1.0$ and $z = 0.2$ could increase their stellar mass by a factor of 1.9 and such increase is lower than that reported in earlier simulations (De Lucia and Blaizot, 2007). Lidman et al. (2013) have suggested models that predict galaxy growth through a combination of minor and major mergers shedding light on the size of BCGs that should increase dramatically as they grow in mass.

physical properties should be considered to explain the growth of massive galaxies (Vulcani et al., 2016). At high redshifts, star formation was suggested to play an important role in growth of massive galaxies because a large fraction of it at $z \sim 2$ had high star-formation rates. Moreover, the old stellar ages of the most massive early-type galaxies and the existence of apparently “red and dead” galaxies with small sizes at $z = 1.5 - 2.5$ suggested that at least some of the growth is due to other mechanisms, like mergers. Recently, Graham et al. (2015) and many authors have suggested that some

massive galaxies have evolved by accreting a large disc of gas that rapidly forms stars rather than growth only via mergers.

Below $z \sim 1$, most massive galaxies ($M \sim 10^{12} M_{\odot}$) are generally found in dense environments (Blanton and Moustakas, 2009), such as at the center of clusters, and are identified as the Brightest Cluster Galaxies (BCGs). Many studies have focused on characterizing the assembly of massive galaxies, both from a theoretical and observational point of view. In semi-analytic models, the accretion of satellite galaxies is mainly dry and minor (De Lucia and Blaizot, 2007), while others pointed to major mergers in the centre of clusters as the main reason of the mass growth (Brough et al., 2011; Rasmussen et al., 2010). The companions of two of the BCGs would merge with the BCG within 0.35 Gyr (Brough et al., 2011). Although it is clear that mergers do occur, it has not been clear yet what fraction of the stars in the merging galaxies ends up in the BCG and what fraction is distributed throughout the cluster. High-resolution simulations suggested that 50% to 80% of the mass of mergers was not locked into galaxies, but it was distributed throughout the cluster (Conroy et al., 2007). Recent studies of Lidman et al. (2012) and others depended on colour gradients to support simulations that claimed that at least half of the mass was lost into the intracluster medium of the clusters (Vulcani et al., 2016).

The environment at high redshift, in which massive galaxies are located, is less characterized, and the coincidence between massive galaxies and BCGs is weak. Owsnworth et al. (2014), using a variety of number density selections, claimed that more than half of the total stellar mass in massive galaxies ($M \sim 10^{11.24} M_{\odot}$) at $z = 0.3$ was created externally to the $z = 3$ progenitors. Connecting high and low-redshift BCG data via evolution of their host halo masses, Shankar et al. (2015) found an increase since $z \sim 1$ of a factor $\sim 2-3$ in their mean stellar mass and $\sim 2.5-4$ in their mean effective radius.

It is important to precisely connect today's most massive galaxies to their progenitors at earlier times in order to understand how individual galaxies have evolved and gathered their mass and what mechanisms have derived these changes (Vulcani et al., 2016). Linking galaxies and their progenitors is an important task, through cosmic time, which in turn requires assumptions for how galaxies evolve. Recently, a few approaches have been developed to link galaxies across cosmic time (Mundy et al., 2015). While these techniques are limited, it is widely recognized that these

approaches are far more excellent than selecting galaxies at fixed stellar mass for studies of galaxy evolution (Vulcani et al., 2016).

3. DATA AND METHOD

3.1. CFHTLS

The Canada–France–Hawaii Telescope Legacy Survey (CFHTLS) is a major imaging project aimed to explore large scale structures and the high redshift Universe. CFHTLS requires precise magnitudes and redshifts for millions of sources (Benjamin et al., 2007; Fu et al., 2008; McCracken et al., 2008; Parker et al., 2007; Tereno et al., 2009).

CFHTLS consists of three survey sub-fields; Deep, Wide and Very Wide. There are four Deep-fields in the Deep survey and they are valuable tools to reveal BCG candidates and many other objects. Those Deep fields are monitored and broadened continuously to scan the largest possible area (Alis 2009; Coupon et al., 2009; McCracken et al., 2008). CFHTLS areas are shown in Figure 3.1. Images derived from the CFHTLS and other digital sky survey programs are transferred to the Canadian Astronomy Data Centre (CADC) for archiving, then to a catalogue known as the TERAPIX, at the IAP (Institut d'Astrophysique de Paris) for processing. Full details of observations taken with the MegaCam wide-field mosaic camera (Boulade et al., 2000) at the CFHTLS between June 1st, 2003 and September 12th, 2005, data reductions, catalogue preparation and quality assessment steps can be found on the TERAPIX web pages (McCracken et al., 2008). TERAPIX data based on visible and near infrared giant panoramic cameras (like MegaCam at CFHT). The ugriz filter collection is used within the CFHTLS. Object catalogues have multiple tasks as building tools for image processing and pipeline for giant visible and near-infrared cameras, providing tools for the handling of visible and near infrared images of large CCDs, generating calibrated images and catalogues for wide-field Legacy Surveys, Public Surveys, Massive Programs or PI programs to operate pipelines and providing technological support and processing resources to users of MegaCam and WIRCam (Coupon et al., 2009).

(CFHTLS) is an imaging survey carried out between 2003–2009 in the four wide and the four deep fields. The wide survey covers a total area of 171 deg^2 with imaging in u* g' r' i' z' bands. Due to the overlaps between adjacent fields, the effective area of

the CFHTLS-Wide is 155 deg^2 . Except the u-band, CFHTLS filters are almost identical with those used in the SDSS, hence we refer these filters as u g r i z for the rest of the thesis. CFHTLS made use of MegaCam which is a mosaic CCD camera consisting of 36 thinned EEV detectors with each one has 2048×4612 pixels. This configuration has approximately $1 \text{ deg} \times 1 \text{ deg}$ field of view for each MegaCam pointing. Processed individual images consisting of $19\,354 \times 19\,354$ pixels with a pixel scale of $0.186''/\text{pixel}$.

CFHTLS offers researchers the opportunity to work on many subjects in deep and wide sky areas such as star formations in galaxies, morphologies of galaxies, environmental interactions of galaxies, galaxy clusters, large-scale structure of the Universe, material distribution in the Universe, type Ia supernovae, solar system objects (Yelkenci, 2015). The coordinates of the CFHTLS deep and wide areas are given in Table 3.1 (Hudelot et al., 2012; Yelkenci, 2015).

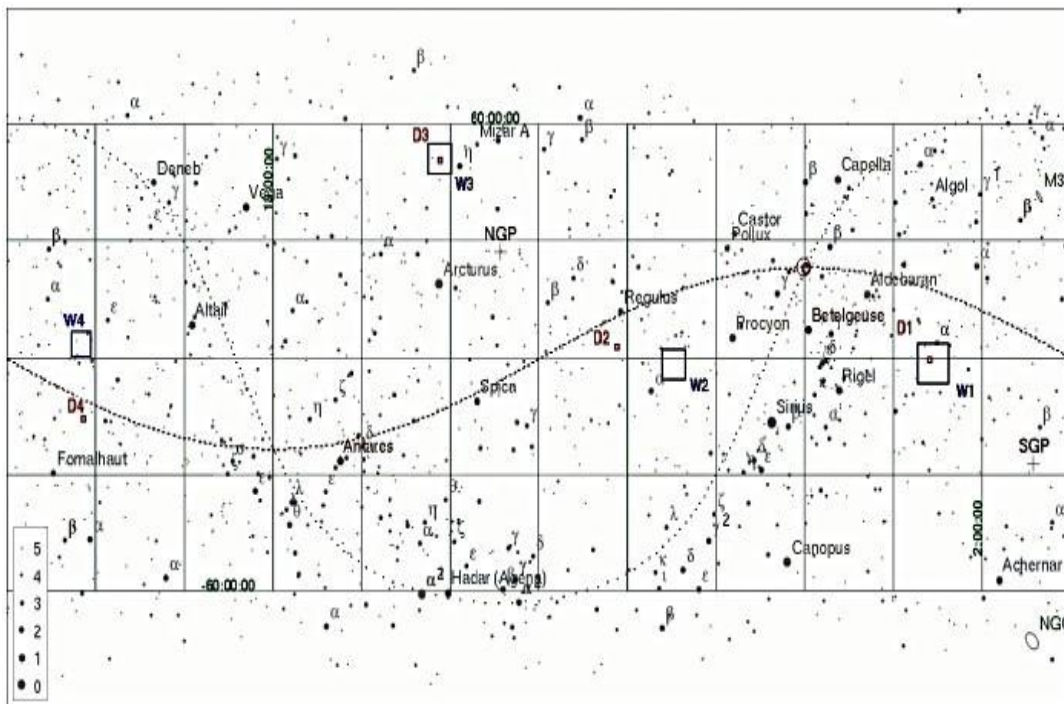


Figure 3.1. CFHTLS Deep and Wide fields. Wide areas (W1, W2, W3, and W4) and deep areas (D1, D2, D3, and D4) are illustrated.

Table 3.1. Sky coordinates of the CFHTLS deep (D1, D2, D3, and D4) and wide (W1, W2, W3, W4) areas.

CFHTLS D/W	Field	α (h m s)	δ ($^{\circ}$ ' ")
D1 field	1 $^{\circ}$ x 1 $^{\circ}$	02 26 00	-04 30 00
D2 field	1 $^{\circ}$ x 1 $^{\circ}$	10 00 20	+02 12 21
D3 field	1 $^{\circ}$ x 1 $^{\circ}$	14 17 54	+52 30 31
D4 field	1 $^{\circ}$ x 1 $^{\circ}$	22 15 31	-17 44 05
W1 field	8 $^{\circ}$ x 9 $^{\circ}$	02 18 00	-07 00 00
W2 field	5 $^{\circ}$ x 5 $^{\circ}$	08 54 00	-04 15 00
W3 field	7 $^{\circ}$ x 7 $^{\circ}$	14 17 54	+54 30 31
W4 field	1 $^{\circ}$ x 25 $^{\circ}$	22 13 18	+01 19 00

3.2. Imaging at CFHT in Wide Field

The survey consists of a large mosaic camera called MegaCam, which is a wide-field CCD camera consisting of 36 thinned EEV detectors arranged 1 degree by 1 degree field of view with a 340 Megapixel camera. MegaCam has a pixel scale of 0.186 arc second per pixel. MegaCam filters cover two survey categories: The Wide Survey (W) consists of four separated zones, namely W1, W2, W3 and W4, and the Deep Survey (D) consists of four separated zones referred as D1, D2, D3 and D4. The reference center of each Wide field of view is defined as the reference W [1, 2, 3, 4] (0, 0) and the Cartesian field names increase toward the East and North. CFHTLS Wide field descriptions are summarized in Table 3.2, where the effective areas of the wide field (W1) are shown. The global characteristics of the CFHTLS Wide field (W1) are summarized in Table 3.3 and in more detail in Table 3.4. Generally, the global properties follow survey specifications, but the survey's homogeneity over a Large Patch Scale needs to be carefully evaluated. The positions and geometry of the four wide fields comprising T0007, namely W1, is shown in Figure 3.2.

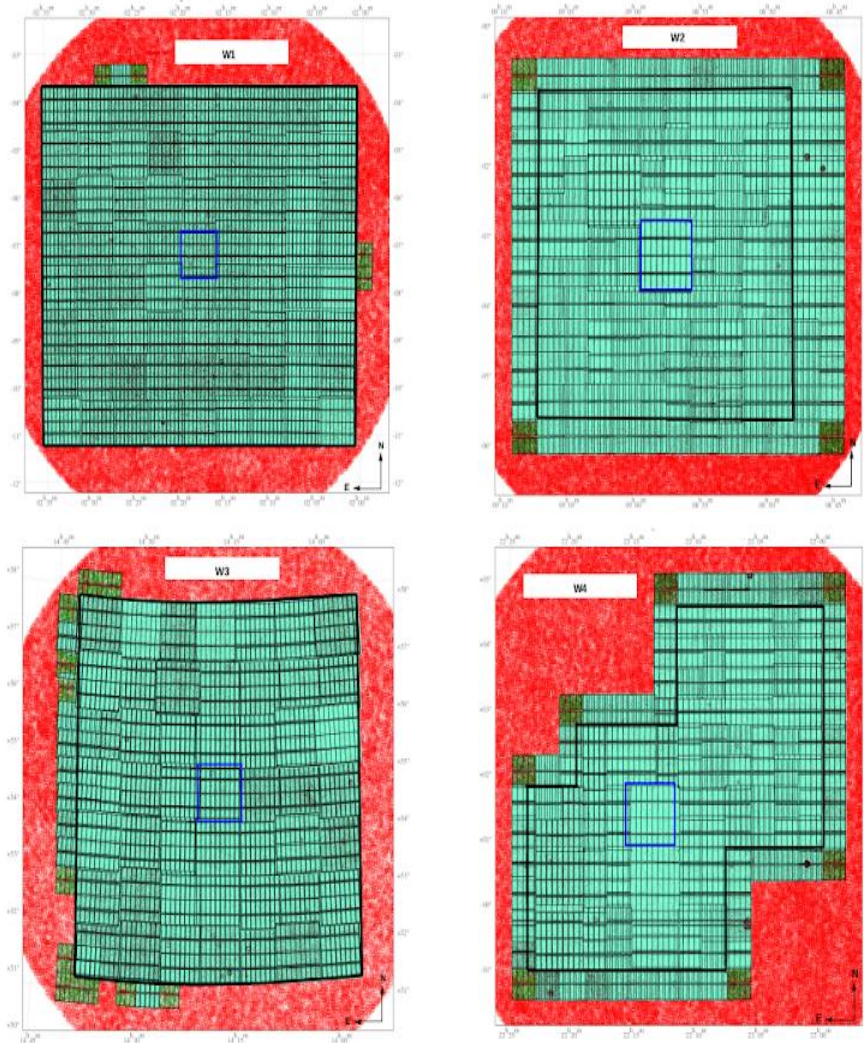


Figure 3.2. Positions and geometry of the CFHTLS Wide fields. The black thick contours show the total field of view composing the ugriz filter collection of the T0007 release. The blue squares show a typical MegaCam field of view and indicate the positions of the reference center field. The MegaCam images included in the release are in green. They reveal the tiling and mosaicing of each CFHTLS Wide area. The small rectangles indicate individual MegaCam CCDs. W1, W2, W3 and W4 do not cover the same field of view, so the four Wide regions are not shown with the same scale in this figure. These plots have been produced during the calibration step of W1, W2, W3 and W4.

3.3. Overview of TERAPIX Pipeline

All the images of the survey are collected and reduced by Terapix-IAP in Paris. Object catalogues are also extracted from images and distributed over the community via Canadian Astronomy Data Center (CADC). Firstly, each incoming file is checked for integrity and content, then registered in the database. Image quality is automatically

assessed at a per CCD level as well as globally over the Megacam sector for science exposure. Image evaluation and reliability confirmation are analyzed statistically to define the Point Spread Function (PSF) context homogeneity and form, astronomical source statistics, and defects such as saturated pixels, impacts of cosmic rays, glitches, trails, bright spikes and aureoles (Coupon et al., 2009).

Pre-processing of raw images (masking bad pixels, removing the overscan, subtracting the dark and the bias, flat fielding and illumination correction) is performed by the Elixir pipeline at CFHT. The data are then transferred to Terapix to produce the stacked images and the final catalogues (Coupon et al., 2009). Thus, any CFHTLS users (or PI users for PI data processed at TERAPIX) may access those maps independently. Using the map to reject image artifacts, a shallow source catalog is then extracted. For each CCD, a PSF model is built and used to track sharpness and elongation of the image over the focal plane. Products in the data ingestion mode are also used to track many astronomical and technological image properties and to generate statistics that are constantly updated. Among these image properties are a history of image quality and observation of time distribution for each program and filter. Figure 3.3. Shows the positions of each “tile” (blue square corresponding to the field of view of Mega-cam) covering the W1 and W2 Wide fields. Each tile is labelled by its Cartesian name on top.

Table 3.2. Overview of the CFHTLS Wide fields. Sky coverage is expressed along R.A. and Dec axes.

CFHTLS field name	Reference center RA [J2000] DEC [J2000]		Total sky coverage [deg ²]	Filters
W1	02:18:00	-07:00:00	8.5×7.5	<i>Ugriz</i>

Table 3.3. Summary of the W1 mean survey parameters.

Field Parameter	u	g	r	i	y	z
Nb stacks	72	72	72	56	16	72
Seeing	0.84±0.11	0.77±0.10	0.70 ±0.07	0.65±0.08	0.66±0.10	0.69±0.13
80% comp. (stellar)	25.27± 0.21	25.52±0.18	25.03±0.16	24.73±0.18	24.82±0.22	23.90±0.26
80% comp. (extended)	24.45±0.15	24.67±0.14	24.00±0.10	23.69±0.13	23.78±0.20	22.91±0.15
Int. astrom. error	(0.031",0.029")	(0.031",0.029")	0.025",0.022"	(0.020",0.017")	(0.20",0.017)	(0.025",0.22")
Ext. astrom. error	(0.237",0.227")	(0.254",0.244")	0.259",0.27"	(0.252",0.243")	(0.272",0.254)	(0.260",0.247")
Mag. Error	0.05±0.01	0.03±0.01	0.03±0.01	0.03±0.01	0.03±0.01	0.04±0.01
CFHTLS SDSS δm [mag]	-0.02±0.015	+0.003±0.006	+0.041±0.014	+0.000±0.007	-0.002±-0.008	0.015±0.011

Table 3.4. The observed area in the surface covered by the MEGAPrime focal Plane on the sky.

Field	Parameter	u	g	r	i	y	z	ugriz coverage
W1	Row observed area	-	-	-	-	-	-	64.16
	Final unmasked area	58.47 (210500)	58.41 (210267)	58.49 (210581)	45.41 (163490)	13.08 (47096)	58.47 (210504)	58.33 (209975)

3.4. Seeing and Image Quality

Seeing is measured by a two-dimensional Mofat model of the Point Spread Function (PSF) and the Full Width Half Maximum (FWHM). FWHM is defined from the ellipticity parameters of the PSF as $FHWM = \sqrt{ab}$, where a and b are the size of the major and minor axes, respectively, of the model. More details about PSF are given in section 3.8.4.

3.5. Photometric Redshift

Redshift may be estimated from broadband photometry and known as photometric or spectroscopic redshift. A photometric redshift is an estimate of a galaxy's redshift by comparing its apparent brightness in several bandpasses. It is an estimate for the recession velocity of an astronomical object without measuring its spectrum. The technique uses photometry, where the brightness of the object is viewed through various standard filters, to determine the redshift, and hence, according to Hubble's law, the distance of the observed object can be determined.

The Universe is expanding; the galaxies are running away from us. The recession speed, as measured by the Doppler shift of a galaxy's spectral lines, is larger for more distant galaxies. One can extrapolate this motion in the past to estimate the time the Universe began in the Big Bang. That enables us to link between the galaxy recession speed or redshift and the time after the Big Bang. Upon emitting light, the redshift becomes a measure of the galaxy's age (Sparke and Gallagher, 2007).

Numerous studies have emphasized the role of redshift to determine the distance, age and the evolution of a galaxy. Some galaxies' parameters are of great importance, so they should be measured, for instance, the celestial coordinates which can be easily determined, compared to difficulty measured the distance. According to Hubble's law, there is a relationship between the redshift of objects and the distances to them (Luoma, 2018).

The deep Hubble Space Telescope images provide information from a wide range of redshifts. Each observation is a snapshot of a galaxy at one time point. Since observation of the evolution of a single galaxy is impossible due to long time scales, series of snapshots of galaxies in different redshifts are needed to trace the galaxy evolution. Additionally, inspecting the stellar mass estimates and the star formation rates, as functions of redshift, shows the star evolution and stellar content of spiral galaxies in clusters (Luoma, 2018).

3.5.1. Accuracy of photometric redshifts

TERAPIX has calculated the photometric redshifts (z_p) of the CFHTLS applying LePhare. LePhare is a tool for SED fitting that uses χ^2 minimization to achieve the best fit with the comparative model spectra (Ilbert et al., 2006). The photometric redshift

computation for the CFHTLS fields used five distinct spectra (E, Sbc, Scd, Irr, and SB) (Coupon et al., 2009). In order to involve redshift limits up to $z \sim 1.2$, these five models are extrapolated into 66 templates. Spectroscopic redshifts (z_s) acquired by VVDS were used to calibrate the templates (Le Fèvre et al., 2005). Comparison of photometric redshifts estimated for CFHTLS with spectroscopic redshifts available for the W1 field reveals a mean error of 0.03 (Coupon et al., 2009). Table 3.5. provides accurate photometric redshift information for a range of CFHTLS-W1 magnitude constraints. The table's outlier percentage was calculated as the ratio of galaxies having $|\Delta z| \geq 0.15 \times (1 + z_s)$ where Δz is the distinction between z_s and z_p .

Table 3.5. For different magnitude cuts in the r-band, photometric redshift accuracy and outlier fraction (Coupon et al., 2009).

i_{AB}	$\sigma_{\Delta z(1+z_s)}$	η (%)
20.5	0.025	1.12
21.0	0.026	1.57
21.5	0.029	1.39
22.0	0.032	2.25
22.5	0.037	2.81
23.0	0.043	4.91
23.5	0.048	7.63
24.0	0.053	10.13

3.6. Sample Selection

In this work, we looked into how BCG clusters found in the CFHTLS's W1 field changed structurally over time. The W1 field's geometry and coordinates are shown in Figure 3.4, which contains 9×8 individual pointings. Since the pointings overlap, W1's total effective survey region is 63.75 deg^2 . For extended sources, 24 mag is the 80% completeness threshold for r-band, although the average r-band images seeing for the W1 field is $0.71''$. The W1 galaxy catalogue, which masks regions surrounding luminous stars, spikes, and areas that have lack cosmetic quality, allowed the detection

of galaxy clusters and, consequently, their BCGs. As a result, there are 2,871,455 ($r \leq 24$) galaxies in our object catalogue.

Photometric redshift catalogues, images, object and mask files can be considered among the data products of CFHTLS. TERAPIX processes, produces, and distributes these products. Since the most recent data release, the whole data has been obtained to the public. It is accessible through the Canadian Astronomy Data Centre (CADC) (Hudelot et al., 2012).

Rather than focusing on identifying low surface brightness features, the CFHTLS's image processing pipeline was improved for better object identification with accurate photometry. Such features may have been eliminated from the images by the removal of the sky background, which may have affected our ability to determine the effective radius. Therefore, based on the CFHTLS images, at lower redshifts, the surface brightness profile of BCGs could not be precise (e.g. $z < 0.3$) (Furnell et al., 2021).

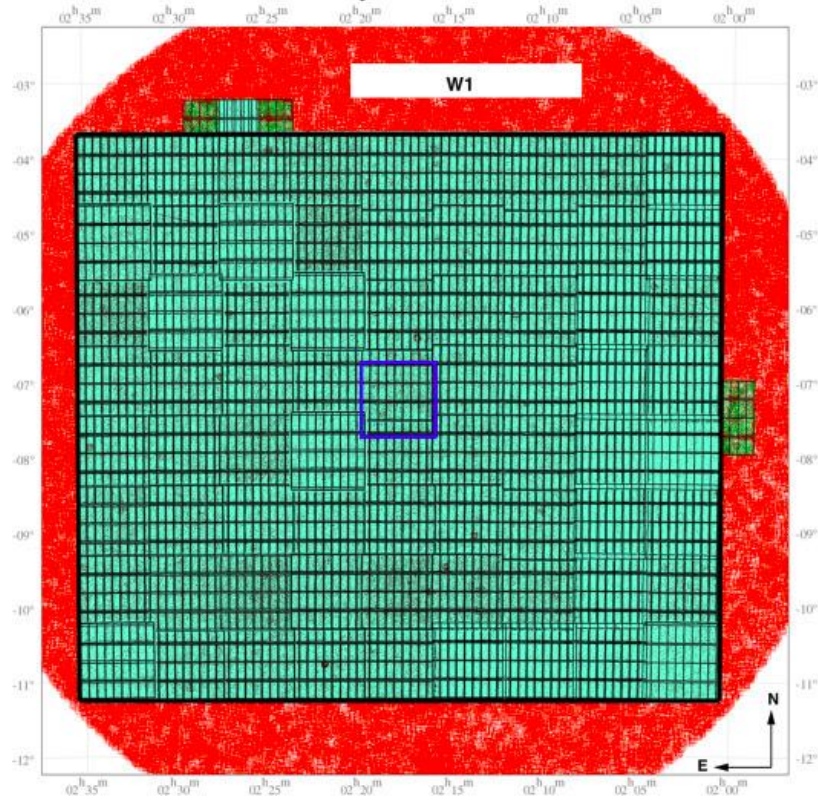


Figure 3.4. CFHTLS W1 pointings' geometry. For this field, there are 9×8 MegaCam pointings. Region of the released image with T0007 release is represented by a solid black line. Astrometric calibrations have been applied in areas beyond the black line. Because several MegaCam pointings overlap, the overall effective area that was covered with W1 is 63.75 deg^2 . The reference field with central coordinates of $\text{RA} = 02^{\text{h}} 18^{\text{m}}$, $\text{Dec} = -07^{\circ} 00'$ is displayed in the centre as a blue rectangle (Hudelot et al., 2012).

3.7. BCG Sample

Brightest cluster galaxies (BCGs) have gained great interest over the recent years. Some studies have reported a relation between their morphologies and structural properties (Fasano et al., 2010; Zhao et al., 2015), others explored how the BCGs grew and how its size changed (Ascaso et al., 2011; Furnell et al., 2018).

Several studies analyzed the behavior of some BCG parameters which can be derived from the best fitting single Sérsic models. Among these parameters are the effective radius (R_e) (de Vaucouleurs, 1948), the Sérsic index known as (n) (Sérsic, 1968) and the morphological classifications (Zhao et al., 2015). The Sérsic index calculates the light profile's concentration. Generally, disc (spiral and S0) BCGs regularly have small values of n , elliptical and cD have large values of n ($n \geq 4$). The effective radius (R_e) is an applicable parameter to measure the extent of the light distribution. Disc BCGs

often have tiny diameters, whereas cD galaxies typically have much bigger sizes. Furthermore, cD and elliptical BCGs may be distinguished by R_e which is considered as a good discriminator (Zhao et al., 2015).

Despite having a predominantly elliptical shape, a significant percentage of BCGs contain an extended envelope around the centre area. As well as they have a low-surface-brightness envelope. (Dressler, 1984; Lauer and Postman, 1992; Oegerle and Hill, 2001; Zhao et al., 2015) resulting in brightness profiles that are distinct from those of regular ellipticals. The Sérsic index could be applied to determine its structure (Peng et al., 2002, 2010). Size-luminosity relations have been created using sizes obtained from these light profiles, which have been demonstrated to be distinct for early-type galaxies and BCGs (Bernardi et al., 2007; Samir et al., 2020). Moreover, Tortorelli et al. (2018) investigated Hubble Frontier Fields member galaxies of the two intermediate-redshift clusters were compared to early-type galaxies' Kormendy relations. Furthermore, Authors discovered that galaxies identified as early-type by the Sérsic index, elliptical by visual inspection, and passive by spectral properties -like star formation - have the same slopes of the Kormendy relations.

According to several studies, the formation histories of elliptical and cD BCGs may differ due to changes in structural characteristics. For instance, the inner (Sérsic-like) component could be formed by way of significant mergers rich in gas. Another theory of formation stated the dissipative processes. Consequently, we can say that the formation of the outer envelope and the increasing of galaxy sizes may both be influenced by the process of dissipationless minor mergers (Zhao et al., 2015).

3.8. Brief Introduction to GALFIT: 2D Image Decomposition

Having an image of a galaxy, one dimensional surface brightness profile can be created in numerous ways by many tools. The easiest approach is to cut a slice along the galaxy's major axis and to measure the surface brightness at various points in the galaxy. It has been observed that galaxy profiles along its major and minor axes could differ significantly (Burstein, 1979; Ferrarese et al., 1994). Another approach for that the galaxy as a complete in the image can be drawn to encircle the galaxy's isophotes with ellipses, whereby a surface brightness can be determined based on the galaxy's semi-major axis. On the other hand, there are some drawbacks to the one-dimensional profile. For instance, when using azimuthally averaged profiles, it does not consider

that the isophotes' ellipticities and position angle variations have changed. Moreover, the residual that results from subtracting the best-fit profile from the observed profile does not provide much information about the galaxy's unaccounted structure. It is preferred to analyse the observed galaxy image and fit a two-dimensional analytical model over it. The majority of the 1-d analysis's aforementioned drawbacks can be resolved (Vaghmare, 2015). Among the most common tools used for a 2-d analytical model is the GALFIT program. GALFIT is essentially used to gain more information and hints about the origin of galaxies from the analysis of its hidden fine structures. GALFIT is a method for breaking down a galaxy's surface brightness profile into its constituent parts (Tawfeek, 2019).

3.8.1. Analytical light profile functions

Studies of galaxies using a 2-D modeling has been applied as it can recover the true parameter values without any degeneration (Peng et al., 2002). GALFIT, the fitting algorithm, is capable of modeling celestial object profiles in two-dimensional (2D) formats from their raw images (Peng et al., 2002). The main functions used in GALFIT to fit a galaxy are; Sérsic, Exponential disk, Nuker, Modified Ferrer, and Edge-on disk. Basically, one model for a specific galaxy is used, otherwise, additional models to minimize the residuals for a complex galaxy with multi-components can be added (Tawfeek, 2019). Fitting a model to a galaxy image at the simplest conceptual stage is about defining a merit function. χ^2 , which is the precision of GALFIT fits, whose value varies from 1 to 2. Concluding that the less merit function causes a better fit parameter and thus a model to galaxy image can be fit.

The input parameters needed to run GALFIT must be chosen carefully to get verified fitting results. The main inputs are; the FITS image, obtained from observations, the sigma (σ) image and the Point Spread (PSF) image. All these parameters enable GALFIT to distinguish between stellar and galactic objects and eventually, the chosen analytical function to fit the light profile of the target object (Yelkenci, 2015).

The most significant factors that should be considered before running GALFIT are:

3.8.1.1. Images in FITS format with pixel values in counts

Pixel values of the target FITS images are strongly recommended to be measured in counts, but not in flux units. That is because the sky in flux units tends to be misleadingly tiny and negligible (Peng et al., 2002). Thus, indicating that it is easier to deal with images without sky's correction. In case the sky is corrected, the matter will be more complicated due to flat field mistakes, neighboring pollution, and discrepancy between the model profile and the results. So, it's preferable to deal with images without sky's correction. A small error in the measurement of the sky by even a few electrons could have a significant impact on the fitting results.

The crucial need to the count units of the image is also to construct a sigma image using GALFIT as seen in (Equation 3.1).

$$Gain \left[\frac{e^-}{count} \right] \cdot ADU[count] \cdot NCOMBINE = [electrons] \quad (3.1)$$

where GAIN for a single image is the detector gain parameter from the image header and is defined as the magnitude of amplification produced by a galaxy. It is usually measured in units of electrons/ADU. ADU is the “Analog-to-Digital Unit” used for measuring a pixel value. NCOMBINE is the number of combined images.

3.8.1.2. Proper sky value for image

Since the sky value affects the fit parameters so much, we need to verify the sky value is correct and reasonable before starting GALFIT. The overestimated sky background produces a lower Sérsic index, a fainter luminosity, whereas the underestimated sky and a smaller radius induce the opposite effect. It's remarkable to mention that the sky as a free parameter can be fitted by GALFIT.

3.8.1.3. Correct sigma image

Sigma image can be created manually or automatically. In manual mode, users should apply a sigma image by overriding GALFIT to avoid information from NOISE, GAIN, and NCOMBINE. This approach is recommended for users with a simple understanding of sigma image. Alternatively, GALFIT can automatically generate an internal sigma image, bearing in mind the image has a pixel value of counts. The latter approach is preferred, and it is faster.

3.8.1.4. Ideal PSF image for convolution

The PSF image is not only a star image, but also a perfect image of a point source. Though it is not hard to build a PSF picture, it is rather difficult to accept that anything could be ideal. The best PSF image is isolated from any contamination of light, and it should have very high signal-to-noise. Furthermore, an ideal PSF image should have a zero background and a flat. Moreover, it should be centred in the image and have the exact form of a stellar image.

3.8.1.5. Removed neighboring contamination

For proper fitting, the target galaxy should be clean of any object that may mask it. That will make GALFIT fit quickly and smoothly to the target object. Meanwhile, in case of modeling a galaxy in a crowded field, projected neighboring light will bias the model. Therefore, all objects surrounding the target galaxy must be flagged before fitting it.

3.8.1.6. Appropriate convolution box

Convolution box is the fit box through which GALFIT runs. The box size is highly dependent on the object. Objects with high concentrations often require larger convolution boxes compared to objects with flatter centers as more flux is distributed from the center to the edges. The commonly used size of the convolution box is 40 to 80 FWHM times of the image fits (Tawfeek, 2019).

3.8.1.7. Simple model for the fitting start

It is recommended to begin fitting with the simplest and the most basic model for comprehensive decomposition of a multi-component galaxy. If fitting with the simplest model is not enough, we can then build up complexity as required by the situation. Such recommendations will enable running GALFIT quickly. Moreover, this helps to save time and avoid duplication with two separate components.

3.8.2. GALFIT inputs and outputs

GALFIT inputs

GALFIT requires a number of input parameters which are shown in Figure 3.5 and described below:

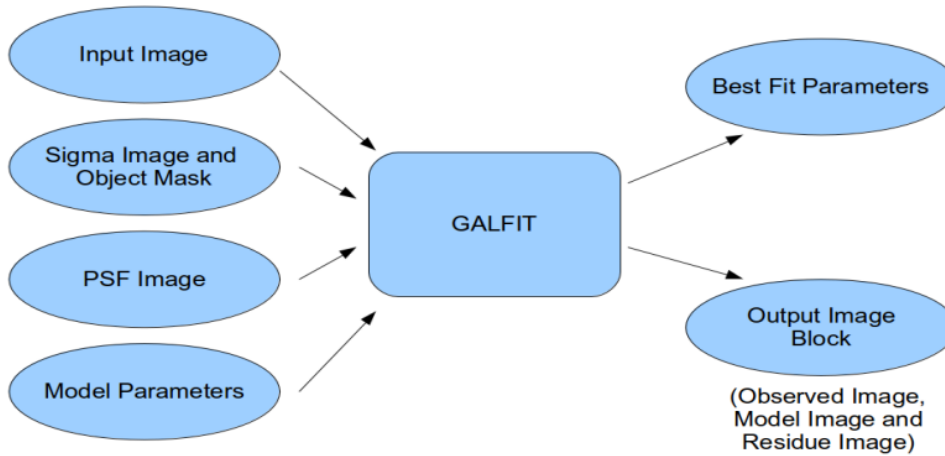


Figure 3.5. A diagram illustrating the use of GALFIT.

3.8.2.1. Fits image

An image in fits format must be added, as one of the main inputs for GALFIT decomposition. The analyzed image should only include the target object in order to mask any other projected one. The units of pixels should be in counts.

3.8.2.2. Sigma image

During the fitting process, Sigma image is used to flag the unallowable pixels. It is highly recommended to leave the input empty. GALFIT can automatically create a reasonable one if the pixel values are in units of counts. In the current study, GALFIT is applied to create a sigma image.

3.8.2.3. PSF image

The most important GALFIT input for correct fitting is the PSF image. In the case of space-based telescopes, since the PSF is typically under sampled, the PSF image is permitted to have a lower pixel scale than the image itself (Vaghmare, 2015). There are several ways to extract a good PSF image, one of which is using a pure analytical profile. Because all ground-based images follow a Gaussian profile, the image's FWHM can be applied to create an analytical function (Tawfeek, 2019).

3.8.2.4. Configuration input file

The models to be fitted, the beginning guess parameters, and a list of constraints are all described in a configuration input file. Figure 3.6. illustrates a GALFIT input file example.

```
# Input menu file: galfit.feedme
# Chi^2/nu = 1.469, Chi^2 = 12695.048, N dof = 8641
=====
# IMAGE and GALFIT CONTROL PARAMETERS
A) gal.fits          # Input data image (FITS file)
B) imgblock.fits    # Output data image block
C) none             # Sigma image name (made from data if blank or "none")
D) psf.fits         # Input PSF image and (optional) diffusion kernel
E) 1                # PSF fine sampling factor relative to data
F) none            # Bad pixel mask (FITS image or ASCII coord list)
G) none            # File with parameter constraints (ASCII file)
H) 1 93 1 93       # Image region to fit (xmin xmax ymin ymax)
I) 100 100         # Size of the convolution box (x y)
J) 26.563          # Magnitude photometric zeropoint
K) 0.038 0.038     # Plate scale (dx dy) [arcsec per pixel]
O) regular         # Display type (regular, curses, both)
P) 0               # Choose: 0=optimize, 1=model, 2=imgblock, 3=subcomps

# INITIAL FITTING PARAMETERS
#
# For component type, the allowed functions are:
#   sersic, expdisk, edgedisk, devauc, king, nuker, psf,
#   gaussian, moffat, ferrer, and sky.
#
# Hidden parameters will only appear when they're specified:
#   Bn (n=integer, Bending Modes).
#   C0 (diskyness/boxyness),
#   Fn (n=integer, Azimuthal Fourier Modes).
#   R0-R10 (coordinate rotation, for creating spiral structures).
#   T0, T1, T0-T10 (truncation function).
#
# -----
# par)  par value(s)  fit toggle(s)  # parameter description
# -----

# Component number: 1
0) sersic          # Component type
1) 46.5265 48.2556 1 1 # Position x, y
3) 22.9761 1       # Integrated magnitude
4) 2.6233 1        # R_e (effective radius) [pix]
5) 4.1097 1        # Sersic index n (de Vaucouleurs n=4)
6) 0.0000 0        # -----
7) 0.0000 0        # -----
8) 0.0000 0        # -----
9) 0.8572 1        # Axis ratio (b/a)
10) -71.7466 1     # Position angle (PA) [deg: Up=0, Left=90]
Z) 0              # Skip this model in output image? (yes=1, no=0)

# Component number: 2
0) sky            # Component type
1) 0.7300 1       # Sky background at center of fitting region [ADUs]
2) 0.000e+00 0    # dskv/dx (skv gradient in x) [ADUs/pix]
```

Figure 3.6. GALFIT input file example.

3.8.2.5. Fitting profile

In order to fit a galaxy's light profile via GALFIT, a suitable radial profile function such as de Vaucouleurs, Sérsic, Gaussian, exponential disk, modified Ferrer, empirical

King, Nuker, Moffat, edge-on disk or background sky component must be selected (Peng et al., 2002). However, it is difficult to define which profile would be chosen and how many components should be taken to fit. Thus, it is better to start fitting through a single component to guess the best fitting and gradually add other components. These profiles can be combined, and the user has the choice to freeze or free any subset of parameters. Additionally, the user may provide constraints to connect the model parameters or to establish a parameter range restriction. Frequently, Sérsic profile is used for early-type galaxies, and a Sérsic or de Vaucouleur profile plus an exponential profile for two components are used for late-type galaxies. On the other hand, the Modified Ferrer profile may be fitted to galaxies with more than two components such as a bar, a tail, or a nuclear source.

- The Sérsic profile

Sérsic profile is among the most currently used models to present the morphology of a single galaxy component. It is a flexible profile in which Gaussian, de Vaucouleurs and exponential profiles can be considered as exceptions to the Sérsic profile as shown in the (Equation. 3.2). The Sérsic law of power has the following function:

$$I(R) = I_e e^{-bn} \left(\left(\frac{R}{R_e} \right)^{\left(\frac{1}{n} \right)} - 1 \right) \quad (3.2)$$

$I(R)$ represented the surface brightness at the effective radius R_e , (n) shows the concentration parameter that describes the inner profile, where a large (n) reflects a steep inner profile and a highly extended outer wing. However, a small (n) determines a shallow inner profile at a broad radius and a steep truncation. The dependent variable (b) is combined to (n) to make Sérsic profile valid. When the Sérsic index is 4, the Sérsic profile represents a de Vaucouleurs profile, a Gaussian profile at $n = 0.5$, and an exponential disc at $n = 1$ (Peng et al., 2002).

- The exponential disk profile

The Exponential Profile is used to fit the galaxy disk. Late type (spiral and irregular) galaxies typically fit with this profile. If $n = 1$, the exponential profile is a specific example of the Sérsic function (see Equation. 3.3). The general form of the exponential profile is:

$$\Sigma(R) = \Sigma \exp\left(\frac{-R}{R_s}\right) \quad (3.3)$$

where R_s is the scale length considering reviewing as a function of the effective radius (R_e) as $R_s = (R_e / R_s)$ for $n = 1$ (Peng et al., 2002).

- Gaussian profile

A further unique instance of the Sérsic profile is the Gaussian profile in (Equation. 3.4) with $n = 0.5$, but FWHM is used instead of R_e (Peng et al., 2002), according to the following (Equation 3.4).

$$\Sigma(R) = \Sigma_0 \exp\left(\frac{-R^2}{2\sigma^2}\right) \quad (3.4)$$

where $\text{FWHM} = 2.354 \sigma$.

- The modified Ferrer profile

The Ferrer profile is taken into account for fitting bar galaxies with a flat center and an outward truncation as illustrated in (Equation 3.5). It depends on the two parameters α for the truncation sharpness and β for the central slope (Binney and Tremaine, 1987). The form of this profile can be written as:

$$\Sigma R = \Sigma_0 \left[1 - \left(\frac{R}{R_{out}^{2-\beta}} \right)^\alpha \right] \quad (3.5)$$

- The Nuker profile

This profile is used to fit the nuclear profile of surrounding galaxies with the following double power law, as seen in (Equation 3.6).

$$R = I_b 2^{\left(\frac{\beta-\gamma}{\alpha}\right)} \left(\frac{R}{R_b}\right)^{-\gamma} \left[1 + \left(\frac{R}{R_b}\right)^{-\alpha} \right]^{\left(\frac{\gamma-\beta}{\alpha}\right)} \quad (3.6)$$

where β denoted the outer power law slope, γ indicated the inner slope, and α controled the sharpness of the transition (Lauer et al., 1995).

- The edge-on disk profile

This profile is used to fit a galaxy on a flat disk with an edge on view in (Equation 3.7). Its functional form is:

$$\Sigma(R, h) = \Sigma \left(\frac{R}{R_s}\right) K_1 \left(\frac{R}{R_s}\right) \text{sech}^2 \left(\frac{h}{h_s}\right) \quad (3.7)$$

where Σ_0 implies the surface brightness profile, R_s denotes the major axis disk scale-length, h_s represents the perpendicular disk scale height, and K_1 denotes a Bessel function.

- Additional profiles

Beside the aforementioned profiles, two more profiles exist; the Empirical King Profile used for globular clusters (King, 1962) and the Moffat Profile (Moffat, 1969).

3.8.3. Goodness of fit

The quick Levenberg-Marquardt algorithm is used by GALFIT to identify the best-fit parameters by minimizing χ^2 . This algorithm has a limitation because it is frequently becoming trapped in a local minimum. Therefore, the solutions must be carefully reviewed for accuracy and physical significance. The optimization technique is an enhanced least squares fitting method developed by Levenberg and Marquardt for non-linear problems (Tawfeek, 2019; Vaghmare, 2015). Example of a model fit of five galaxies is given in Figure. 3.7.

GALFIT measures the quality of fit by the normalized or decreased χ^2_v (Peng, 2003) as shown in the (Equation 3.8). χ^2_v has the following form:

$$\chi^2_v = \frac{1}{N_{DOF}} \sum_{x=1}^{nx} \sum_{y=1}^{ny} \left(\frac{(f_{data}(x,y) - f_{model}(x,y))^2}{\sigma(x,y)^2} \right) \quad (3.8)$$

where N_{DOF} denotes the range of freedom, $f_{data}(x, y)$ represents the image used as input, $\sigma(x, y)$ implies the sigma image either internally generated or received as an input, and $f_{model}(x, y)$ denotes the image used as the model (Peng, 2002). The output file's header (.fits) receives the χ^2 value and saves it there. The anticipated value in the reduced χ^2 test is $\chi^2_v = 1$. When $\chi^2_v = 1$, the data and fitted model agree. In the case where $\chi^2_v \gg 1$, the model and data do not match well. Furthermore, values of $\chi^2_v < 1$ indicate that the fit is problematic. Very tiny numbers suggest that the fitted parameters' uncertainties are incorrectly calculated (Bevington and Robinson, 2003; Tawfeek, 2019).

GALFIT starts convolves the produced model image with the current set of parameters to account for the instrument's seeing effects, then subtracts it from the observed image with the PSF using a Fast Fourier Transform (FFT) method. It generates a model that matches the PSF with a pixel scale that appropriately bins it to fit the observed image if the PSF is sampled more finely than the observed image. The convolution procedure, which consumes the majority of GALFIT's processing resources, may be modified the configuration file in a way that will change the results (Vaghmare, 2015).

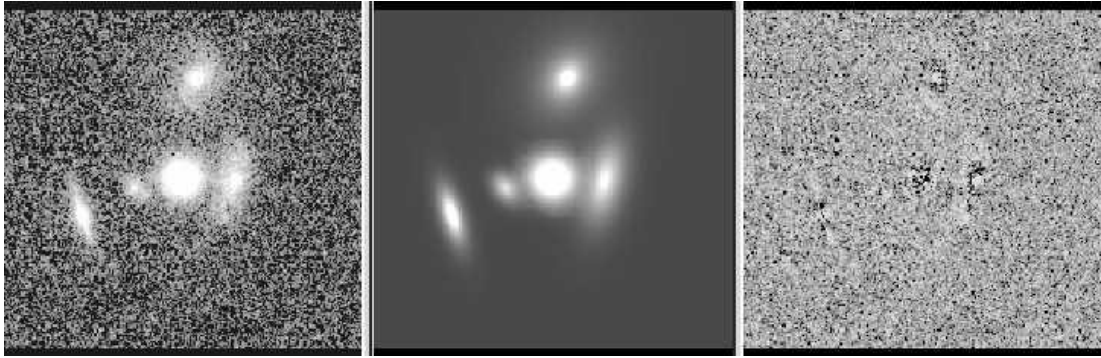


Figure 3.7. Simultaneous example of model that fit of galaxies (original data, GALFIT model and residual, respectively).

3.8.4. Determining the point spread function

A common definition for seeing is the dispersion of light from a point source. On imaging, a point source appears to be extended, this is because the incoming light was detected by the telescope-detector system. PSF is used to describe the complete effect. The final image of an astronomical object created by a telescope may then be defined mathematically as the convolution of two functions. The intrinsic light distribution of the source is represented by the first, while the PSF is represented by the second. A galaxy image represents the distribution of light in the galaxy but convolved with a PSF as seen in Figure 3.8. Consequently, first the image should be deconvolved before the light distribution is studied. Although, deconvolution frequently causes the image to become noisier. It is not a practical approach, particularly for images with a low signal to noise ratio already (Peng et al., 2002). Another GALFIT's approach is to convolve the model image with the PSF before removing it from the observed image when computing the χ^2 value.

The accuracy rises for galaxies with sizes comparable to the Full Width at Half Maximum of the seeing, without a PSF. The parameters are biased by any system particular to the chosen telescope-detector combination. GALFIT is able to obtain the PSF as a 2-d FITS image. This GALFIT feature has significance since it eliminates the requirement to roughly approximate the PSF as certain analytical functions (Vaghmare, 2015).

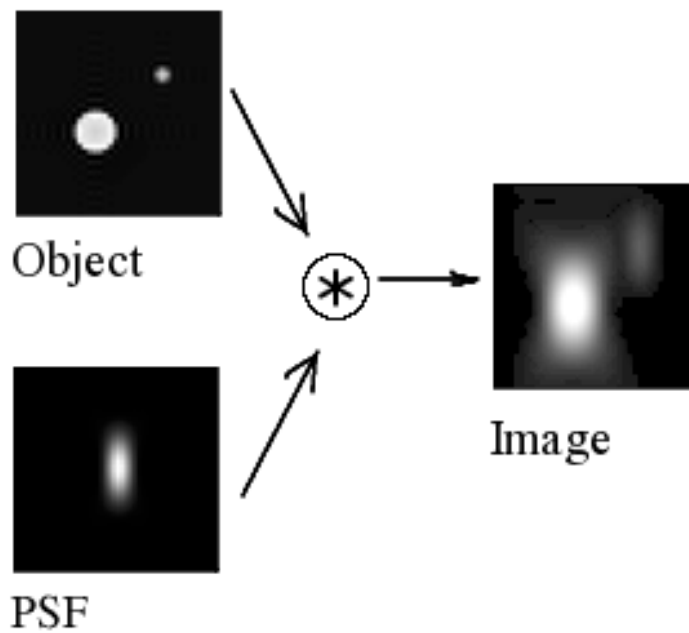


Figure 3.8. The image on the CCD of PSF effects on the body

There are several techniques for calculating the PSF:

1. Coadding images of stars:

The best way to calculate the PSF is to create cutouts of isolated and the bright stars in the foreground. Then create a high signal-to-noise ratio image of a star by coding the data after that. All background must be removed from the final image and correctly focused.

2. Assuming an analytical profile:

For ground-based telescopes, the PSF may be roughly calculated using a profile (e.g. the Gaussian or Moffat function). As a result, the probability distribution of the pathways that photons take away from a source is composed of a variety of distribution functions, each of which represents the scattering of the photons as a result of a particular effect. One can estimate this by using a Gaussian by the central limit theorem.

3. Semi-analytic approach:

Another more involved approach can be introduced if an analytical function is not sufficient. This requires recognizing multiple shining stars in the image's foreground. Simultaneously an analytical profile being fitting, like a Gaussian or Moffat. It is necessary to establish the average parameters required to characterise the stars. The

best-fit function is subtracted from the stellar profiles to calculate the residuals. The best-fit model includes any residuals determined as a result of non-symmetrical or extended structures (Vaghmare, 2015).

The point spread function (PSF) component employed in GALFIT is not expressed as an analytical mathematical function, but rather as a convolution PSF image. GALFIT takes into consideration the complexities of the point spread function and provides a more precise modelling of the observed data by using a convolution PSF image (Peng et al., 2010). A PSF flux peak may be seen in the centre of a user-provided image in (.fits) file format. Consequently, the image includes all of the PSF's light (Luoma, 2018; Peng et al., 2010).

4. RESULTS

One of the main techniques for figuring out the creation and growth of galaxy clusters is through the study of the BCGs. Photometric analysis and structural parameters of these galaxies give clues on how the environment influences the morphological, physical, and dynamical characteristics of the galaxies. In this study, the goal is to provide the surface brightness profile fitting data of 1685 BCGs from the Canada-France-Hawaii Telescope Legacy Survey in range of the redshift $0.1 < z < 1.0$. We used a single Sérsic profile to fit r-band images of BCGs. Towards that, we used GALFIT software to fit Sérsic profiles to a sample of BCGs. To explore the influence of the environment, according to the richness of the host cluster, our sample is separated into two categories. The aim of our study is to examine the temporal changes in structural parameters and scaling relationships concerning BCGs across different environmental circumstances. We present the linear regressions with the perfect fit for the Kormendy, and size-luminosity relations. This chapter is aiming to describe our results after applying the profile of surface brightness fitting of a BCG sample, we have published the results of our study in *New Astronomy* (Shaaban et al., 2022).

4.1. BCG Sample

The current study's BCG sample is taken from galaxy clusters discovered in CFHTLS-W1. To identify clusters within the W1 area, the Wavelet Z-Photometric (WaZP) cluster finder was used as a detection method. By WaZP cluster finder, clusters can be identified and characterized within the specified area of interest. The (WaZP) is designed to identify clusters of galaxies making use of scans of optical galaxies at several wavelengths when photometric redshifts and galaxy coordinate are provided. The (WaZP) searches for projected galaxy overdensities in photometric redshift space without than making any assumptions about the underlying galaxy population. WaZP, in a nut-shell, using galaxies' locations, such as their RA and Dec, can create soft wavelet-based maps of density for every slice of the galaxy database in photometric redshift space. Thus, a distinguished listing the probable cluster candidates and their

associated galaxy members is created by extracting and combining overdensity peaks (Aguena et al., 2021).

When an overdensity is detected, the clusters' radius and richness (λ) are calculated together. The clusters' radius is defined as the radius at which the density is 200 times more than the background galaxy density in the area (R200), where the richness can be denoted as the total of the membership probabilities of galaxies inside the R200.

Based on galaxies' distances from a cluster's core, their membership probabilities for a specific cluster, their magnitudes and their photometric redshifts can be calculated (Castignani and Benoist, 2016). WaZP has a signal-to-noise (SNR) ratio that it uses to identify cluster candidates. The density peak when compared to the local galactic background is used to calculate these ratios. With an SNR >3 , cluster detections have been used. 3337 detections are obtained in the whole W1 area.

According to the following criteria, we recognized those galaxy clusters' BCGs as the brightest elliptical galaxies:

- i. be 0.5 Mpc from the cluster's centroid,
- ii. have a $z = 0.03 (1 + z_c)$ cluster-consistent redshift,
- iii. have a $(r - i)$ colour that is (within ± 0.3) compatible with the colours of model elliptical galaxies for the appropriate redshift.

True colour pictures of the cluster cores have been created with STIFF utilising g, r, and r-band CFHTLS images, in order to analyse cluster detections (Bertin, 2012). The cluster sample used to find BCGs is quite small. Therefore, there has been a visual examination carried out to avoid any incorrect detection. When galaxies are clearly overdensity and have a homogeneous colouring scheme, the cluster candidates, hence BCGs are kept. Eventually, 3283 BCGs are left the W1 region.

4.2. Structural Analysis of BCGs

We outline the primary methods used in this study in this section. In addition to a background (sky) model, each BCG's r-band images are modelled using a Sérsic profile which is single. The sections that follow, we explain the essential procedures of the analysis that we carried out.

4.2.1. Preparing images

For this study, the BCGs' list is determined from the survey containing the parameters of interest such as RA, Dec, z , R_e and others. It is essential that the survey images consisting of individual images cover wide fields of the sky. In order to overcome the complexity in such massive images (.fits files varying in size from 5 GB to 25 GB), it is preferable to cutouts around the target BCG, so the objects are cropped first to $1'' \times 1''$ (1 arcmin= 300 pixels) sized separate images. Using the original images in r band helps create image cutouts. In order to cutout the image around the target BCG a simple script has been used. The output of the script is prepared to correspond to the cutting coordinate input of GALFIT.

An example of cluster center and the BCG (ID 7942, $z_{\text{phot}}=0.282$) illustrated in Figure 4.1. Cluster center is marked with cyan cross, BCG is marked with cyan circle, and the dashed circle represents the 500 kpc projected radius around the cluster center.

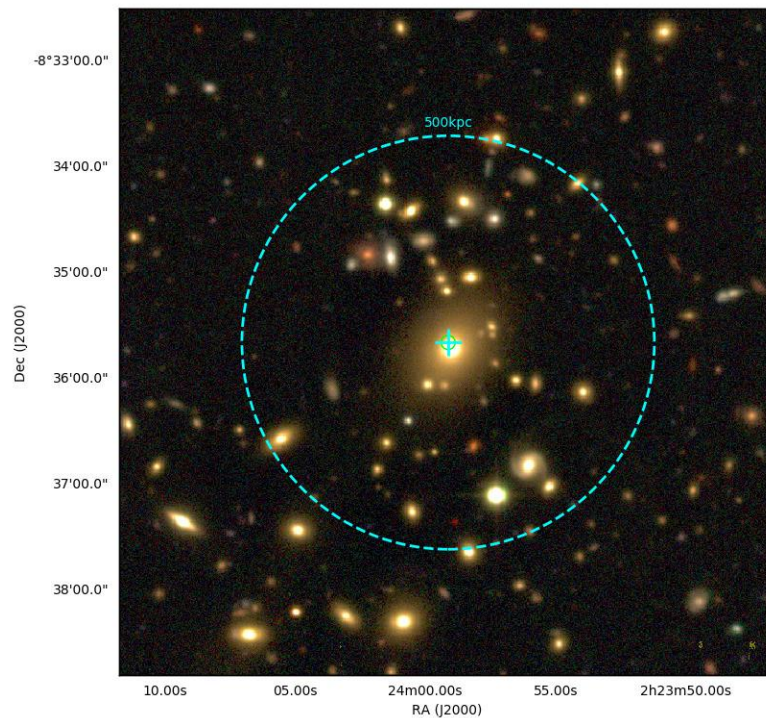


Figure 4.1. An example of cluster center and the BCG (ID 7942, $z_{\text{phot}}=0.282$). Cluster center is marked with cyan cross, BCG is marked with cyan circle, and the dashed circle represents the 500 kpc projected radius around the cluster center.

There are 72 individual MegaCam pointings in the CFHTLS W1 field. We first identify the matching region for each BCG in our sample based on the galaxy's location

and the corner coordinates of each area. Thus, using our unique CFITSIO methods, the image which cutout is generated by using the image in r-band.

We created cutout images with BCGs centred in order to analyse them with GALFIT. When using the MegaCam ($0.186''/\text{pixel}$), this image size can be equivalent to about 56 arcseconds. The scale of angles coincides to the physical size equal to hundred kpc, the standard cosmology at $z \sim 0.1$ redshift. With a physical size that is three or more times greater than usual size of BCG, for instance 10- 30 kpc, GALFIT can use this data to establish the galaxy's background level. Therefore, the region of sky surrounding the object of interest must be appropriate. The importance of GALFIT, which may use the sky as a free parameter.

4.2.2. Mask images

Galaxy images to be investigated using the GALFIT program are needed to have an adequately empty environment, be unaffected by other objects or masked. Furthermore, unwanted events that might create light effects, due to satellite traces as a result of long observation periods, in addition to the saturation light effects of stars, should be avoided. Therefore, image masks are needed.

In an attempt to make masking for unwanted objects, the process is as follows: Firstly, the near objects around the target, which have bright magnitude and can affect our analysis, are selected. Those objects need to be masked. Images are visualized with FITS extension using Smithsonian Astrophysical Observatory (SAOImage) DS9 program, version 8.1, which is an astronomical imaging and data visualization application. Images in the sample to be studied are selected and adjusted using DS9 in order to create ellipses for each object needed to be masked. If the initial parameters (RA, Dec, a, b and theta) are known for the selected unwanted objects, DS9 program will give the values of the magnitudes to be used in the input file for the masking program. All the objects in the image are scanned from the catalog and their coordinates are determined from the image. The information of the objects for the masking is prepared according to the catalog. The masking program can be carried out after converting the DS9 region file to the input file. The mask file can be used to create the mask image. The mask image can be used as an input image for the GALFIT program which is the main tool for the analysis.

For the whole W1, TERAPIX has already developed masking the images for defects of image, stars and unwanted objects. There is a mask file for each of the 72 distinct Mega-Cam pointings' regions. As soon as the matching area for our main objective were detected, we immediately produce cutout files with the same field of view, for this masking. It can be referred to this mask file as the polygon masks since the masking was carried out using polygon-shaped sections. Although, the file for the mask is insufficient for a trustworthy GALFIT result. Luminous galaxies that were near interested objects in similarly masked. It is important when we examine BCGs located in the central regions of galaxy clusters, the Universe's most dense area. If an object is brighter than $i < 20$, we mask everything else except for our target galaxy. We use the semi-major and semi-minor axes, the position angle of the sources, and Kron radius to detect the areas to be masked. These values are derived from the TERAPIX object catalogues. These types of mask files are referred to as object masks. Then, these two mask files are combined to create a single mask file for GALFIT. This method of producing the final files of masking is illustrated in Figure 4.2 which is near to the method used by Yelkenci (2015).



Figure 4.2. This study applied a masking method. The TERAPIX polygon mask file (left of the image) containing stars is combined with the masks for objects (centre), the final mask file (right) formed for BCG ID 7942.

4.2.3. Obtaining the point-spread function model

Point Spread Function (PSF) images which can be frequently used to describe how light from a point source spread. A PSF model must be provided as an input file for GALFIT to represent galactic light distributions. This is essential for objects located in busy regions.

PSFex, created by E. Bertin and based on SExtractor, is what we use. We used SExtractor to create LDAC files for each W1 region, which we then processed into PSFex. We let PSFex pick point-like objects by enforcing a maximum ellipticity of ϵ

= 0.3 on each object. When construction the PSF, point-like sources are chosen if they have a signal-to-noise ratio of $S/N \geq 20$.

Each MegaCam pointing is quite big (1 deg^2) and PSF can change through the image, thus we separated each W1 area (19354×19354 pixels) into 19×19 sub-fields that were around 100×100 pixels each. As a result, we are provided 361 PSFs for a certain MegaCam pointing. The 72 areas in W1 are all tested using this method again.

We establish the representative PSF of that sub-field based on the coordinates of the target and feed it into GALFIT. Figure 4.3 shows a PSF image example for a MegaCam pointing that we show how to select the appropriate sub-field for the galaxy's goal.

4.2.4. Running GALFIT

Some recent studies described GALFIT as an effective tool for data analysis to support images that can be observed. GALFIT requires a variety of input parameters and information to fit the light distribution. This involves a coordinated input for executing the programme, particularly when dealing with a big number of objects. As a result, we combine GALFIT with a wrapper Fortran programme along with some scripts for post-processing.

This Fortran programme allows you to set up input parameters, create configuration and auxiliary files, and execute the entire BCG sample. At this step, the procedure is given the final mask and PSF files described in earlier parts. The initial parameters of effective radius (R_e), axis ratio (b/a), position angle, and magnitude are derived from CFHTLS object catalogues given by TERAPIX.

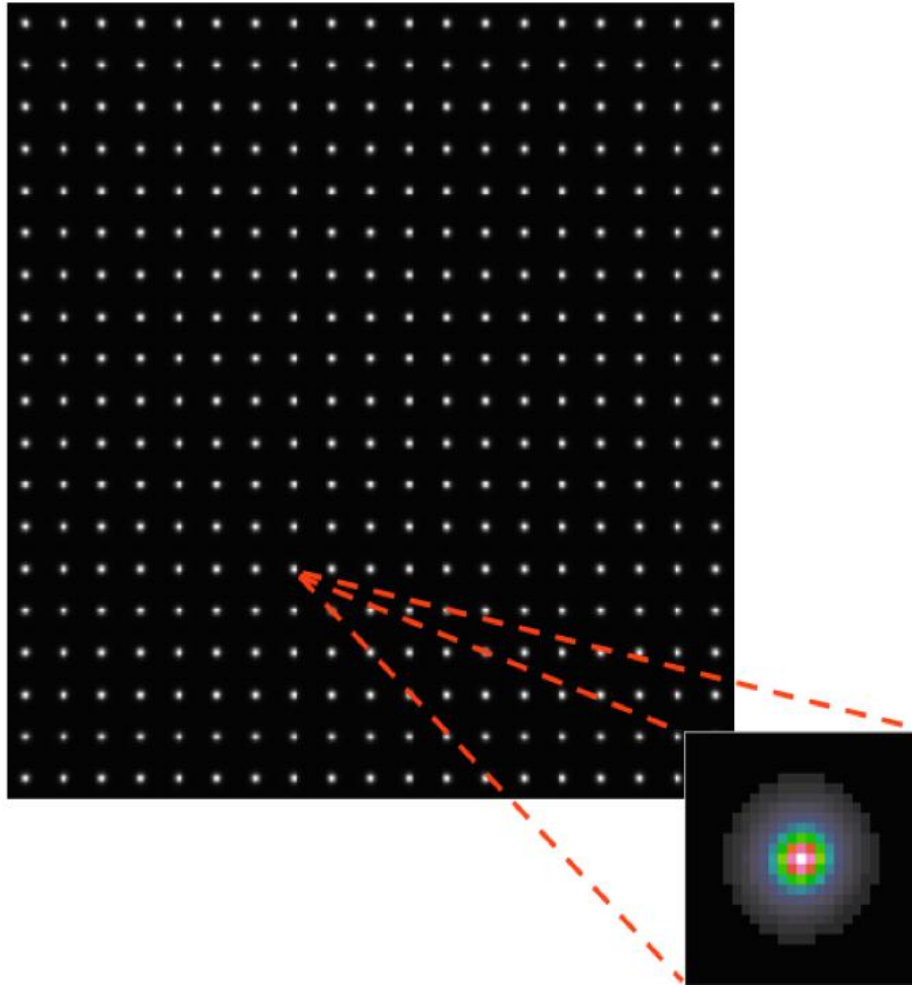


Figure 4.3. PSFex was used to create a point-spread function model for a single Mega-Cam pointing. Inset is the enlarged image of the PSF of a sub-field. Similar PSFs are generated for each of W1's 72 areas.

Figure. 4.4. illustrated the observed, the model and the residual image for BCG 4634 which displayed in DS9, as an example. The target BCG, surrounded with other galaxies, observed in the center of the image (the top right side). The model obtained with Sersic components, and the residual image are also seen on the figure's bottom left and right sides, respectively.

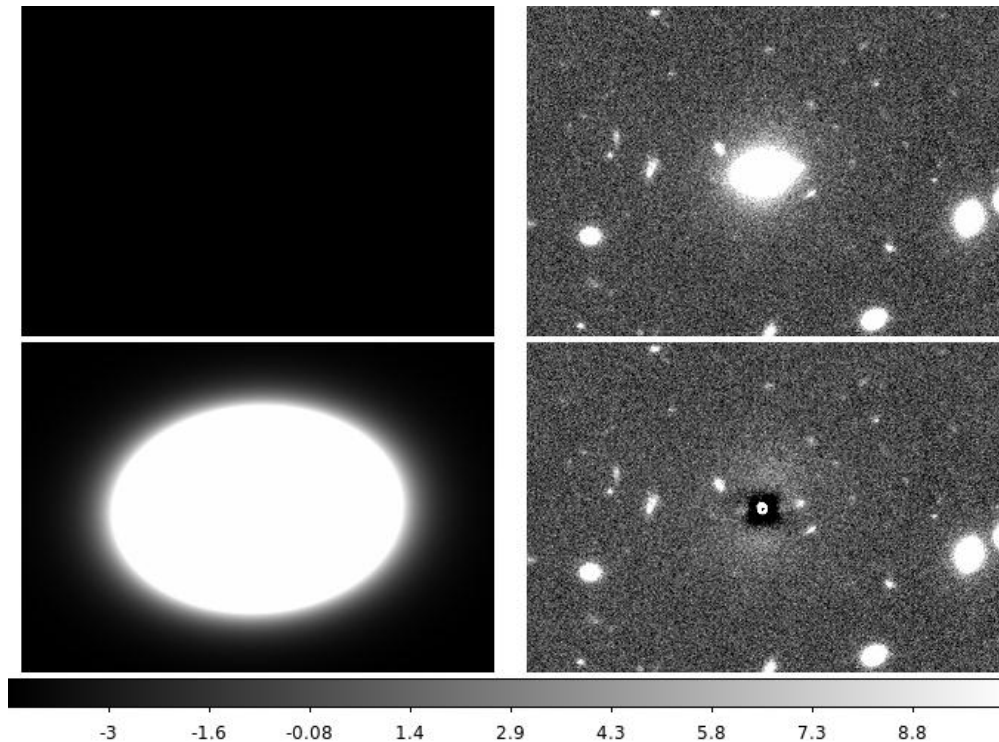


Figure 4.4. Example GALFIT output file for BCG 4634-r band; empty image (top left), original image (top right), the GALFIT model (bottom left) and the residual image (bottom right).

The result of the GALFIT run is a multi-extension FITS file that includes the cutout image, created model image, and residual image. Each individual frame is shown in Figure. 4.4. includes, as header data, the fitting process's output parameters. When the GALFIT run is finished, the programme collects the values, organises them, and put them in table in the output file that provides the fundamentals for the results.

A maximum of 100 iterations are permitted when using GALFIT in an iterative procedure. If the fitting procedure had already converged on a solution before the last iteration, we would know the values of the output of the fitting parameters. In the absence of such conditions, the wrapper software handles the empty values that are returned to mark these circumstances in the output file.

Creating a model for the BCG light distribution takes more consideration, for the reason that the enormous galaxy density in the core areas of galaxy clusters. As a result, in order to model the sky background accurately, for GALFIT, we developed a two-step run. We leave the components of the sky and Sersic free in the initial run. The sky value remains free, along the two axes of the image, as well as the sky gradients. We use the sky background and gradients and run GALFIT once again while holding the

settings constant after the first run has converged to a solution. The outcomes are the Sérsic parameters from the second run.

Having prepared the data and the initial parameters the fitting can be started in the following order;

- 1) Create the GALFIT input file by adding the name of the input data image, the output image name, the PSF image, and setting the starting values to the following parameters: image region, size of convolution, location of the target, effective radius (R_e), P.A., Sérsic index (n) and axis ratio (b/a).
- 2) Run GALFIT with the command `./galfit input.file`.
- 3) Check the model with DS9 visually.
- 4) Using the best fit values from the fit.log file, adjust the parameter values.

4.3. The Surface Brightness Profile Fitting of a Sample of BCGs

Our pipeline might converge on a solution for 2721 BCGs by following the steps described in the preceding section. We needed to delete nonphysical solutions from the findings before continuing with analysis. As a result, we used the coming standards for the GALFIT outputs; $\chi^2 < 5$, $n < 8$, and $R_e < 50$ kpc. Higher Sérsic indices are unreliable, thus we remove those greater than eight. Larger values for BCGs' effective radius over 50 kpc are also difficult to motivated physically, therefore we remove such examples as well.

The redshift range has received one final cut. In the scaling relations analysis, we did not include the few BCGs we had at lower ($z < 0.1$) and larger ($z > 1.0$) redshifts. Consequently, the redshift range that remain after this exclusion is $0.1 < z \leq 1.0$ for 2428 BCGs. Figure. 4.5. demonstrated the photometric redshifts and r-band magnitude distributions for the complete sample.

The sections below describe how the structural parameters analysed depending on the host cluster richness ($\lambda > 30$ and $\lambda \leq 30$) and the redshift of the BCG ($0.1 < z \leq 0.4$, $0.4 < z \leq 0.7$, and $0.7 < z \leq 1.0$). Table 4.1. shows the statistics of the structural parameters (i.e. R_e and n) for various redshift and richness redshift bins.

We offer relations for parameter pairs of the "photometric plane" (PP) of galaxies of the early type where Sérsic index takes the role of velocity dispersion. The PP links

$\log(R_e)$, μ_e , and $\log(n)$ to build an early-type galaxies three-dimensional reation (La Barbera et al., 2004).

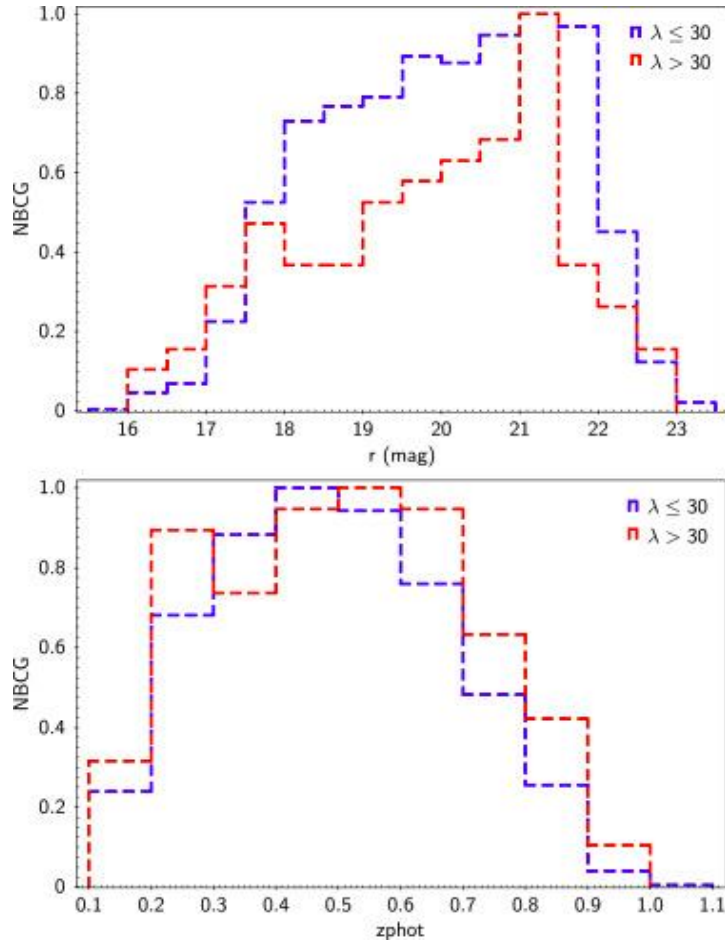


Figure 4.5. BCGs' r-band apparent magnitude normalised distributions (top) and photometric redshift (bottom). The whole sample for each histogram is divided into two subsamples for the lower richness ($\lambda \leq 30$) and higher richness ($\lambda > 30$) clusters.

Table 4.1. Statistical features of effective radius (R_e) (in kpc) and Sérsic index of the BCGs for different richness and redshift bins (number of objects, mean, standard deviation (σ) and median).

Effective radius (R_e) (kpc)												
		0.1 < z ≤ 0.4			0.4 < z ≤ 0.7			0.7 < z ≤ 1.0				
Richness	N	Mean	σ	Median	N	Mean	σ	Median	N	mean	σ	Median
$\lambda \leq 30$	535	13.074	8.4	10.8	803	13.7	9.3	10.9	231	11.3	7.6	9.08
$\lambda > 30$	37	15.399	7.5	13.9	55	17.0	10.6	12.7	22	14.9	10.5	11.9

Table 4.1. (Continued) Statistical features of effective radius (R_e) (in kpc) and Sérsic index of the BCGs for different richness and redshift bins (number of objects, mean, standard deviation (σ) and median).

		Sérsic Index (n)											
		0.1 < z \leq 0.4				0.4 < z \leq 0.7				0.7 < z \leq 1.0			
Richness	N	Mean	σ	Median	N	Mean	σ	Median	N	mean	σ	Median	
$\lambda \leq 30$	535	3.9	2.01	4.07	803	3.84	1.9	3.83	231	2.8	1.7	2.59	
$\lambda > 30$	37	4.4	1.4	4.49	55	3.5	1.9	3.94	22	2.5	1.2	2.55	

4.3.1. Distribution of structural parameters

Based on the host cluster richness, the structural characteristics of BCGs are compared in Figure. 4.6. It is clear that the rich clusters have an effective radius distribution that is skewed higher. This suggests that BCGs in more richer clusters appear to have a larger effective radius. The median values of effective radius shown in Table 4.1 illustrate that this tendency may be observed across all redshift bins. In the lowest redshift bin, the distinction between relatively rich and poor clusters becomes more obvious, which may be a sign of increased merging events in overcrowded surroundings. In contrast, both rich and poor clusters of BCGs exhibit a similar distribution of the Sérsic index.

There have been statistical studies run to see if BCGs from rich and poor clusters drawn from the same sample. Kolmogorov-Smirnov (KS) tests provide p-values as 0.8 for the Sérsic index, and the ANOVA tests give 0.7. One may conclude that these two samples cannot be easily distinguished from one another based on their Sérsic index. However, the effective radii in poor and rich clusters of BCGs are significantly different depending on their p-values of 6.6×10^{-4} for KS tests and 6.7×10^{-4} for ANOVA tests, respectively. According to Ascaso et al. (2011) findings, there are considerable relationships between the host cluster's X-ray luminosity and the BCG's absolute magnitude. The cluster's mass can be specified from the X-ray. In our study, the cluster richness is indicative of (Vikhlinin et al., 2006). Considering that BCGs demonstrate the same size-luminosity relation as other early-type galaxies (Samir et al., 2020; Ulgen et al., 2022), the effective radius obtained in the current study can be connected to the absolute magnitude of the BCGs.

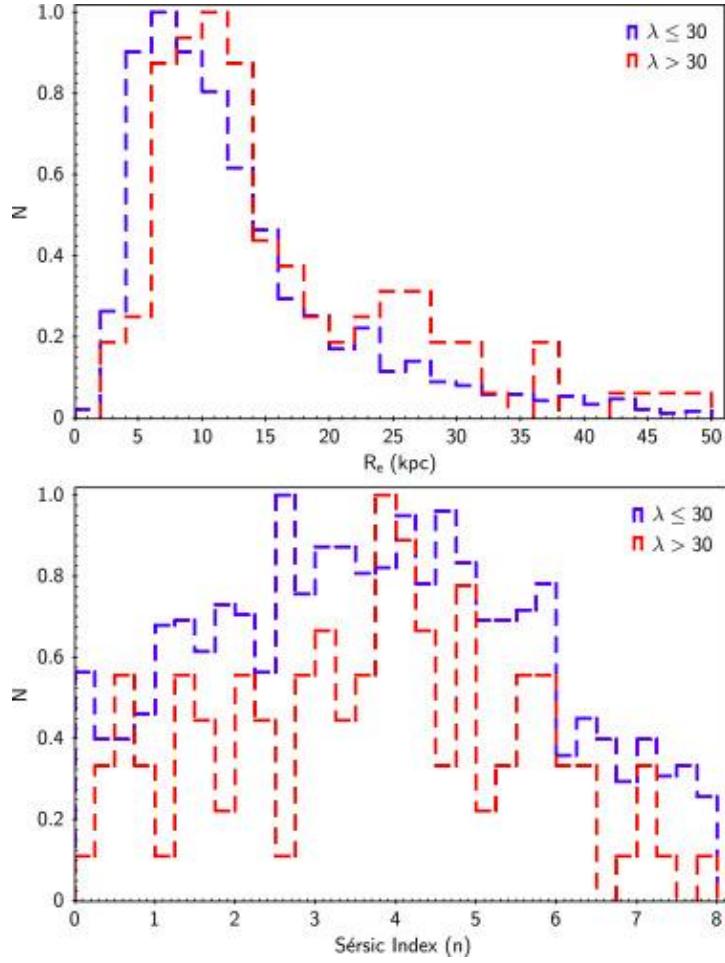


Figure 4.6. Normalised distributions effective radius (top) and Sérsic index (bottom) over the all-redshift range but for various richness cuts.

Figure 4.7. illustrates Sérsic index (n) and effective radius (R_e) relationship. The tendency with a large dispersion is that bigger BCGs which have higher Sérsic indices, as demonstrated by Chu et al. (2022). (Equation 4.1) presents the best-fit connection found from the entire sample.

$$\log (n) = (0.231 \log R_e) + 0.291 \quad (4.1)$$

$\log (R_e) - \log (n)$ relation has a consistent behaviour across every redshift bins, with slopes ranging from 0.2 – 0.3. Although, the BCG slopes are less steep in rich clusters. Table 4.2. provides the findings of particular redshift bins and for various richness of the host cluster. No matter the redshift or richness of our sample, the slope is consistent with the best-fit relations for BCG samples at $z \sim 0$ and $z \sim 0.5$ presented by Ascaso et al. (2011).

Table 4.2. parameters that best fit the relation between $\log(R_e) - \log(n)$ for different redshift and richness bins where a is the slope, and b is the intercept.

	All redshift		$0.1 < z \leq 0.4$		$0.4 < z \leq 0.7$		$0.7 < z \leq 1.0$	
	a	b	a	b	a	b	a	b
All richness	0.231	0.291	0.187	0.373	0.241	0.295	0.235	0.162
$\lambda \leq 30$	0.236	0.288	0.178	0.377	0.256	0.284	0.248	0.156
$\lambda > 30$	0.155	0.348	0.155	0.475	0.162	0.308	0.101	0.260

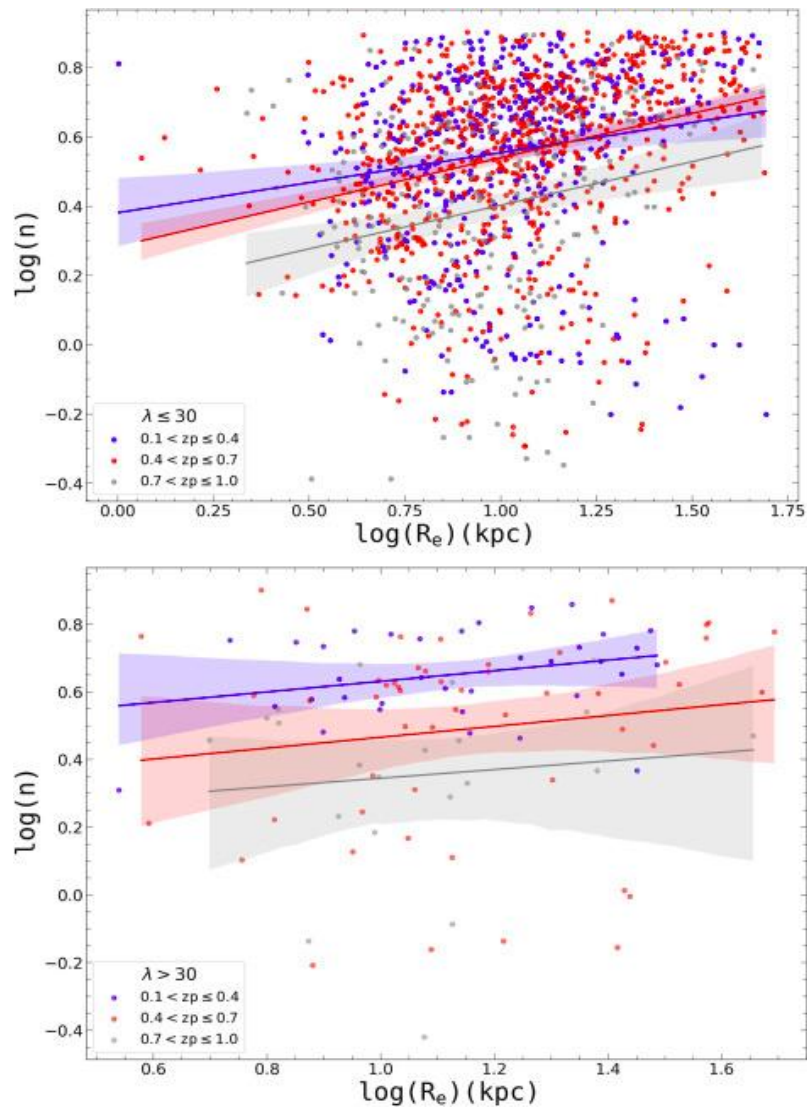


Figure 4.7. Relation between $\log R_e - \log n$ for poor (top) and rich (bottom) clusters. Blue, red, and gray points together with their corresponding linear fits (2σ) display various redshift bins. Confidence intervals are also shown for each fit.

4.4. The Kormendy Relation

The Kormendy relation relates an early-type galaxy's effective radius, within the same radius, to its mean surface brightness (Kormendy, 1977). The amount (μ_e) is a representation of the apparent magnitude of the corresponding total light that was seen within a square arc second at various locations within the distribution. The relation has the form of $\langle \mu_e \rangle = a \times \log(R_e) + b$, where the slope and intercept, respectively, are denoted by a and b . Thus, the Fundamental Plane (FP) of early-type galaxies is projected by the Kormendy relation (Dressler et al., 1987), It offers details on how galaxies' sizes have changed (Longhetti et al., 2007; Tortorelli et al., 2018) and indications of its formation (Kormendy et al., 2009).

The Kormendy relation (Kormendy, 1977) is a section of the Fundamental Plane. It presents the surface brightness dependence of the scale size of galaxies and for a de Vaucouleur surface brightness fit, is a plot of the surface brightness (μ_e) versus the effective radius (R_e). For normal elliptical galaxies because of their huge extended haloes, BCGs have been discovered to lie off the relation (Hoessel et al., 1987; Oegerle and Hoessel, 1991; Schombert, 1987). Another relation similar to that is the one between BCG size and luminosity. It appears to be steeper for BCGs than that of regular elliptical galaxies (Bernardi et al., 2007; Liu et al., 2008). However, it should be noted that using roughly the same data, some authors discover a substantially shallower slope (von der Linden et al., 2007). Figure. 4.8. illustrates the Kormendy relation which plotted for the samples of interest in both poor and rich clusters, at various redshift bins. The slope of this relation is parameterized and published. For instance, for Stott et al. (2011) sample the slope is $A = 20.3 \pm 0.9$ and $B = 2.7 \pm 0.8$, with the errors representing both the formal fit error as well as the relation's intrinsic scatter. This is quite consistent with the results by Brough et al. (2005) where $B = 2.60 \pm 0.03$. On the other hand, in other studies, The possibility of higher values of B , e.g., $B = 3.1 \pm 0.1$ found by both Hoessel et al. (1987) and Oegerle and Hoessel (1991) and $B = 3.44 \pm 0.13$ found by Bildfell et al. (2008).

The mean surface brightness inside the effective radius was calculated to derive the Kormendy relation as written in (Equation 4.2) by Graham and Driver (2005):

$$\mu_e = M_{tot} + 2.5 \log(2\pi R_e^2) + 2.5 \log \left(\frac{b}{a} \right) \quad (4.2)$$

where M_{tot} denotes the integrated magnitude, R_e implies the effective radius, and (b/a) is the axis ratio, where a is the semimajor axis and b is the semi minor axis.

Regardless of the richness and redshift bins, we find a Kormendy relation, as shown in (Equation 4.3). Table 4.3. lists the Kormendy relationship coefficients for various richness and redshift bins.

$$\mu_e = (3.941 \log R_e) + 18.955 \quad (4.3)$$

where (μ_e) is the mean surface brightness and R_e implies the effective radius.

Table 4.3. The best-fitting parameters for the relation between $\log(R_e) - \langle \mu_e \rangle$ (i.e., the Kormendy relation) for various redshift and richness bins, where a is the slope and b is the intercept.

	All redshift		0.1 < z ≤ 0.4		0.4 < z ≤ 0.7		0.7 < z ≤ 1.0	
	<i>a</i>	<i>b</i>	<i>a</i>	<i>b</i>	<i>a</i>	<i>b</i>	<i>a</i>	<i>b</i>
All richness	3.941	18.955	4.005	17.933	4.062	19.141	3.863	20.222
$\lambda \leq 30$	3.958	18.940	4.035	17.907	4.075	19.135	3.972	20.122
$\lambda > 30$	3.546	19.381	3.000	18.951	4.055	19.089	3.203	20.822

Basically, Because of the variable nature and surroundings of the sample, the Kormendy relation highlights the quantitative variation in surface brightness at specified effective radius (Samir et al., 2020). Generally, it shows that BCGs remain in the luminous family (Caon et al., 1994; Capaccioli et al., 1992). For the sample, we were able to derive a Kormendy relation having a much steeper slope.

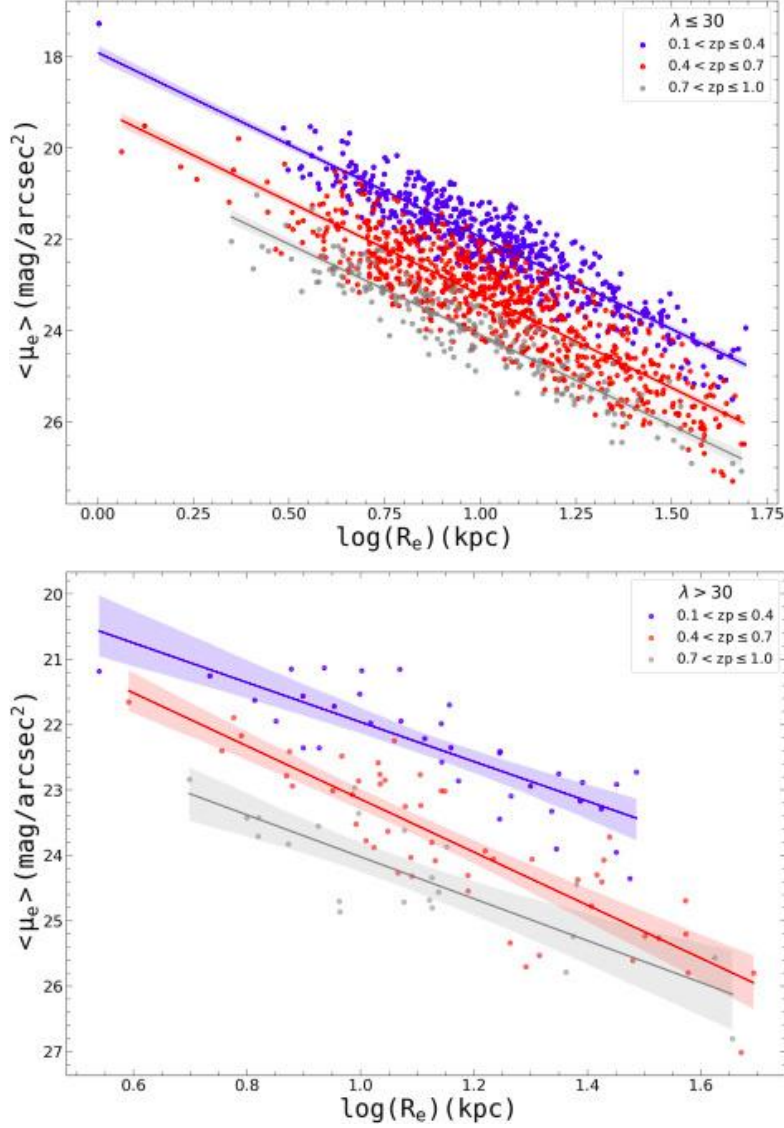


Figure 4.8. The Kormendy relation for poor (top) and rich (bottom) clusters, the meaning of points, lines, and shaded regions is the same as Figure 4.7.

4.5. Size-Luminosity Relation

The correlation between the absolute magnitude and the effective radius have been shown in Figure 4.9. In all redshift bins, the link between the absolute magnitude in r-band (M_r) and the effective radius appears to be highly consistent. The findings of the linear fits are shown in Figure 4.9.

For the whole sample, we determine the size-luminosity relation provided in (Equation 4.4) below:

$$\text{Log}(R_e) = -0.240 M_r - 4.481 \quad (4.4)$$

Where R_e is the effective radius and M_r the absolute magnitude in r-band.

In Table 4.4. coefficients for the best-fitting bins are presented. Both rich and poor clusters have a little bit higher slope of the size-luminosity relation in the highest redshift bin. Although, there isn't much of a difference in the redshift bins' slopes.

This size–luminosity relation, for early-type galaxies, has also been supported by Aguerri et al. (2005); Bernardi (2009); Caon et al. (1993); Gutiérrez and Azzaro (2004). According to Samir et al. (2020) that BCGs have a steeper size-luminosity relation than isolated galaxies. This steepening is caused by the high luminosities of BCGs as well as their environment.

There is a considerable relationship between the absolute magnitude and the shape parameter, as well as the absolute magnitude and the effective surface brightness, exists for BCGs at low redshift. Although, for the intermediate-redshift sample, these patterns are less significant (Ascaso et al., 2011).

BCG sizes and luminosities have a linear relationship which also demonstrated by Samir et al. (2020) using a sample they took from the SDSS. Our magnitudes are converted to luminosities in order to produce $(\log L_r - \log R_e)$ that is equivalent to absolute magnitudes, even if we prefer to provide absolute magnitudes. It is difficult to distinguish between BCGs of poor clusters and rich clusters for this comparison since their results were not presented in a manner similar to our study's. Our best-fit linear relation has a slope of $a = 0.33 \pm 0.02$ for the whole dataset, but Samir et al. (2020) observed a slope of $a = 0.72 \pm 0.02$. The two studies' various redshift ranges might be the cause of the slope's discrepancy.

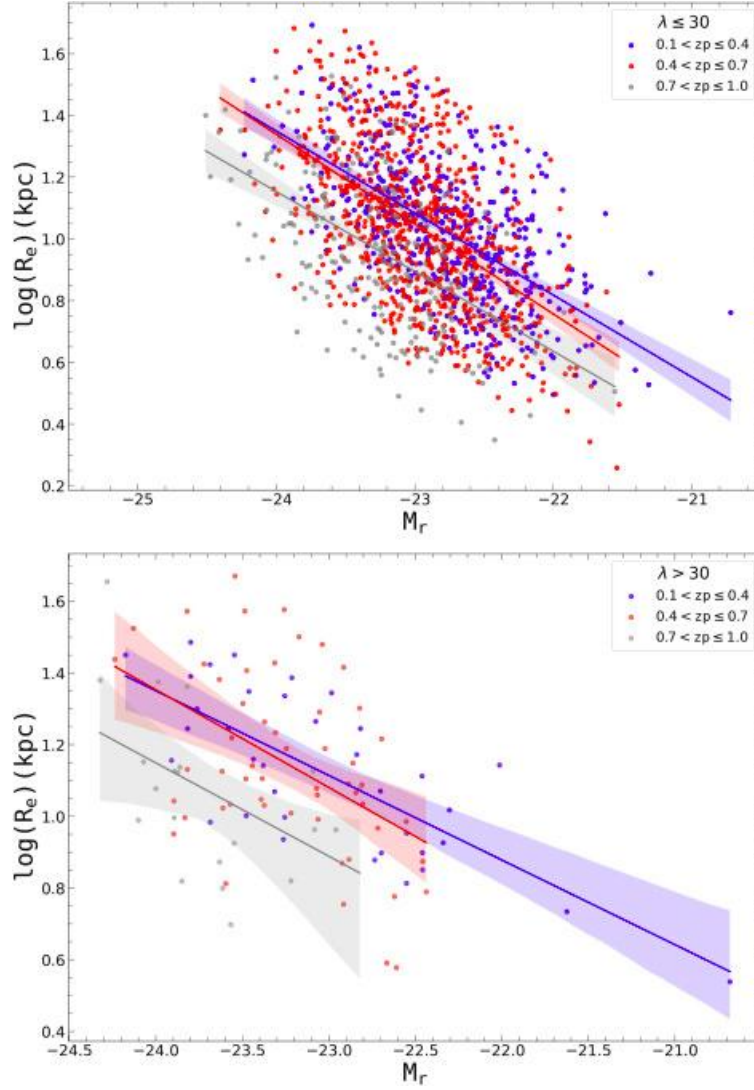


Figure 4.9. The size-luminosity relation for poor (top) and rich (bottom) clusters. The meaning of points, lines, and shaded regions is the same as in Figure 4.7.

Table 4.4. The size-luminosity relation's best-fit parameters for various redshift and richness bins, where a is the slope and b is the intercept.

	All redshift		0.1 < z ≤ 0.4		0.4 < z ≤ 0.7		0.7 < z ≤ 1.0	
	a	b	a	b	a	b	a	b
All richness	-0.240	-4.481	-0.263	-4.961	-0.290	-5.629	-0.256	-4.990
$\lambda \leq 30$	-0.242	-4.519	-0.265	-5.022	-0.290	-5.63	-0.259	-5.060
$\lambda > 30$	-0.196	-3.422	-0.236	-4.311	-0.274	-5.213	-0.261	-5.110

4.6. Evolution of Structural Parameters

Figure 4.10 shows the relation between the BCGs' effective radius and Sérsic index as functions of the redshift. We display BCGs in different clusters for poor cluster ($\lambda \leq 30$) and rich cluster ($\lambda > 30$) in both panels. To more clearly display the patterns, according to the centre redshifts of the bins used in this study, the median values for each were presented, which are 0.25, 0.55, and 0.75.

The Sérsic index has a little rise in the direction of less redshifts. Though, our effective radius measurements did not indicate any considerable redshift-related evolution. Figure 4.10. illustrates how the trends in the parameters for poor clusters and rich clusters are consistent. The mean distinction between the median Sérsic index values for poor clusters and rich clusters is $\langle \Delta n \rangle = 0.19$. In a similar way, the mean distinction of the effective radius $\langle \Delta \log (R_e) \rangle = 0.10$. These results imply that the BCG structural parameters have evolved similarly in both the poor clusters and rich clusters.

Similar trends for the effective radius are shown in the latest research by Chu et al. (2022), which suggests that the BCG sizes have not changed since $z = 0.7$. Stott et al. (2011) investigated some high redshift data of BCGs (i.e., $0.8 < z < 1.3$), that HST imaging is accessible, use a nearby sample of BCGs at $z \sim 0.25$, they similarly discovered minimal change in size.

In contrast to Ascaso et al. (2011), our findings found that the effective radius evolution differs from the Sersic index. Low- and intermediate-redshift samples of them have comparable Sersic indices, however their low redshift BCGs are about twice as big as those at intermediate redshifts. Even after our sample was divided into rich and poor groups, we still did not observe a comparable size evolution in our analysis. Though, in rich clusters, our BCGs had larger effective radii compared to those in poor clusters. Bai et al. (2014) demonstrated that a relation between the stellar masses of BCGs and cluster richness and noted that the mass of BCGs rises by around 1.5 times from $z = 0.5$ to $z = 0$. We are unable to directly compare due to the fact that the lack of stellar masses for our sample of BCGs. However, In the same redshift range, it is hard to notice a rise in BCG sizes, which might be used as a measure of star mass.

Our findings are compared to the literature in Table 4.5. It can be observed that our results match well with those from previous research in comparable redshift ranges. A good study of nearby BCGs ($z \leq 0.08$) by Kluge et al. (2020) demonstrated a

comparable slope for the for the Kormendy relation as 3.61 ± 0.13 . Chu et al. (2022) investigated, from the CFHTLS, BCGs as well, but they included all Wide fields, in contrast, we utilised a cluster catalogue produced from the W1. Cross-matching the galaxies was not possible since the BCG catalogue for Chu et al. (2022) had not been available when this paper was submitted. However, we might predict little fraction of overlap among the clusters, thus to BCGs. Considering that overlap, it appears that both studies' findings are very compatible in terms of the Kormendy relation's slope and intercept. We must note that despite Chu et al. (2022) 's analysis included all the CFHTLS-Wide imaging, that covers around 155 deg^2 , we have a nearly two-times larger BCG sample than they have.

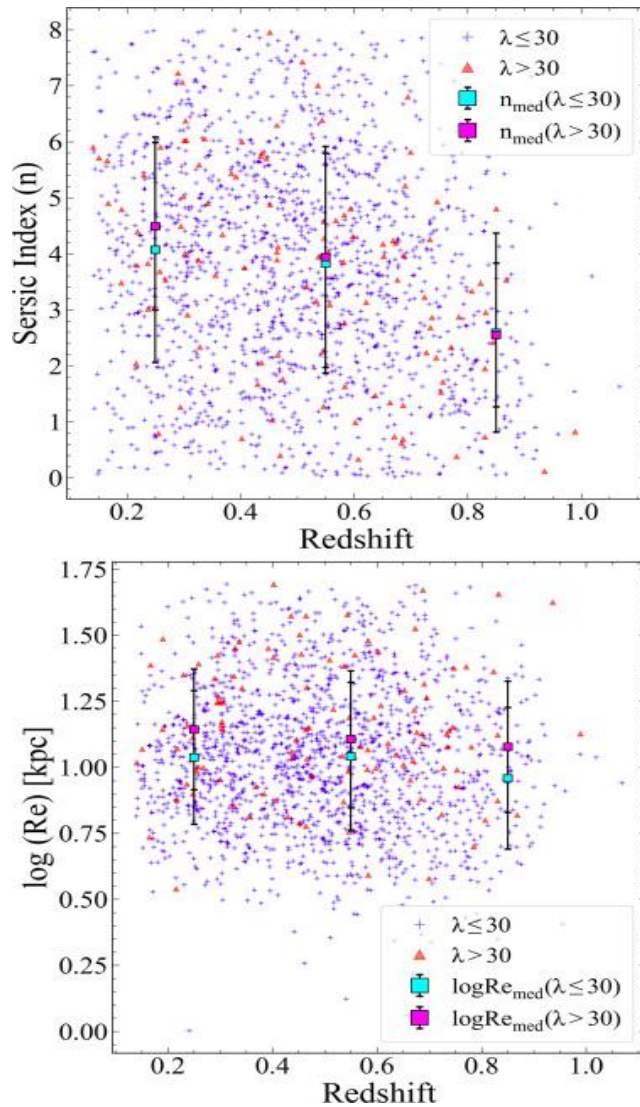


Figure 4.10. Evolution of the Sérsic index (top) and effective radius (bottom) for poor and rich clusters. BCGs in poor and rich clusters are shown, respectively, by blue and red dots. For both poor and rich clusters, the median values for each redshift bin are displayed individually.

Table 4.5. The Kormendy relation coefficients gathered in our work are compared with those from earlier studies on various redshift scales. The relation's slope is represented by a , and its intercept by b .

Redshift range	This study		Redshift range	previous studies		Reference
	a	b		a	b	
0.1 < z \leq 0.4	4.005	18.955	0.076 < z < 0.394	3.75	16.40	Samir <i>et al.</i> (2020)
			0.15 < z < 0.55	3.44	-	Bildfell <i>et al.</i> (2008)
0.4 < z \leq 0.7	4.062	19.141	0.3 < z < 0.6	3.346	18.33	Ascaso <i>et al.</i> (2011)
0.7 < z \leq 1.0	3.863	20.222	0.8 < z < 1.3	2.7	20.3	Stott <i>et al.</i> (2011)
0.1 < z \leq 1.0	3.941	18.955	0.3 < z < 0.9	3.50	18.01	Bai <i>et al.</i> (2014)
0.1 < z \leq 1.0	3.941	18.955	0.187 < z < 1.8	3.33	-	Chu <i>et al.</i> (2021)
			0.1 < z < 0.7	3.34	18.65	Chu <i>et al.</i> (2022)

5. CONCLUSIONS

A structural study of a BCG sample with a $0.1 < z \leq 1.0$ redshift range is presented. The most extensive sample ever applied for this sort of research is this one. The first catalogue of galaxy clusters, the CFHTLS-W1 contains 3283 clusters which we use. Although, following the fitting technique for the surface brightness profile, we preserve 1685 galaxies' reliable information, just as mentioned in results in the pervious chapter. We applied the r-band images produced within the CFHTLS framework in the field of 72 deg^2 for the procedure. Using GALFIT, a surface brightness profile fitting tool, we were able to extract effective radii and Sérsic indices, which represent the structural characteristics of BCGs.

Depending on the host cluster's richness, the cluster sample have been divided into two sub-samples, in order to determine any possible environmental effects. How effective radii are distributed shown in Figure 4.6 suggests that the environmental influences on the evolution of the BCG can vary. Cannibalism and galaxy mergers may occur more often in richer clusters since BCGs are located in the galaxy clusters' potential well's core. The connection between the host cluster properties and the BCG structural parameters for a sample at $z \sim 0$ was also demonstrated by Ascaso et al. (2011). The Sérsic index distributions for different richness are nearly identical as the K-S test predicts.

For any evolutionary impact to be observed, our BCGs were binned into three various redshift bins (i.e., $0.1 < z \leq 0.4$, $0.4 < z \leq 0.7$ and, $0.7 < z \leq 1.0$). The cosmic dimming is primarily responsible for the offsets in the Kormendy relation at various redshift bins. In addition to the offsets, individual relationship slopes are consistent with one another. A general acceptance appears for the relevant redshift range of the results of our study in Table 4.5. when comparing our results with those of earlier studies.

With the exception of both poor and rich clusters, the highest redshift bin, a relatively similar trends were observed, in the link between size and luminosity, across all redshift ranges. However, it is important to note that rich clusters have fewer BCGs, therefore in the highest redshift bin.

Other studies have similarly noted the BCG sizes' little or absent evolution since $z \sim 1$ (Chu et al., 2021, 2022; Stott et al., 2011). Additional study is necessary because certain observational studies revealed a rise in the size (Ascaso et al., 2011; Bai et al., 2014; Bernardi, 2009; Lavoie et al., 2016; Lidman et al., 2013). That is like some theoretical studies (De Lucia and Blaizot, 2007; Naab et al., 2009; Ruzkowski and Springel, 2009). Images from high-resolution of BCGs at various epochs might give vital insights into this debate.

Some of the light coming from the outer borders of the BCG may have been reduced by the reduction of the background of CFHTLS images, as was mentioned in Section 3.1. Consequently, the results could be interpreted with care for smaller redshifts (i.e. $z < 0.3$), at low redshifts, investigating the development of BCG's size may benefit from the independent reduction of the survey's raw images.

REFERENCES

- [1] Agüena, M., Benoist, C., da Costa, L.N., Ogando, R.L.C., Gschwend, J., Sampaio Santos, H.B., Lima, M., Maia, M.A.G., Allam, S., Avila, S., Bacon, D., Bertin, E., Bhargava, S., Brooks, D., Carnero Rosell, A., Carrasco Kind, M., Carretero, J., Costanzi, M.,..... Wilkinson, R.D. (2021). The WaZP galaxy cluster sample of the dark energy survey year 1. *Mon. Not. R. Astron. Soc.*, 502 (3), 4435–4456. <http://dx.doi.org/10.1093/mnras/stab264>, arXiv:2008.08711
- [2] Aguerri, J.A.L., Elias-Rosa, N., Corsini, E.M., Muñoz-Tuñón, C. (2005). Photometric properties and origin of bulges in SB0 galaxies. *Astron. Astrophys.*, 434, 109–122. DOI: 10.1051/0004-6361:20041743
- [3] Alis S. (2009). Evolutionary Effects on Brightest Cluster Galaxy (BCG) Detections in the CFHTLS-Deep Fields. *Publications de l’Observatoire Astronomique de Beograd*, 86,309. <https://ui.adsabs.harvard.edu/abs/2009POBeo..86..309A>
- [4] Aragón-Salamanca, A., Ellis, R.S., Couch, W. J., Carter, D. (1993). Evidence for systematic evolution in the properties of galaxies in distant clusters, *Mon. Not. R. Astron. Soc.*, 262 (3), 764–794, <https://doi.org/10.1093/mnras/262.3.764>.
- [5] Aragon-Salamanca, A., Baugh, C.M., Kauffmann, G. (1998). The K-band Hubble diagram for the brightest cluster galaxies: a test of hierarchical galaxy formation models. *Mon. Not. R. Astron. Soc.*, 297 (2), 427–434. <http://dx.doi.org/10.1046/j.1365-8711.1998.01495.x>, arXiv:astro-ph/9801277
- [6] Ascaso, B., Aguerri, J.A.L., Varela, J., Cava, A., Bettoni, D., Moles, M., D’Onofrio, M. (2011). Evolution of Brightest Cluster Galaxy Structural Parameters in the Last 6 Gyr: Feedback Processes Versus Merger Events. *Astrophys. J.*, 726 (2), 69. <http://dx.doi.org/10.1088/0004-637X/726/2/69>, arXiv:1007.3264
- [7] Bai, L., Yee, H.K.C., Yan, R., Lee, E., Gilbank, D.G., Ellingson, E., Barrientos, L.F., Gladders, M.D., Hsieh, B.C., Li, I.H. (2014). The Inside-out Growth of the Most Massive Galaxies at $0.3 < z < 0.9$. *Astrophys. J.*, 789 (2), 134. <http://dx.doi.org/10.1088/0004-637X/789/2/134>, arXiv:1406.4149.
- [8] Baldry, I. K., Balogh, M. L., Bower, R. G., Glazebrook, K., Nichol, R. C., Bamford, S. P., Budavari T. (2006). Galaxy bimodality versus stellar mass and environment. *Mon. Not. R. Astron. Soc.*, 373, 469–483
- [9] Bamford, S.,P., Nichol, R.,C., Baldry, I.,K., Land, K., Lintott, C.,J., Schawinski, K., Slosar, A., Szalay, A. S., Thomas, D., Torke, M., Andreescu, D., Edmondson, E.M., Miller, C.J, Murray, P., Raddick, M.J., Vandenberg, J. (2009). Galaxy Zoo: the dependence of morphology and colour on environment. *Mon. Not. R. Astron. Soc.*, 393, 1324. doi:10.1111/j.1365-2966.2008.14252

- [10] Bautz, L. P., and Morgan, W. W. (1970). On the classification of the forms of clusters of galaxies, *Astrophys. J.*, 162, L149-L153. doi:10.1086/180643
- [11] Beck, S. C. (2000). Dwarf galaxies & starbursts. *Sci Am.*, 282(6), 66-71. doi: 10.1038/scientificamerican0600-66. PMID: 10862425.
- [12] Beers, T.C., and Geller, M.J. (1983). The environment of D and cD galaxies. *Astrophys. J.*, 274, 491-501. doi:10.1086/161463
- [13] Bekki, K., Couch, W.J., Drinkwater, M. J., Gregg, M.D. (2001), *Astrophys. J.*, 557, L39-L42. <https://iopscience.iop.org/article/10.1086/323075/fulltext/015435.text.html>
- [14] Bellstedt, S., Lidman, C., Muzzin, A., Franx, M., Guatelli, S., Hill, A.R., Hoekstra, H., Kurinsky, N., Labbe, I., Marchesini, D., Marsan, Z.C., Safavi-Naeini, M., Sifón, C., Stefanon, M., van de Sande, J., van Dokkum, P., Weigel, C. (2016). The evolution in the stellar mass of brightest cluster galaxies over the past 10 billion years. *Mon. Not. R. Astron. Soc.*, 460 (3), 2862–2874. <http://dx.doi.org/10.1093/mnras/stw1184>, arXiv:1605.02736
- [15] Benjamin, J., Heymans, C., Semboloni, E., Waerbeke, L.V., Hoekstra, H., Erben, T., Gladders, M.D., Hettterscheidt, M., Mellier, Y., Yee, H.K.C. (2007). Cosmological constraints from the 100-deg² weak-lensing survey *Mon. Not. R. Astron. Soc.*, 381, 702–712 doi:10.1111/j.1365-2966.2007.12202
- [16] Bernardi, M., Hyde, J.B., Sheth, R.K., Miller, C.J., Nichol, R.C. (2007). The Luminosities, Sizes, and Velocity Dispersions of Brightest Cluster Galaxies: Implications for Formation History. *Astron. J.*, 133 (4), 1741–1755. <http://dx.doi.org/10.1086/511783>, arXiv:astro-ph/0607117.
- [17] Bernardi, M. (2009). Evolution in the structural properties of early-type brightest cluster galaxies at small lookback time and dependence on the environment. *Mon. Not. R. Astron. Soc.*, 395 (3), 1491–1506. <http://dx.doi.org/10.1111/j.1365-2966.2009.14601.x>, arXiv:0901.1318.
- [18] Bertin, E. (2012). Displaying Digital Deep Sky Images. In: Ballester, P., Egret, D., Lorente, N.P.F. (Eds.), *Astronomical Data Analysis Software and Systems XXI*. In: *Astronomical Society of the Pacific Conference Series*. 461, 263.
- [19] Bertola, F. (1981). What Shape are Elliptical Galaxies? *S&T*, 61, 380. <https://ui.adsabs.harvard.edu/abs/1981S&T....61..380B>
- [20] Bevington, P. R. and Keith, R.D. (2003). *Data reduction and error analysis for the physical sciences.* (3rd ed). McGraw-Hill. <https://ui.adsabs.harvard.edu/abs/2003drea.book.....B>
- [21] Bildfell, C., Hoekstra, H., Babul, A., Mahdavi, A. (2008). Resurrecting the red from the dead: optical properties of BCGs in X-ray luminous clusters. *Mon. Not. R. Astron. Soc.*, 389 (4), 1637–1654. <http://dx.doi.org/10.1111/j.1365-2966.2008.13699.x>, arXiv:0802.2712
- [22] Binney, J., and Tremaine, S. (1987). *Galactic dynamics.* (2nd ed). Princeton Series in Astrophysics. <https://ui.adsabs.harvard.edu/abs/1987gady.book.....B>
- [23] Blanton, M. R., Hogg, D. W., Bahcall, N. A., Brinkmann, J., Britton, M., Connolly, A. J., Csabai, I., Fukugita, M., Loveday, J., Meiksin, A., Munn, J.

- A., Nichol, R. C., Okamura, S., Quinn, T., Schneider, D. P., Shimasaku, K., Strauss, M. A., Tegmark, M, Vogeley, M. S., Weinberg, D. H. (2003). *Astrophys. J.*, 592, 819-838. doi:10.1086/375776
- [24] Blanton, M. R. and Moustakas, J. (2009). Physical properties and environments of nearby galaxies. *Ann. Rev. Astro. Astroph.*, 47, 159-210. <https://doi.org/10.1146/annurev-astro-082708-101734>
- [25] Block, D. L. (2001). The Duality of Spiral Structure, *S&T*, 101(1), 48. <https://ui.adsabs.harvard.edu/abs/2001S&T...101a..48B>
- [26] Bothun, G. D. (2000). Beyond the Hubble Sequence, *S&T*, 99 (5), 36. <https://ui.adsabs.harvard.edu/abs/2000S&T...99e..36B>
- [27] Boulade, O., Charlot, X., Abbon, P., Aune, S., Borgeaud, P., Carton, P., Carty, M., Desforge, D., Eppele, D., Gallais, P., Gosset, L., Granelli, R., Gros, M., de Kat, J., Loiseau, D., Mellier, Y., Ritou, J. L., Rousse, J. Y., Starzynski, P., ..., Vigroux, L. G. (2000). Development of MegaCam, the next-generation wide-field imaging camera for the 3.6-m Canada-France-Hawaii Telescope. *Proc. SPIE, Optical and IR Telescope Instrumentation and Detectors*, 4008, 657-668. doi: 10.1117/12.395524
- [28] Bower, R. G., Lucey, J. R., and Ellis, R. S. (1992), Precision photometry of early-type galaxies in the Coma and Virgo clusters: a test of the universality of the colour–magnitude relation – I. The data. *Mon. Not. R. Astron. Soc.*, 254, 589 <https://doi.org/10.1093/mnras/254.4.589>
- [29] Brough, S., Collins, C. A., Burke, D. J., Mann, R. G., & Lynam, P. D. (2002). Evolution of brightest cluster galaxies in X-ray clusters. *Mon. Not. R. Astron. Soc.*, 329, L53-L56 doi: 10.1046/j.1365-8711.2002.05179.x
- [30] Brough, S., Collins, C.A., Burke, D.J., Lynam, P.D., Mann, R.G. (2005). Environmental dependence of the structure of brightest cluster galaxies. *Mon. Not. R. Astron. Soc.*, 364 (4), 1354–1362. <http://dx.doi.org/10.1111/j.1365-2966.2005.09679.x>, arXiv: astro-ph/0510065.
- [31] Brough, S., Couch, W.J., Collins, C.A., Jarrett, T., Burke, D.J., Mann, R.G. (2008). The luminosity halo mass relation for brightest cluster galaxies. *Mon. Not. R. Astron. Soc.*, 385 (1), L103–L107. <http://dx.doi.org/10.1111/j.1745-3933.2008.00442.x>, arXiv:0801.1170.
- [32] Brough, S., Tran, K.-V., Sharp, R. G., von der Linden, A., & Couch, W. J. (2011). Spatial kinematics of Brightest Cluster Galaxies and their close companions from Integral Field Unit spectroscopy. *Mon. Not. R. Astron. Soc.*, 414(1), L80-L84. doi: 10.1111/j.1745-3933.2011.01060.x
- [33] Budding, E. and Demircan, O. (2007). Introduction to Astronomical Photometry. ed. R. Ellis, J. Huchra, S. Kahn, G. Rieke, & P. B. Stetson (2nd ed). Cambridge: Cambridge University Press <https://ui.adsabs.harvard.edu/abs/2007iap..book....B>
- [34] Burke C., Collins C. A. (2013). Growth of brightest cluster galaxies via mergers since $z=1$. *Mon. Not. R. Astron. Soc.*, 434, 2856. <https://doi.org/10.1093/mnras/stt1192>

- [35] Burstein, D. (1979). Structure and origin of S0 galaxies. III. The luminosity distribution perpendicular to the plane of the disks in S0's. *Astrophys J.*, 234, 829-836. doi: 10.1086/157563
- [36] Caon, N., Capaccioli, M., and D'Onofrio, M. (1993). On the shape of the light profiles of early-type galaxies. *Mon. Not. R. Astron. Soc.* 265(4), 1013–1021 <https://doi.org/10.1093/mnras/265.4.1013>
- [37] Caon, N., Capaccioli, M., D'Onofrio, M. (1994). VizieR Online Data Catalog: B-band photometry in Fornax and Virgo. *VizieR Online Data Catalog*. doi:1994yCat..41060199C
- [38] Capaccioli, M. (1989). Photometry of early-type galaxies and the $r^{1/4}$ law. In: Corwin, H.G., Bottinelli, L. (eds). *The World of Galaxies*. Springer, New York, NY. https://doi.org/10.1007/978-1-4613-9356-6_29
- [39] Capaccioli, M., Caon, N., and D'Onofrio, M. (1992). Families of galaxies in the μ_e - R_e plane. *Mon. Not. R. Astron. Soc.*, 259(2), 323-327. doi:10.1093/mnras/259.2.323
- [40] Carnevali, P., Cavaliere, A., and Santangelo, P. (1981). Merging instability in groups of galaxies. *Astrophys J.*, 249, 449-461. doi: 10.1086/159305
- [41] Carter, D., and Metcalfe, N. (1980). The morphology of clusters of galaxies. *Mon. Not. R. Astron. Soc.*, 191, 325-337. doi: 10.1093/mnras/191.2.325
- [42] Castignani, G., Benoist, C. (2016). A new method to assign galaxy cluster membership using photometric redshifts. *Astron. Astrophys.* 595, A111. <http://dx.doi.org/10.1051/00046361/201528009>, arXiv:1606.08744
- [43] Chu, A., Durret, F., Márquez, I. (2021). Physical properties of brightest cluster galaxies up to redshift 1.80 based on HST data. *Astron. Astrophys.* 649, A42. <http://dx.doi.org/10.1051/00046361/202040245>, arXiv:2102.01557.
- [44] Chu, A., Sarron, F., Durret, F., Márquez, I. (2022). Physical properties of more than one thousand brightest cluster galaxies detected in the Canada-France-Hawaii Telescope Legacy Survey. *Astron. Astrophys.* 666, A54. <http://dx.doi.org/10.1051/0004-6361/202243504>, arXiv:2206.14209.
- [45] Collins, C. A., Stott, J. P., Hilton, M., Kay, S.T., Stanford, S. A., Davidson, M., Hosmer, M., Hoyle, B., Liddle, A., Lloyd-Davies, E., Mann, R.G., Mehrrens, N., Miller, C. J., Nichol, R. C., Romer, A. K., Sahlén, M., Viana, P. T. P., West, M. J. (2009). Early assembly of the most massive galaxies, *Nature*, 458, 603-606. doi: 10.1038/nature07865
- [46] Conroy, C., Wechsler, R. H., and Kravtsov, A. V. (2007). The Hierarchical Build-Up of Massive Galaxies and the Intracluster Light since $z = 1$. *Astrophys J.* 668, 826-838. doi: 10.1086/521425
- [47] Conselice, C. J., Bershady, M. A., and Jangren, A. (2000). The Asymmetry of Galaxies: Physical Morphology for Nearby and High-Redshift Galaxies. *Astrophys. J.* 529 (2), 886–910. doi:10.1086/308300
- [48] Conselice, C. J. (2003). The Relationship between Stellar Light Distributions of Galaxies and Their Formation Histories. *Astrophys. J. S.*, 147, 1–28. doi: 10.1086/375001

- [49] Conselice, C. J. (2014). The evolution of galaxy structure over cosmic time, *Annu. Rev. Astron. Astrophys.*, 52, 291–337. doi: 10.1146/annurev-astro-081913-040037
- [50] Conselice, C. J., Bluck, A.F.L., Buitrago, F., Bauer A.E., Grützbauch, R., Bouwens, R.J., Bevan, S., Mortlock, A., M. Dickinson, M., Daddi, E., Yan, H., Scott, D., Chapman, S.C., Chary, R.R., Ferguson, H.C., Giavalisco, M., Grogin, N., Illingworth, G., Jogee, S., Weinzierl, T. (2011). The Hubble Space Telescope GOODS NICMOS Survey: overview and the evolution of massive galaxies at $1.5 < z < 3$. *Mon. Not. R. Astron. Soc.*, 413, 80-100 <https://doi.org/10.1111/j.1365-2966.2010.18113.x>
- [51] Cowie, L.L., and Binney, J. (1977). Radiative regulation of gas flow within clusters of galaxies: a model for cluster X-ray sources. *Astrophys J.* 215, 723-732 doi:10.1086/155406
- [52] De Lucia, G., Blaizot, J. (2007). The hierarchical formation of the brightest cluster galaxies. *Mon. Not. R. Astron. Soc.*, 375 (1), 2–14. <http://dx.doi.org/10.1111/j.1365-2966.2006.11287.x>, arXiv:astro-ph/0606519.
- [53] De Propris, P., West, M. W, Andrade-Santos, F., Ragone-Figueroa, C., Elena Rasia, E., Forman, W., Jones, C., Kipper, R., Borgani, S., Lambas, D.G., Romashkova, E.A., Patra, K.C. (2020). Brightest cluster galaxies: the centre can(not?) hold. *Mon. Not. R. Astron. Soc.*, 500, 310-318. doi:10.1093/mnras/staa3286.
- [54] de Souza, R. E., Gadotti, D. A., and dos Anjos, S. (2004). BUDDA: A new two-dimensional bulge/disk decomposition code for detailed structure analysis of galaxies. *Astrophys. J., Suppl. Ser.*, 153, 411
- [55] de Vaucouleurs G. (1948). Recherches sur les Nebuleuses Extragalactiques, *Ann. d'Astrophys.*, 11, 247
- [56] de Vaucouleurs G., de Vaucouleurs A., Corwin H. G., Jr, Buta R. J., Paturel G., Fouque P. (1991). Third Reference Catalogue of Bright Galaxies. Volume I: Explanations and references. Volume II: Data for galaxies between 0h and 12h. Volume III: Data for galaxies between 12h and 24h, Springer-Verlag: New York.
- [57] Dressler, A. (1980). Galaxy morphology in rich clusters: implications for the formation and evolution of galaxies. *Astrophys. J.* 236, 351-365. doi:10.1086/157753
- [58] Dressler, A. (1984). Internal kinematics of galaxies in clusters. I. Velocity dispersions for elliptical galaxies in Coma and Virgo. *Astrophys. J.*, 281, 512–524. <http://dx.doi.org/10.1086/162124>.
- [59] Dressler, A., Lynden-Bell, D., Burstein, D., Davies, R.L., Faber, S.M., Terlevich, R., Wegner, G. (1987). Spectroscopy and Photometry of Elliptical Galaxies. I. New Distance Estimator. *Astrophys. J.*, 313, 42. <http://dx.doi.org/10.1086/164947>.
- [60] Dressler, A., Oemler, A., J., Butcher, H. R., Gunn, J. E. (1994). The Morphology of Distant Cluster Galaxies. I. HST Observations of CL 0939+4713. *Astrophys. J.*, 430, 107. doi: 10.1086/174386

- [61] Dubinski, J., (1998). The Origin of the Brightest Cluster Galaxies. *Astrophys. J.*, 502 (1), 141–149. <http://dx.doi.org/10.1086/305901>, arXiv:astro-ph/9709102.
- [62] Edwards L. O. V., and Patton D. R., (2012). Close companions to brightest cluster galaxies: support for minor mergers and downsizing. *Mon. Not. R. Astron. Soc.*, 425, 287-295. doi:10.1111/j.1365-2966.2012.21457.x
- [63] Fabian, A.C., and Nulsen, P.E.J. (1977). Subsonic accretion of cooling gas in clusters of galaxies. *Mon. Not. R. Astron. Soc.*, 180, 479 -484. doi:10.1093/mnras/180.3.479
- [64] Fabian, A. C., Nulsen, P. E. J., and Canizares, C. R. (1982). Star formation in a cooling flow. *Mon. Not. R. Astron. Soc.*, 201, 933. doi:10.1093/mnras/201.4.933
- [65] Fasano, G., Bettoni, D., Ascaso, B., Tormen, G., Poggianti, B.M., Valentinuzzi, T., D’Onofrio, M., Fritz, J., Moretti, A., Omizzolo, A., Cava, A., Moles, M., Dressler, A., Couch, W.J., Kjærgaard, P., Varela, J. (2010). The shapes of BCGs and normal ellipticals in nearby clusters. *Mon. Not. R. Astron. Soc.*, 404 (3), 1490–1504. <http://dx.doi.org/10.1111/j.1365-2966.2010.16361.x>, arXiv:1001.2701.
- [66] Ferrarese, L., van den Bosch, F. C., Ford, H. C., Jaffe, W., O’Connell, R. W. (1994). Hubble Space Telescope Photometry of the Central Regions of Virgo Cluster Elliptical Galaxies. III. Brightness Profiles. *Astron. J.* 108, 1598. doi: 10.1086/117180.
- [67] Fu, L., Semboloni, E., Hoekstra, H., Kilbinger, M., van Waerbeke, L., Tereno, I., Mellier, Y., Heymans, C., Coupon, J., Benabed, K., Benjamin, J., Bertin, E., Doré, O., Hudson, M. J., Ilbert, O., Maoli, R., Marmo, C., McCracken, H. J., Ménard, B. (2008). Very weak lensing in the CFHTLS wide: cosmology from cosmic shear in the linear regime. *Astron. Astrophys.* 479(1), 9-25. doi: 10.1051/0004-6361:20078522
- [68] Furnell, K.E., Collins, C.A., Kelvin, L.S., Clerc, N., Baldry, I.K., Finoguenov, A., Erfanianfar, G., Comparat, J., Schneider, D. P. (2018). Exploring relations between BCG and cluster properties in the SPectroscopic IDentification of eROSITA Sources survey from $0.05 < z < 0.3$. *Mon. Not. R. Astron. Soc.*, 478, 4952- 4973. doi:10.1093/mnras/sty991
- [69] Furnell, K.E., Collins, C.A., Kelvin, L.S., Baldry, I.K., James, P.A., Manolopoulou, M., Mann, R.G., Giles, P.A., Bermeo, A., Hilton, M., Wilkinson, R., Romer, A.K., Vergara, C., Bhargava, S., Stott, J.P., Mayers, J., Viana, P., (2021). The growth of intracluster light in XCS-HSC galaxy clusters from $0.1 < z < 0.5$. *Mon. Not. R. Astron. Soc.*, 502 (2), 2419–2437. <http://dx.doi.org/10.1093/mnras/stab065>, arXiv:2101.01644.
- [70] Gallagher, J.S. and Ostriker, J.P. (1972). A Note on Mass Loss during Collisions between Galaxies and the Formation of Giant Systems. *Astron. J.*, 77, 288. doi:10.1086/111280
- [71] Garijo, A., Athanassoula, E., and Garcia-Gomez, C. (1997). The formation of cD galaxies. *Astron. Astrophys.*, 327, 930-946. doi:10.48550/arXiv.astro-ph/9705216

- [72] Graham, A., Lauer, T. R., Colless, M., and Postman, M. (1996). Brightest Cluster Galaxy Profile Shapes, *Astrophys.J.*, 465, 534. doi:10.1086/177440
- [73] Graham, A.W., Driver, S.P. (2005). A Concise Reference to (Projected) Sérsic $R_{1/n}$ Quantities, Including Concentration, Profile Slopes, Petrosian Indices, and Kron Magnitudes. *Publ. Astron. Soc. Aust.*, 22 (2), 118–127. <http://dx.doi.org/10.1071/AS05001>, arXiv:astro-ph/0503176.
- [74] Graham, M.L., Nugent, P.E., Sullivan, M., Filippenko, A.V., Cenko, S. B., Silverman, J.M., Clubb, K. I., and Zheng W. (2015). Constraining the progenitor companion of the nearby Type Ia SN 2011fe with a nebular spectrum at +981 d. *Mon. Not. R. Astron. Soc.*, 454, 1948–1957.
- [75] Grebel, E. K. (2004). The Evolutionary History of Local Group Irregular Galaxies. Carnegie Observatories Astrophysics Series, Cambridge Univ. Press. doi:10.48550/arXiv.astro-ph/0403222
- [76] Gunn, J.E., and Gott, J.R. (1972). On the Infall of Matter Into Clusters of Galaxies and Some Effects on Their Evolution. *Astrophys.J.* 176, 1. doi:10.1086/151605
- [77] Guo, Y., McIntosh, D. H., Mo, H. J., Katz N., van den Bosch F. C., Weinberg M., Weinmann S. M., Pasquali A., Yang X. (2009). Structural properties of central galaxies in groups and clusters, *Mon. Not. R. Astron. Soc.*, 398(3), 1129–1149. <https://doi.org/10.1111/j.1365-2966.2009.15223.x>
- [78] Gutiérrez, C.M., and Azzaro, M. (2004). The Properties of Satellite Galaxies in External Systems. II. Photometry and Colors. *Astrophys. J., Suppl. Ser.* 155, 395. doi:10.1086/422357.
- [79] Hansen, S.M., Sheldon, E.S., Wechsler, R.H., Koester, B.P., (2009). The Galaxy Content of SDSS Clusters and Groups. *Astrophys. J.*, 699 (2), 1333–1353. <http://dx.doi.org/10.1088/0004-637X/699/2/1333>, arXiv:0710.3780.
- [80] Hoessel, J.G., and Schneider, D.P. (1985). CCD observations of Abell clusters. IV - Surface photometry of 175 brightest cluster galaxies. *Astron. J.*, 90, 1684–1664. doi: 10.1086/113871.
- [81] Hoessel, J. G., Oegerle, W. R., and Schneider, D. P. (1987). The surface-brightness-effective-size relation for elliptical galaxies in the cores of clusters. *Astron. J.* 94, 1111-1115. doi:10.1086/114548
- [82] Hogan, C. J. (1998). *The Little Book of the Big Bang*, Springer-Verlag, Heidelberg.
- [83] Hogg, D. W., Blanton, M. R., Brinchmann, J., Eisenstein, D. J., Schlegel, D. J., Gunn, J. E., McKay, T. A., Rix, H.-W., Bahcall, N. A., Brinkmann, J., Meiksin, A. (2004). The Dependence on Environment of the Color-Magnitude Relation of Galaxies. *Astrophys. J.*, 601(1), L29-L32. doi :10.1086/381749
- [84] Hudelot, P., Cuillandre, J.C., Withington, K., Goranova, Y., McCracken, H., Magnard, F., Mellier, Y., Regnault, N., Betoule, M., Aussel, H., Kavelaars, J.J., Fernique, P., Bonnarel, F., Ochsenbein, F., Ilbert, O. (2012). VizieR Online Data Catalog: The CFHTLS Survey (T0007 release) (Hudelot+ 2012). p. II/317, VizieR Online Data Catalog.

- [85] Ilbert, O., Arnouts, S., McCracken, H.J., Bolzonella, M., Bertin, E., Le Fèvre, O., Mellier, Y., Zamorani, G., Pellò, R., Iovino, A., Tresse, L., Le Brun, V., Bottini, D., Garilli, B., Maccagni, D., Picat, J.P., Scaramella, R., Scodreggio, M., Vettolani, G., ..., Vergani, D. (2006). Accurate photometric redshifts for the CFHT legacy survey calibrated using the VIMOS VLT deep survey. *Astron. Astrophys.*, 457 (3), 841–856. <http://dx.doi.org/10.1051/0004-6361:20065138>, arXiv:astro-ph/0603217.
- [86] Jordan, A. Cote, P., West, M.J., Morzke, R.O., Minniti, D. and Rejkuba, M. (2004). Hubble space telescope observations of CD galaxies and their globular cluster systems, *Astron. J.*, 127, 24-47. arXiv:astro-ph/0309795.
- [87] Jorgensen, I., Franx, M., and Kjaergaard, P. (1995). Spectroscopy for E and S0 galaxies in nine clusters. *Mon. Not. R. Astron. Soc.*, 276, 1341–1364. doi:10.1093/mnras/276.4.1341
- [88] Jorgensen, I. (1999). E and S0 galaxies in the central part of the Coma cluster: ages, metal abundances and dark matter. *Mon. Not. R. Astron. Soc.*, 306 (3), 607–636.
- [89] Kauffmann, G., White, S. D. M., Heckman, T. M., Ménard, B., Brinchmann, J., Charlot S., Tremonti, C., Brinkmann, J. (2004). The environmental dependence of the relations between stellar mass, structure, star formation and nuclear activity in galaxies. *Mon. Not. R. Astron. Soc.*, 353, 713-731. doi: 10.1111/j.1365-2966.2004.08117.x
- [90] Keel, B. (2012). Galaxies and the Universe. <http://www.astr.ua.edu/keel/galaxies/index.html>
- [91] Khosroshahi, H. G., Wadadekar, Y., and Kembhavi, A. (2000). Correlations among Global Photometric Properties of Disk Galaxies. *Astrophys. J.*, 533:162–171. doi:10.1086/308654
- [92] King, I. (1962). The structure of star clusters. I. an empirical density law. *Astron. J.*, 67, 471. doi:10.1086/108756
- [93] Kluge, M., Neureiter, B., Riffeser, A., Bender, R., Goessl, C., Hopp, U., Schmidt, M., Ries, C., Brosch, N. (2020). Structure of Brightest Cluster Galaxies and Intracluster Light. *Astrophys. J. Suppl.*, 247 (2), 43. <http://dx.doi.org/10.3847/1538-4365/ab733b>, arXiv:1908.08544.
- [94] Kormendy, J. (1977). Brightness distributions in compact and normal galaxies. II. Structure parameters of the spheroidal component. *Astrophys. J.* 218, 333–346. <http://dx.doi.org/10.1086/155687>.
- [95] Kormendy, J., Fisher, D.B., Cornell, M.E., Bender, R. (2009). Structure and Formation of Elliptical and Spheroidal Galaxies. *Astrophys. J. Suppl.*, 182 (1), 216–309. <http://dx.doi.org/10.1088/0067-0049/182/1/216>, arXiv:0810.1681
- [96] Kormendy, J., and Kennicutt, R. C., Jr. (2004). Secular Evolution and the Formation of Pseudobulges in Disk Galaxies. *Annu. Rev. Astron. Astrophys.*, 42, 603-683. <https://doi.org/10.1146/annurev.astro.42.053102.134024>
- [97] Kravtsov, A. V., and Borgani, S. (2012). Formation of Galaxy Clusters. *Annu. Rev. Astron. Astrophys.*, 50, 353-409. doi:10.1146/annurev-astro-081811-125502

- [98] La Barbera, F., Merluzzi, P., Busarello, G., Massarotti, M., Mercurio, A. (2004). Probing galaxy evolution through the internal colour gradients, the Kormendy relations and the Photometric Plane of cluster galaxies at $z \approx 0.2$. *Astron. Astrophys.* 425, 797–812. <http://dx.doi.org/10.1051/0004-6361:20047157>, arXiv:astro-ph/0307482.
- [99] Lake, G. (1992). Understanding the Hubble Sequence, *Sci. Technol*, 5, 515.
- [100] Lambas, D. G., Groth, E. J., & Peebles, P. J. E. (1988). Alignments of Brightest Cluster Galaxies with Large-Scale Structures. *Astron. J.* 95, 996. doi:10.1086/114695
- [101] Larson R. B., Tinsley B. M., Caldwell C. N. (1980). The evolution of disk galaxies and the origin of S0 galaxies. *Astrophys. J.* 237, 692-707. doi:10.1086/157917
- [102] Lauer, T.R., and Postman, M. (1992). The Hubble Flow from Brightest Cluster Galaxies. *Astrophys. J. Lett.*, 400, L47. <http://dx.doi.org/10.1086/186646>.
- [103] Lauer, T. R., Ajhar, E. A., Byun, Y.-I., Dressler, A., Faber, S. M., Grillmair, C., Kormendy, J., Richstone, D., and Tremaine, S. (1995). The Centers of Early-Type Galaxies with HST.I. An Observational Survey. *Astron. J.*, 110, 2622.
- [104] Lavoie, S., Willis, J.P., Démoclès, J., Eckert, D., Gastaldello, F., Smith, G.P., Lidman, C., Adami, C., Pacaud, F., Pierre, M., Clerc, N., Giles, P., Lieu, M., Chiappetti, L., Altieri, B., Ardila, F., Baldry, I., Bongiorno, A., Desai, S.,...Tuffs, R.J. (2016). The XXL survey XV: evidence for dry merger driven BCG growth in XXL-100-GC X-ray clusters. *Mon. Not. R. Astron. Soc.*, 462 (4), 4141–4156. <http://dx.doi.org/10.1093/mnras/stw1906>, arXiv:1608.01223
- [105] Lea, S.M., Silk, J., Kellogg, E., and Murray, S. (1973). Thermal-Bremsstrahlung Interpretation of Cluster X-Ray Sources. *Astrophys. J.*, 184, L105. doi:10.1086/181300
- [106] Le Fèvre, O., Vettolani, G., Garilli, B., Tresse, L., Bottini, D., Le Brun, V., Maccagni, D., Picat, J.P., Scaramella, R., Scodreggio, M., Zanichelli, A., Adami, C., Arnaboldi, M., Arnouts, S., Bardelli, S., Bolzonella, M., Cappi, A., Charlot, S., Ciliegi, P.,...Rizzo, D. (2005). The VIMOS VLT deep survey. First epoch VVDS-deep survey: 11 564 spectra with $17.5 \leq IAB \leq 24$, and the redshift distribution over $0 \leq z \leq 5$. *Astron. Astrophys.*, 439 (3), 845–862. <http://dx.doi.org/10.1051/0004-6361:20041960>, arXiv:astro-ph/0409133.
- [107] Lidman, C., Suherli, J., Muzzin, A., Wilson, G., Demarco, R., Brough, S., Rettura, A., Cox, J., DeGroot, A., Yee, H.K.C., Gilbank, D., Hoekstra, H., Balogh, M., Ellingson, E., Hicks, A., Nantais, J., Noble, A., Lacy, M., Surace, J., Webb, T. (2012). Evidence for significant growth in the stellar mass of brightest cluster galaxies over the past 10 billion years. *Mon. Not. R. Astron. Soc.*, 427 (1), 550–568. <http://dx.doi.org/10.1111/j.1365-2966.2012.21984.x>, arXiv:1208.5143.

- [108] Lidman, C., Iacobuta, G., Bauer, A.E., Barrientos, L.F., Cerulo, P., Couch, W.J., Delaye, L., Demarco, R., Ellingson, E., Faloon, A.J., Gilbank, D., Huertas-Company, M., Mei, S., Meyers, J., Muzzin, A., Noble, A., Nantais, J., Rettura, A., Rosati, P., Sánchez-Janssen, R., Strazzullo, V., Webb, T.M.A., Wilson, G., Yan, R., Yee, H.K.C. (2013). The importance of major mergers in the build up of stellar mass in brightest cluster galaxies at $z=1$. *Mon. Not. R. Astron. Soc.*, 433 (1), 825–837. <http://dx.doi.org/10.1093/mnras/stt777>, arXiv:1305.0882.
- [109] Lin, Y.-T., and Mohr, J. J. (2004). K-band Properties of Galaxy Clusters and Groups: Brightest Cluster Galaxies and Intracluster Light. *Astrophys. J.*, 617, 879.
- [110] Liu F. S., Xia X. Y., Mao S., Wu H., Deng Z. G. (2008). Photometric properties and scaling relations of early-type Brightest Cluster Galaxies. *Mon. Not. R. Astron. Soc.*, 385, 23. <https://doi.org/10.1111/j.1365-2966.2007.12818.x>
- [111] Lin, Y.-T., Ostriker, J. P., and Miller, C. J. (2010). A New Test of the Statistical Nature of the Brightest Cluster Galaxies. *Astrophys. J.*, 715, 1486–1496. doi:10.1088/0004-637X/715/2/1486
- [112] Liu, F.S., Mao, S., Deng, Z.G., Xia, X.Y., Wen, Z.L. (2009). Major dry mergers in early-type brightest cluster galaxies. *Mon. Not. R. Astron. Soc.*, 396 (4), 2003–2010. <http://dx.doi.org/10.1111/j.1365-2966.2009.14907.x>, arXiv:0904.2379.
- [113] Livio, M., 2000, *The Accelerating Universe*, John Wiley & Sons, New York.
- [114] Loh, Y.-S., and Strauss, M. A. (2006). The bright end of the luminosity function of red sequence galaxies, *Mon. Not. R. Astron. Soc.*, 366, 373. doi:10.1111/j.1365-2966.2005.09714.x
- [115] Longhetti, M., Saracco, P., Severgnini, P., Della Ceca, R., Mannucci, F., Bender, R., Drory, N., Feulner, G., Hopp, U., (2007). The Kormendy relation of massive elliptical galaxies at $z \sim 1.5$: evidence for size evolution. *Mon. Not. R. Astron. Soc.* 374 (2), 614–626. <http://dx.doi.org/10.1111/j.1365-2966.2006.11171.x>, arXiv:astro-ph/0610241
- [116] Longo, G., Capaccioli, M., Busarello, G. (eds). (1992). *Morphological and Physical Classification of Galaxies*, Kluwer Academic Publishers, Dordrecht.
- [117] Lopes de Oliveira, Lima Neto, G. B., Mendes de Oliveira, C., Janot-Pacheco, E., and Motch, C. (2006). Discovery of a cluster of galaxies behind the Milky Way: X-ray and optical observations. *Astron. Astrophys.*, 459:415–422. doi: 10.1051/0004-6361:20065681
- [118] Lotz, J. M., Primack, J. and Madau, P. (2004). A New Nonparametric Approach to Galaxy Morphological Classification. *Astron. J.*, 128:163–182. doi: 10.1086/421849
- [119] Loubser, S. I., Sánchez-Blázquez, P., Sansom, A. E., and Soechting, I. K. (2009). Stellar populations in the centres of brightest cluster galaxies. *Mon. Not. R. Astron. Soc.*, 398, 133–156. doi:10.1111/j.1365-2966.2009.15171.x
- [120] Lucentini, J., 2002, *The Mysteries of Galaxy Spirals*, *Sci. Technol.*, 9, 29.
- [121] Luoma, A., J., I. (2018). Parametric studies of galaxy structure and morphology using GALFIT. [Master's thesis]. University of Helsinki.

- [122] Mackie, G. (2011). *The Multiwavelength Atlas of Galaxies*, Cambridge University Press. <https://ui.adsabs.harvard.edu/abs/2011mag..book.....M>
- [123] McCracken, H. J., Ilbert, O., Mellier, Y., Bertin, E., Guzzo, L., Arnouts, S., Le Fèvre, O., and Zamorani, G. (2008). Clustering properties of a type-selected volume-limited sample of galaxies in the CFHTLS. *Astron. Astrophys.*, 479, 321. doi: 10.1051/0004-6361:20078636
- [124] McIntosh D. H., Guo Y., Hertzberg J., Katz N., Mo H. J., van den Bosch F. C., Yang X. (2008). Ongoing assembly of massive galaxies by major merging in large groups and clusters from the SDSS. *Mon. Not. R. Astron. Soc.*, 388, 1537. doi:10.1111/j.1365-2966.2008.13531.x
- [125] Moffat, A. F. J. (1969). A Theoretical Investigation of Focal Stellar Images in the Photographic Emulsion and Application to Photographic Photometry. *Astron. Astrophys.*, 3, 455.
- [126] Moore B., Katz N., Lake G., Dressler A., Oemler A. (1996). Galaxy harassment and the evolution of clusters of galaxies, *Nat*, 379, 613. doi:10.1038/379613a0
- [127] Mundy, C. J., Conselice, C. J., and Ownsworth, J. R. (2015). Tracing galaxy populations through cosmic time: a critical test of methods for connecting the same galaxies between different redshifts at $z < 3$. *Mon. Not. R. Astron. Soc.*, 450, 3696
- [128] Murante, G., Giovalli, M., Gerhard, O., Arnaboldi, M., Borgani, S., and Dolag, K. (2007). The importance of mergers for the origin of intracluster stars in cosmological simulations of galaxy clusters. *Mon. Not. R. Astron. Soc.*, 377, 2. <https://doi.org/10.1111/j.1365-2966.2007.11568.x>
- [129] Mushotzky, R.F., and Smith, B.W. (1979). X-ray spectra of clusters of galaxies. *Highl. Astr., IAU*, 5, 735. <https://ui.adsabs.harvard.edu/abs/1980HiA.....5..735M>
- [130] Naab, T., Johansson, P.H., Ostriker, J.P. (2009). Minor Mergers and the Size Evolution of Elliptical Galaxies. *Astrophys. J. Lett.*, 699 (2), L178–L182. <http://dx.doi.org/10.1088/0004-637X/699/2/L178>, arXiv:0903.1636.
- [131] Nelson, A.E., Gonzalez, A.H., Zaritsky, D., Dalcanton, J.J. (2002). Revisiting Brightest Cluster Galaxy Evolution with the Las Campanas Distant Cluster Survey. *Astrophys. J.*, 566 (1), 103–122. <http://dx.doi.org/10.1086/338054>, arXiv:astro-ph/0110310.
- [132] Niederste-Ostholt, M., Strauss, M.A., Dong, F., Koester, B.P., McKay, T.A. (2010). Alignment of brightest cluster galaxies with their host clusters. *Mon. Not. R. Astron. Soc.*, 405 (3), 2023–2036. <http://dx.doi.org/10.1111/j.1365-2966.2010.16597.x>, arXiv:1003.0322.
- [133] Oegerle, W.R., and Hoessel, J.G. (1991). Fundamental Parameters of Brightest Cluster Galaxies. *Astrophys. J.*, 375, 15. doi:10.1086/170165
- [134] Oegerle, W.R., Hill, J.M. (2001). Dynamics of cD Clusters of Galaxies. IV. Conclusion of a Survey of 25 Abell Clusters. *Astron. J.*, 122 (6), 2858–2873. <http://dx.doi.org/10.1086/323536>.
- [135] Oemler, A. (1976). The structure of elliptical and cD galaxies. *Astrophys. J.*, 209, 693. doi:10.1086/154769

- [136] Ostriker, J.P., and Hausman, M.A. (1977). Cannibalism among the galaxies: dynamically produced evolution of cluster luminosity functions. *Astrophys. J.*, 217, L125. doi:10.1086/182554
- [137] Ownsworth, J. R., Conselice, C. J., Mortlock, A., Hartley, W.G., Almaini, O., Duncan, K., Mundy, C.J. (2014). Minor versus major mergers: the stellar mass growth of massive galaxies from $z = 3$ using number density selection techniques. *Mon. Not. R. Astron. Soc.*, 445, 2198–2213 <https://doi.org/10.1093/mnras/stu1802>
- [138] Parker, L.C., Hoekstra, H., Hudson, M.J., Waerbeke, L.V., Mellier, Y. (2007). The Masses and Shapes of Dark Matter Halos from Galaxy-Galaxy Lensing in the CFHT Legacy Survey. *Astrophys. J.*, 669, 21. doi:10.1086/521541
- [139] Patel, P., Maddox, S., Pearce, F. R., Aragón-Salamanca, A., and Conway, E. (2006). An imaging survey of a uniform sample of brightest cluster galaxies and intracluster light, *Mon. Not. R. Astron. Soc.*, 370, 851. <https://doi.org/10.1111/j.1365-2966.2006.10510.x>
- [140] Peng, C.Y. (2002). GALFIT user's manual. <https://users.obs.carnegiescience.edu/peng/work/galfit/README.pdf>
- [141] Peng, C.Y., Ho, L.C., Impey, C.D., Rix, H.-W. (2002). Detailed Structural Decomposition of Galaxy Images. *Astron. J.*, 124 (1), 266–293. <http://dx.doi.org/10.1086/340952>, arXiv:astro-ph/0204182.
- [142] Peng, C.Y., Ho, L.C., Impey, C.D., Rix, H.-W. (2010). Detailed Decomposition of Galaxy Images. II. Beyond Axisymmetric Models. *Astron. J.*, 139 (6), 2097–2129. <http://dx.doi.org/10.1088/0004-6256/139/6/2097>, arXiv:0912.0731.
- [143] Pignatelli, E., Fasano, G., P. Cassata, P. (2006). GASPHOT: a tool for Galaxy Automatic Surface PHOTometry. *Astron. Astrophys.*, 446, 373–388. doi:10.1051/0004-6361:20041704
- [144] Postman, M., Lauer, T.R. (1995). Brightest Cluster Galaxies as Standard Candles. *Astrophys. J.*, 440, 28. <http://dx.doi.org/10.1086/175245>.
- [145] Quintana, H., and Lawrie, D.G. (1982). On the Determination of Velocity Dispersions for CD Clusters of Galaxies. *Astron. J.* 87, 1. doi:10.1086/113080
- [146] Rasmussen, J., Mulchaey, J. S., Bai, L., Ponman, T. J., Raychaudhury, S., Dariush, A., (2010). *Astrophys. J.* 717, 958. doi:10.1088/0004-637X/717/2/958
- [147] Rix, H-W, Zaritsky, D. (1995). Nonaxisymmetric Structures in the Stellar Disks of Galaxies. *Astrophys. J.* 447, 82. doi: arXiv:astro-ph/9505111.
- [148] Rubin, V. C., Whitmore, B. C., and Ford, Jr. W. K. (1988). Rotation curves for spiral galaxies in clusters. I-Data, global properties, and a comparison with field galaxies. *Astrophys J.*, 333, 522–541

- [149] Ruszkowski, M., Springel, V. (2009). The Role of Dry Mergers for the Formation and Evolution of Brightest Cluster Galaxies. *Astrophys. J.*, 696 (2), 1094–1102. <http://dx.doi.org/10.1088/0004-637X/696/2/1094>, arXiv:0902.0373.
- [150] Samir, R.M., Takey, A., Shaker, A.A. (2020). The fundamental plane of brightest cluster galaxies and isolated elliptical galaxies. *Astrophys. Space Sci.*, 365 (8), 142. <http://dx.doi.org/10.1007/s10509-020-03857-8>.
- [151] Sandage A. (1972). The Redshift-Distance Relation. I. Angular Diameter of First Ranked Cluster Galaxies as a Function of Redshift: the Aperture Correction to Magnitudes. *Astrophys. J.*, 173, 485. doi:10.1086/151440
- [152] Scarlata, C., Carollo, C.M., Lilly, S.J., Feldmann, R., Kampczyk, P., Renzini, A., Cimatti, A., Halliday, C., Daddi, E., Sargent, M.T., Koekemoer, A., Scoville, N., Kneib, J.P., Leauthaud, A., Massey, R., Rhodes, J., Tasca, L., Capak, P., McCracken, H.J.,...Takahashi, M. (2007). The Redshift Evolution of Early-Type Galaxies in COSMOS: Do Massive Early-Type Galaxies Form by Dry Mergers? *Astrophys. J. Suppl.*, 172 (1), 494–510. <http://dx.doi.org/10.1086/517972>, arXiv:astro-ph/0701746.
- [153] Schombert, J.M. (1987). The Structure of Brightest Cluster Members. II. Mergers. *Astrophys. J., Suppl.*, 64, 643. doi:10.1086/191212
- [154] Sérsic, J.L. (1963). Influence of the atmospheric and instrumental dispersion on the brightness distribution in a galaxy. *Bol. Asoc. Argent. Astron. Plata Argent.*, 6, 41–43.
- [155] Sérsic, J.L. (1968). *Atlas De Galaxias Australes*.
- [156] Shaaban, E., Alis, S., Bektasoglu, M., Yelkenci, F.K. Ulgen, E.K., Cakir, O., Fisek, S. (2022). Structural analysis of brightest cluster galaxies in poor and rich clusters. *New Ast.*, doi: <https://doi.org/10.1016/j.newast.2022.101998>
- [157] Shankar, F., Buchan, S., Rettura, A. Bouillot, V.C., Moreno, J., Licitra, R., Bernardi, M., Huertas-Company, M., Mei, S., Ascaso, B., Sheth, R., Delaye, L., Raichoor, A. (2015). Avoiding progenitor bias: the structural and mass evolution of brightest group and cluster galaxies in hierarchical models since $z \lesssim 1$. *Astrophys. J.*, 802, 73. doi:10.1088/0004-637X/802/2/73
- [158] Silk, J. (1976). Accretion by galaxy clusters and the relationship between X-ray luminosity and velocity dispersion. *Astrophys. J.*, 208, 646. doi:10.1086/154645
- [159] Simard, L., Mendel, J.T., Patton, D.R., Ellison, S.L., and McConnachie, A.W. A catalog of bulge+disk decompositions and updated photometry for 1.12 million galaxies in the sloan digital sky survey. *Astrophys. J., Suppl. Ser.*, 196, 11. doi:10.1088/0067-0049/196/1/11
- [160] Sparke, L., and Gallagher, J. (2007). *Galaxies in the Universe*, Cambridge University Press, Cambridge.
- [161] Steinicke, W., Jakiel, R. (2007). *Galaxies and How to Observe Them*, Berlin: Springer <https://ui.adsabs.harvard.edu/abs/2007ghot.book.....S>

- [162] Stott, J.P., Edge, A.C., Smith, G.P., Swinbank, A.M., Ebeling, H. (2008). Near-infrared evolution of brightest cluster galaxies in the most X-ray luminous clusters since $z=1$. *Mon. Not. R. Astron. Soc.*, 384 (4), 1502–1510. <http://dx.doi.org/10.1111/j.1365-2966.2007.12807.x>, arXiv:0712.0496.
- [163] Stott, J. P., Collins, C. A., Sahlén, M., Hilton, M., Lloyd-Davies, E., Capozzi, D., Hosmer, M., Liddle, A.R., N. Mehrtens, N., Miller, C.J., Romer, A.K., Stanford, S.A., Viana, P. T. P., Davidson, M., Hoyle, B., Kay, S.T., and R. C. Nichol. (2010). The XMMcluster survey: the build-up of stellar mass in brightest cluster galaxies at high redshift. *Astrophys. J.*, 718, 23. doi:10.1088/0004-637X/718/1/23
- [164] Stott, J.P., Collins, C.A., Burke, C., Hamilton-Morris, V., Smith, G.P. (2011). Little change in the sizes of the most massive galaxies since $z=1$. *Mon. Not. R. Astron. Soc.*, 414 (1), 445–457. <http://dx.doi.org/10.1111/j.1365-2966.2011.18404.x>, arXiv:1101.4652.
- [165] Stoughton, C., Lupton, R. H., Bernardi, M., Blanton, M. R., Burles, S., Castander, F. J., Connolly, A. J., Eisenstein, D. J., Frieman, J. A., Hennessy, G. S., Hindsley, Robert B., Ivezić, Ž., Stephen. k., Kunszt, P. Z., Lee, B. C., Meiksin, A., Munn, J. A., Newberg, H. J., Nichol, R. C., Zheng, W. (2002). Sloan Digital Sky Survey: Early Data Release. *Astrophys. J.*, 123, 485.
- [166] Tawfeek A.A. (2019). Morphological and Photometric Investigation of Some Galaxy Triplet Systems. [Ph. D. thesis]. Cairo University. Egypt.
- [167] Tereno, I., Schimd. C, Uzan, J.-P., Kilbinger, M., F. H. Vincent, F.H., and Fu, L. (2009). CFHTLS weak-lensing constraints on the neutrino masses. *Astron. Astrophys.*, 500, 657-665. <https://doi.org/10.1051/0004-6361/200811077>
- [168] Tonry, J.L. (1985). Observations of a complete sample of brightest cluster galaxies with multiple nuclei. *Astron. J.*, 90, 2431. doi:10.1086/113948
- [169] Tortorelli, L., Mercurio, A., Paolillo, M., Rosati, P., Gargiulo, A., Gobat, R., Balestra, I., Caminha, G.B., Annunziatella, M., Grillo, C., Lombardi, M., Nonino, M., Rettura, A., Sartoris, B., Strazzullo, V. (2018). The Kormendy relation of galaxies in the Frontier Fields clusters: Abell S1063 and MACS J1149.5+2223. *Mon. Not. R. Astron. Soc.*, 477 (1), 648–668. <http://dx.doi.org/10.1093/mnras/sty617>, arXiv:1803.02375.
- [170] Tovmassian, H.M, and Andernach, H. (2012). On the formation of cD galaxies and their parent clusters. *Mon. Not. R. Astron. Soc.*, 427, 2047. <https://doi.org/10.1111/j.1365-2966.2012.22044.x>
- [171] Ulgen, E.K., Alis, S., Benoist, C., Yelkenci, F.K., Cakir, O., Fisek, S., Karatas, Y., (2022). Identification and properties of isolated field elliptical galaxies from CFHTLS-W1. *Publ. Astron. Soc. Aust.*, 39, e031. <http://dx.doi.org/10.1017/pasa.2022.28>, arXiv:2205.10669.
- [172] Vaghmare, K. (2015). Structure, Properties and Formation Histories of S0 Galaxies [PhD thesis]. IUCAA and Jawaharlal Nehru University. India.
- [173] Van den Bergh, S. (1998). *Galaxy Morphology and Classification*. Cambridge University Press, Cambridge.

- [174] Van der Wel A., Holden B. P., Zirm A. W., Franx M., Rettura A., Illingworth G. D., Ford H. C. (2008). Recent Structural Evolution of Early-Type Galaxies: Size Growth from $z=1$ to $z=0$. *Astrophys. J.*, 688, 48.
- [175] Van Dokkum, P. G., Franx, M., Fabricant, D., Illingworth, G. D., and Kelson, D. D. (2000). Hubble Space Telescope Photometry and Keck Spectroscopy of the Rich Cluster MS 1054–03: Morphologies, Butcher-Oemler Effect, and the Color-Magnitude Relation at $z=0.83$. *Astrophys. J.*, 541(1), 95.
- [176] Vikhlinin, A., Kravtsov, A., Forman, W., Jones, C., Markevitch, M., Murray, S.S., Van Speybroeck, L. (2006). Chandra Sample of Nearby Relaxed Galaxy Clusters: Mass, Gas Fraction, and Mass-Temperature Relation. *Astrophys. J.* 640 (2), 691–709. <http://dx.doi.org/10.1086/500288>, arXiv:astro-ph/0507092.
- [177] Vikram, V., Wadadekar, Y., Kembhavi, A.K., and Vijayagovindan., G.V. (2010). PYMORPH: automated galaxy structural parameter estimation using PYTHON. *Mon. Not. R. Astron. Soc.*, 409, 1379–1392. doi: 10.1111/j.1365-2966.2010.17426.x
- [178] Voit, G. M. (1999). The Rise and Fall of Quasars. *Sci. Technol.*, 5, 40.
- [179] Von Der Linden, A., Best, P.N., Kauffmann, G., White, S.D.M. (2007). How special are brightest group and cluster galaxies? *Mon. Not. R. Astron. Soc.* 379 (3), 867–893. <http://dx.doi.org/10.1111/j.1365-2966.2007.11940.x>, arXiv:astro-ph/0611196.
- [180] Vulcani, B., Marchesini, D., De Lucia, G., Muzzin, A., Stefanon, M., Brammer, G.B. Labbé, I., Le Fèvre, O., and Milvang-Jensen, B. (2016). Mergers and star formation: the environment and stellar mass growth of the progenitors of ultra-massive galaxies since $z=2$. *Astrophys. J.*, 816, 86. doi:10.3847/0004-637X/816/2/86
- [181] Wadadekar, Y. (2012). The 11th Asian-Pacific Regional IAU Meeting 2011, NARIT Conference Series, Vol. 1, ed: S. Komonjinda, Y. Kovalev, D. Rufolo. <http://arxiv.org/abs/1201.2252v1>
- [182] Weinmann S. M., Kauffmann G., van den Bosch F. C., Pasquali A., McIntosh D. H., Mo H., Yang X., Guo Y. (2009). Environmental effects on satellite galaxies: the link between concentration, size and colour profile. *Mon. Not. R. Astron. Soc.*, 394, 1213 <https://doi.org/10.1111/j.1365-2966.2009.14412.x>
- [183] West, M.J., de Propris, R., Bremer, M.N., Phillipps, S. (2017). Ten billion years of brightest cluster galaxy alignments. *Nat. Astron.*, 1, 0157. <http://dx.doi.org/10.1038/s41550-017-0157>, arXiv:1706.03798.
- [184] Whiley, I. M., Aragón-Salamanca, A., De Lucia, G., Von Der Linden, A., S. P. Bamford, S.P., Best, P., Bremer, M.N., Jablonka, P., Johnson, O., Milvang-Jensen, B., Noll, S., Poggianti, B.M., Rudnick, G., Saglia, R., White, S., Zaritsky, D. (2008). The evolution of the brightest cluster galaxies since $z\sim 1$ from the ESO Distant Cluster Survey (EdisCS). *Mon. Not. R. Astron. Soc.*, 387, 1253. <https://doi.org/10.1111/j.1365-2966.2008.13324.x>
- [185] White, S.D.M. (1976). The dynamics of rich clusters of galaxies, *Mon. Not. R. Astron. Soc.*, 177, 717. <https://doi.org/10.1093/mnras/177.3.717>

- [186] White, R.A. (1978). Some morphological characteristics of clusters of galaxies. *Astrophys. J.*, 226, 591. doi:10.1086/156643
- [187] Yelkenci, F.K. (2015). Evolution of the Galaxy Morphology - Density Relation [Ph.D. thesis]. Istanbul University, Turkey.
- [188] Zeilik, M. (2002). *Astronomy: The Evolving Universe*. Ninth Edition, Cambridge University Press, Cambridge.
- [189] Zhao, D., Aragón-Salamanca, A., Conselice, C.J. (2015). Evolution of the brightest cluster galaxies: the influence of morphology, stellar mass and environment. *Mon. Not. R. Astron. Soc.*, 453 (4), 4444–4455. <http://dx.doi.org/10.1093/mnras/stv1940>, arXiv:1508.04845.

CURRICULUM VITAE

Name Surname : Eman Aly Shaaban ABDELMOTALEB

EDUCATION:

- **Undergraduate** : 2006, Cairo University, Faculty of science, Department of Physics and Astronomy
- **Graduate** : 2014, Cairo University, Faculty of science, Department of Physics and Astronomy

PROFESSIONAL EXPERIENCE AND AWARDS:

- She worked as an assistant researcher in National Research Center, Egypt between 2008- 2016.

PUBLICATIONS, PRESENTATIONS AND PATENTS ON THE THESIS:

- Shaaban, E., Alis, S., Bektasoglu, M., Yelkenci, F.K. Ulgen, E.K., Cakir, O., Fisek, S. (2022). Structural analysis of brightest cluster galaxies in poor and rich clusters. *New Ast.*, doi: <https://doi.org/10.1016/j.newast.2022.101998> (Article)
- Gamal B. A., Shaban, E. A., Amin, M. Y., R., M. A. (2014). Detailed surface photometry of the cD galaxies NGC 4839 and NGC 4874. *Astrophys. Space Sci.*, 352, 789. <https://doi.org/10.1007/s10509-014-1991-y> (Article)
- Shaaban, E., Gamal B. A. (2014, Aug). The Third Middle-East and Africa IAU Regional Meeting “MEARIM”. Lebanon. (Presentation)
- Shaaban, E. (2012, Oct). The Third Arab Conference of Astronomy and Geophysics at National Research Institute of Astronomy and Geophysics (NRIAG). Cairo, Egypt. (Presentation)
- Shaaban, E. (2012, July). The 3rd Azarquiel School of Astronomy. Istanbul, Turkey. (Presentation)

OTHER PUBLICATIONS, PRESENTATIONS AND PATENTS::